MODELING AND IDENTIFICATION OF CONTACT DYNAMICS AT SHRINK-FIT HOLDER-EXTENSION AND EXTENSION-TOOL INTERFACES

A THESIS SUBMITTED TO
THE GRADUATE SCHOOL OF NATURAL AND APPLIED SCIENCES
OF
MIDDLE EAST TECHNICAL UNIVERSITY

BY

MUSTAFA ÜNAL ALTIN

IN PARTIAL FULFILLMENT OF THE REQUIREMENTS
FOR
THE DEGREE OF MASTER OF SCIENCE
IN
MECHANICAL ENGINEERING

APRIL 2023

Approval of the thesis:

MODELING AND IDENTIFICATION OF CONTACT DYNAMICS AT SHRINK-FIT HOLDER-EXTENSION AND EXTENSION-TOOL INTERFACES

submitted by **MUSTAFA ÜNAL ALTIN** in partial fulfillment of the requirements for the degree of **Master of Science** i**n Mechanical Engineering, Middle East Technical University** by,

Prof. Dr. Halil KALIPÇILAR
Director, Graduate School of **Natural and Applied Sciences** _____

Prof. Dr. M.A. Sahir Arıkan
Head of the Department, **Mechanical Engineering** _____

Assist. Prof. Dr. Orkun Özşahin
Supervisor, **Mechanical Engineering, METU** _____

Examining Committee Members:

Assoc. Prof. Dr. Mehmet Bülent ÖZER
Mechanical Engineering, METU _____

Assist. Prof. Dr. Orkun ÖZŞAHİN
Mechanical Engineering, METU _____

Assoc. Prof. Dr. Ulaş YAMAN
Mechanical Engineering, METU _____

Assist. Prof. Dr. Gökhan ÖZGEN
Mechanical Engineering, METU _____

Assoc. Prof. Dr. Can Ulaş DOĞRUER
Mechanical Engineering, Hacettepe University _____

Date: 25.04.2023

I hereby declare that all information in this document has been obtained and presented in accordance with academic rules and ethical conduct. I also declare that, as required by these rules and conduct, I have fully cited and referenced all material and results that are not original to this work.

Name Last name: MUSTAFA ÜNAL ALTIN

Signature:

ABSTRACT

MODELING AND IDENTIFICATION OF CONTACT DYNAMICS AT SHRINK-FIT HOLDER-EXTENSION AND EXTENSION-TOOL INTERFACES

Altın, Mustafa Ünal
Master of Science, Mechanical Engineering
Supervisor: Asst. Prof. Dr. Orkun Özşahin

April 2023, 107 pages

Frequency response functions at the extension and tool tip for different holders, extension, and tool assembly can be obtained using experiments. But performing experiments for every combination requires so much effort and time. Using Finite Element Modelling programs, the dynamic properties of these contact regions can be found. Then using the dynamic properties found, the RCSA method can be performed and Frequency response functions for the desired combination can be calculated efficiently. After proving the method is suitable for real-life applications, it can be applied to the other connection types.

Keywords: Shrink Fit, Contact Dynamics, High Speed Machining, Receptance Coupling

ÖZ

SIKI GEÇME İLE BİRLEŞEN TAKIM TUTUCU-UZATICI VE UZATICI-TAKIM ARAYÜZÜNÜN TEMAS DİNAMİKLERİNİN MODELLENMESİ VE BELİRLENMESİ

Altın, Mustafa Ünal
Yüksek Lisans, Makina Mühendisliği
Tez Yöneticisi: Asist. Prof. Dr. Orkun Özşahin

Nisan 2023, 107 sayfa

Farklı takım tutucu, uzatıcı ve takım kombinasyonları için uzatıcı ve takım ucundaki frekans tepki fonkiyonları deneyler ile bulunabilir. Fakat her farklı kombinasyon için deneyleri icra etmek çok fazla efor ve zaman harcamayı gerektirir. Sonlu elemanlar modeli kullanarak temas yüzeylerinin dinamik özellikleri hesaplanabilir. Elde edilen dimanik özellikler kullanılarak, RCSA metodu kullanılabilir ve istenilen kombinasyon için frekans tepki fonksiyonu efektif bir şekilde hesaplanabilir. Bu metodun gerçek hayata uygunluğu kanıtlandıktan sonra diğer bağlantı tiplerine de uygulanabilir.

Anahtar Kelimeler: Sıkı geçme, Temas Dinamikleri, Yüksek Hızlı İşleme, Dinamik Esneklik Birleştirme

To my family

ACKNOWLEDGMENTS

I wish to express my genuine gratitude to my supervisor Asst. Prof. Dr. Orkun Özşahin for his guidance, valuable advice, and encouragement throughout all the stages of this research.

I would like to thank my parents and my siblings for their support and encouragement in my academic life.

And I would also like to thank my wife, Büşra. Without her support, I could not finish this work. She always believes in me and is by my side.

TABLE OF CONTENTS

LIST OF TABLES

TABLES

LIST OF FIGURES

FIGURES

LIST OF ABBREVIATIONS

FEM	: Finite Element Model
FRF	: Frequency Response Function
RCSA	: Receptance Coupling Substructure Analysis
IRCSA	: Inverse Receptance Coupling Substructure Analysis
STL	: Stereolithographic
SVD	: Singular Value Decomposition

LIST OF SYMBOLS

E	: Elastic modulus
ρ	: Density
ν	: Poisson's ratio
μ	: Friction coefficient
ω	: Excitation frequency
k_{yf}	: Displacement to force stiffness
$k_{\theta f}$	: Rotation to force stiffness
k_{yM}	: Displacement to moment stiffness
$k_{\theta M}$	: Rotation to moment stiffness
c_{yf}	: Displacement to force damping
$c_{\theta f}$	: Rotation to force damping
k_{yM}	: Displacement to moment damping
$c_{\theta M}$	: Rotation to moment damping
H_{ij}	: Receptance function (Displacement of point i due to the unit force at point j)
L_{ij}	: Receptance function (Displacement of point i due to the unit moment at point j)
N_{ij}	: Receptance function (Rotation of point i due to the unit force at point j)

P_{ij} : Receptance function (Rotation of point i due to the unit moment at point j)

A : Cross sectional area

γ : Loss factor

ω_r : r-th natural frequency

ϕ_r : r-th mode shape

F_d : Frictional force

CHAPTER 1

INTRODUCTION

1.1 General Overview

Machining is frequently used in manufacturing processes in industry because of its capability to produce a wide variety of components. However, chatter is one of the main problems in machining. It is caused by dynamic interaction between the cutting tool and the work piece. It results in instability and poor surface finish. Much research has been done to eliminate this problem. Using stability lobe diagram, optimum depth of cut and spindle speed combination can be found. However, to obtain this stability lobe diagram FRF of the assembly at the tool tip must be obtained. For every tool-spindle combination an experiment can be performed but it is not practical. To minimize the effort and save time and money, the receptance coupling method can be used to find the tool point FRF of each tool-holder combination. By doing a small number of experiments the contact dynamics properties between the tool and holder can be obtained, and the result can be applied to different configurations such as different tool overhang and different interference amounts.

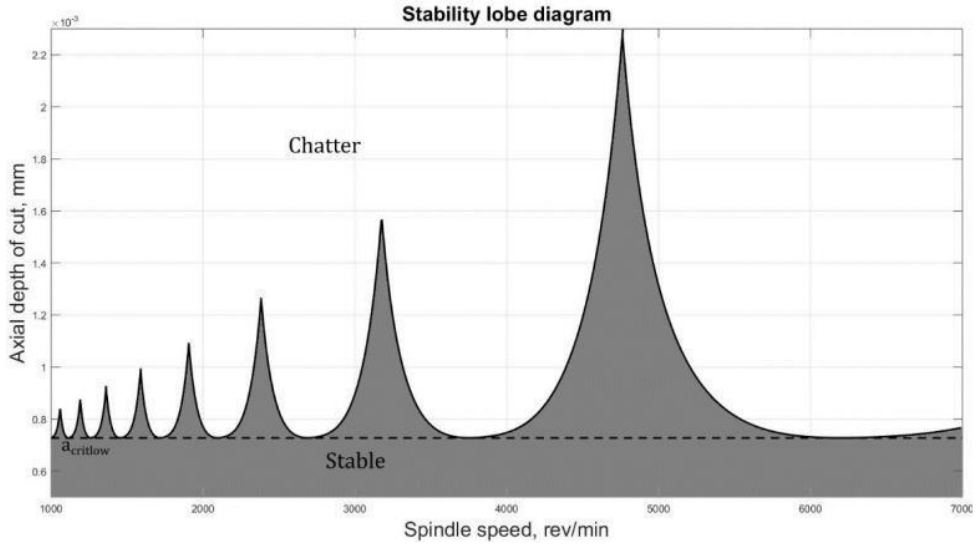

Figure 1-1 Stability lobe diagram [44]

The other method to identify these properties is using finite element methods. Because of the ease to access finite element software and recent developments in finite element methods, many finite element software are now frequently used in structural dynamics problems. Their ability to accurately model a single part is typically acceptable. Nevertheless, engineering structures are usually made up of combinations of various parts or substructures. The accuracy and dependability needed for finite element modeling and calculating the dynamic results of the combined structures are sadly lacking. The results of the real-life tests frequently differ from those of the finite element analysis, and this incompatibility is thought to be caused by the impurity of the material's properties, the nature of the joints, etc., as well as any potential non-linearities. Mechanical joint characteristics have a significant impact on system responses. The calculation of the dynamic properties of the entire assembly may become inaccurate or even inconsequential if these effects are ignored. Numerous mechanical joints, such as rivets, bolts, etc., connect the various substructure assemblies that make up complex systems. Representative models of joints made up of masses, springs, and dampers must be created for these systems. To accurately predict the dynamic properties of mechanical systems connection elements, such as stiffnesses and damping coefficients, must be identified.

1.2 Literature Review

Schimtz et al.[1] used a finite element modeling approach to identify the dynamic properties at the holder and tool with shrink fit connection. All across the contact region, continuous stiffness and damping profiles are determined. After obtaining the dynamic properties they used them to estimate the real values obtained by experiments. To model the holder and the tool, they used Euler-Bernoulli beam theory. Then, they seperated the tool inside the holder and using two spring damper couple at two end of the contact region. They succesfully simulate the shrink fit contact properties. Model of the assembly with distributed stiffness is given in Figure 1-2 and the complex stiffness matrix used to couple the substructures is given Equation 1.1.

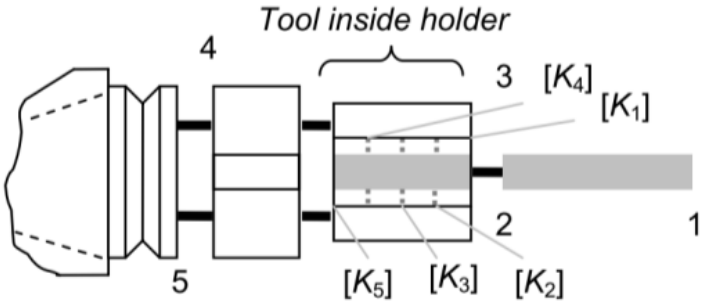

Figure 1-2 Shrink fit tool holder connection modeling [1]

$$[K^*] = \begin{bmatrix} k_{yf} + i\omega c_{yf} & k_{yM} + i\omega c_{yM} \\ k_{\theta f} + i\omega c_{yf} & k_{\theta M} + i\omega c_{yM} \end{bmatrix} \tag{1.1}$$

Xiao et al. [2] used tapered zero-thickness elements to identify the contact properties between spindle and holder. They modeled the spindle and the holder as 3D solid elements and modeled the contact with zero-thickness elements with stiffness and damping as seen in Figure 1-3. This study combines analytical and experimental methods. The FRFs obtained from simulations and the experiments are quite similar to each other.

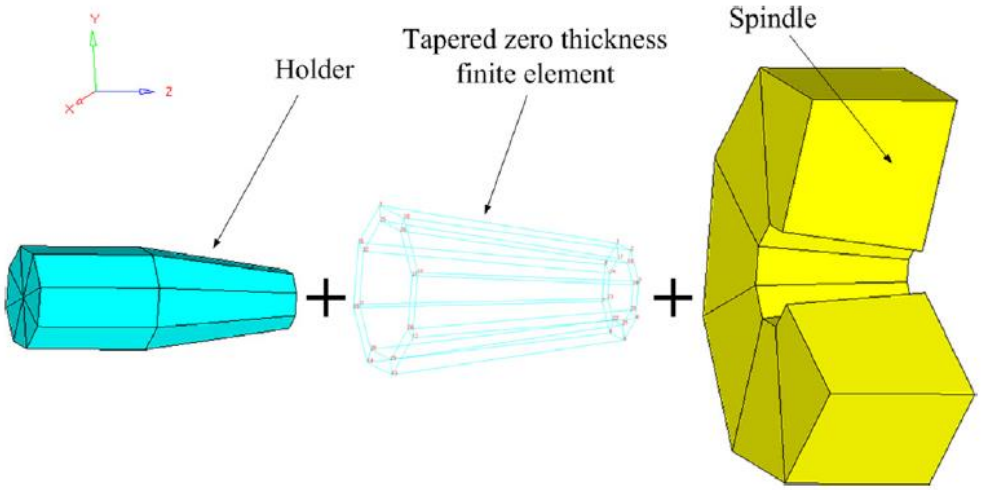

Figure 1-3 Modelling the spindle–holder taper joint with zero-thickness element [2]

Liao et al [3] used the contact force that is obtained by FEM and calculated a single stiffness value for the contact region. They used Hertz contact theory and fractal geometry theory to find corelation between the normal contact force and stiffness. In addition, Gao [4] is also used fractal geometry theory to identify contact dynamics. And they study the effect of different interference amounts, spindle speed and on tool insertion length contact stiffness. Using the stiffness values in the finite element model they calculated the FRF at the tool tip of the assembly and performing experiments they proved the validation of the method.

Xu et al [5] is also studied the dynamic behavior of the spindle-holder assembly. Using FRFs they identified the stiffness and damping values. Their main objective is investigating the effect of the force just at the end of the holder. The direction of the pre-force is demonstrated in Figure 1-4. Then, they concluded that, the contact stiffness increases as the force to hold holder increases which is expected. Then, they improved the study [6] by considering the effects of the centrifugal force due to rotation of the assembly on contact stiffness. Using experiments the validity of the method is proved.

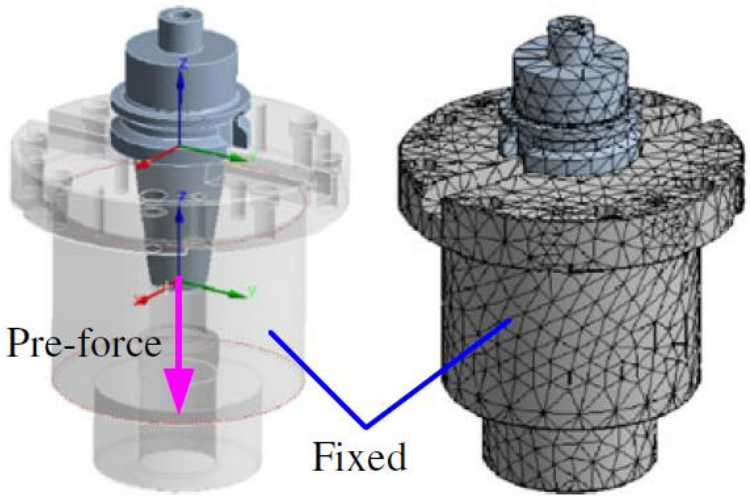

Figure 1-4 Dynamic modeling of a spindle–holder assembly [5]

Houming et al [7] are also modelled the holder-tool assembly in FEM software and perform experiments to validate the results. The model used in analysis is shown in Figure 1-5. They also considered the tool overhang length and rotational speed on the modes of the assembly and dynamic characteristics of the system.

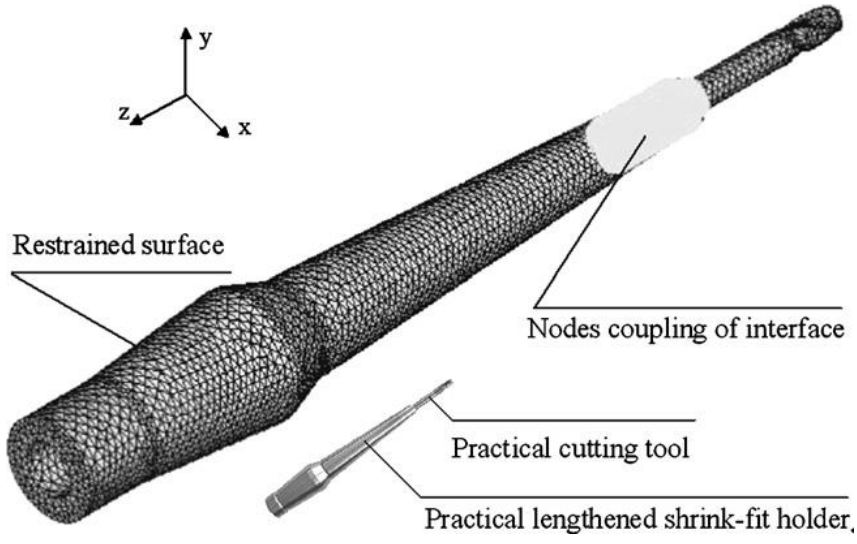

Figure 1-5 Modeling of shrink-fit holder and cutting tool for high-speed milling [7]

Finally, Brecher et al [8] studied the dynamic joint properties of the holder-tool assembly. In addition to previous works, they worked on correct modelling the the fluted section of the tool. To apply the effect of fluted section, they found an effective diameter for tool which is shown in Figure 1-6, so that the simulation results gives more accurate results.

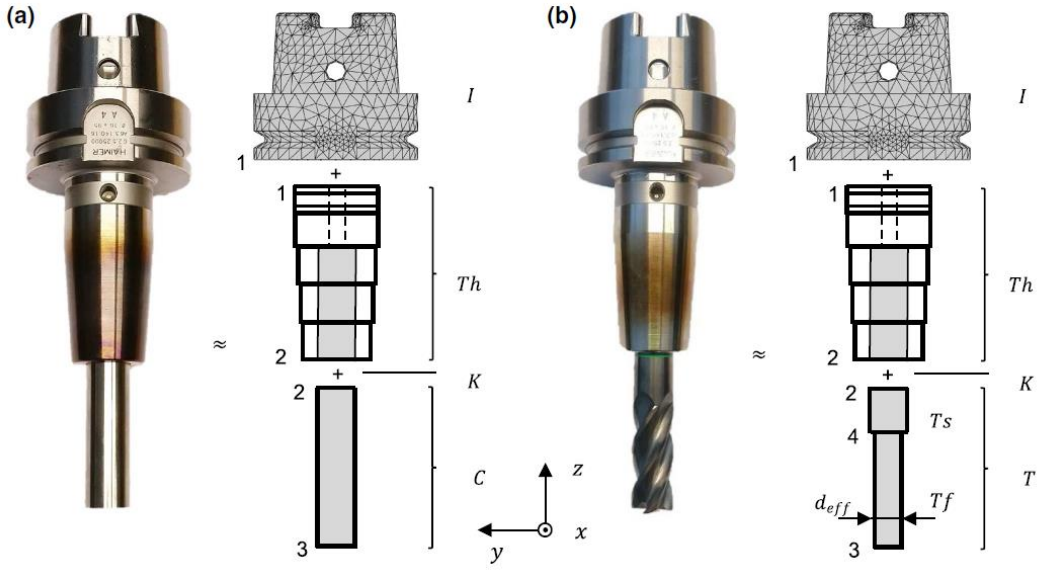

Figure 1-6 Joint identification and fluted segment modelling of shrink-fit tool assemblies [8]

In addition to using finite element methods, prediction of the contact dynamics at spindle-holder-tool assembly is mostly done by using RSCA method [9-19]. Firstly, the FRFs of the subassemblies are calculated analytically, then using experiments the tool point FRF is obtained. Afterwards, using IRSCA method the dynamic properties of the contact region is found.

Özşahin et al. [20] used inverse RCSA to identify the dynamic stiffness and damping values for holder-tool connection. Erturk and Matthias et al. [21-22] are also worked on a similar subject. Closed form expressions of the elastic RCSA equations are obtained and the results of the experiments are used. Receptance matrices calculated

using Timoshenko beam theory is also used in the formulations. The closed form expression to find complex stiffness matrix is given Equation 1.2. Özşahin et al. [23] also work of the effect of fluted section of the asymmetric tools. Because the geometry is asymmetric the tool tip FRFs changes.

$$[K_{ht}] = \left[\left[\left[H_{ht,12}\right]^{-1}\left[\left[H_{ht,11}\right] - \left[H_{sht,11}\right]\right]\left[H_{ht,21}\right]^{-1}\right]^{-1} - \left[H_{t,22}\right] - \left[H_{s,11}\right]\right]^{-1} \quad (1.2)$$

Kiran [24] treated the part of tool inside the holder as an elastic component, and he calculated translational and rotational receptances analytically. Using experiment, he measured the translational receptances and compared them with analytically measured ones. Albertelli et al. [25] considered the contribution of the rotation and moment on the receptances which limits the accuracy of the IRCSA method.

Ealo et al. [26] is also used IRCSA to examine the joints of a horizontal milling machine. The IRCSA method is mostly used to find dynamic properties of two-dimensional connections by measuring a few FRFs of the assembly. However, they used the IRCSA method to find dynamic properties of three-dimensional connections without using considerable number of FRFs to avoid ill-conditioning. And they used only the measurement of the translational DOFs. A finite element model is created, and standalone experiments are performed to obtain FRFs of the assembly and prove the validity of the study.

Ahmadi et al. [27] used an alternative approach to calculate machine tool dynamics. An elastic interface layer is considered at the tool-holder contact region. Using the distributed elastic layer, the contact pressure can be considered. Figure 1-7 shows that the elastic layer acts as a distributed stiffness. Experiments are performed to show the efficiency of the method.

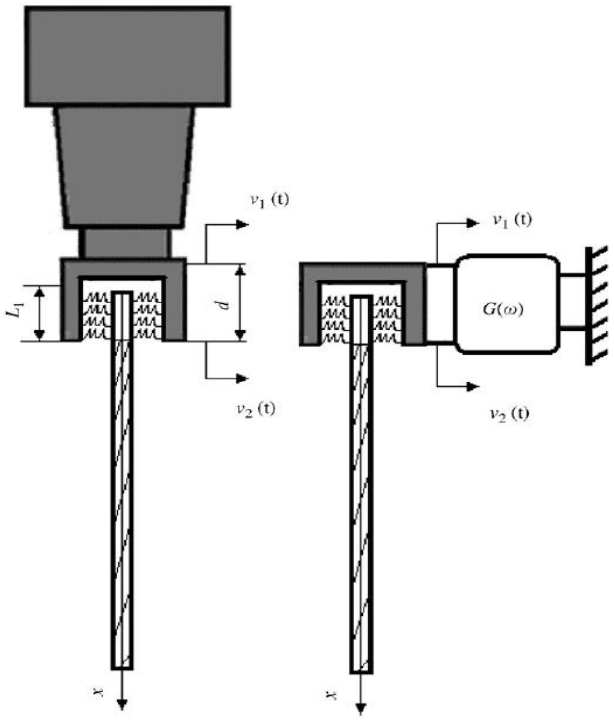

Figure 1-7 Modeling the machine tool dynamics [27]

Yiğit et al. [28] examined the non-linear receptance coupling to find dynamic characteristics. The method shows that joint non-linearities have a significant effect on dynamic stiffness. And experiments are performed to show validity of the method.

Yang et al. [29] included the effect of the collet to the dynamic characteristics of the holder-tool assembly. They divided the whole assembly into two parts, collet-holder and collet-tool assembly. Using Euler-Bernoulli beam theory, dynamics of the collet and the tool is analyzed, and the contact region is considered as zero-thickness elastic layers. Using experiments, similarity of predicted and measured FRFs are shown and validity of the method is proved.

Liao et al. [30] proposed a new method to find rotational receptances using translational receptances, so that performing only one experiment the rotational receptances can be calculated using receptance coupling technique. This method reduces the required number of tests and significantly increase the efficiency of the RCSA method.

Schmitz et al. [31-36] used a combined experimental and analytical methods for their earlier works to predict FRFs of the spindle-holder-tool assembly using RCSA method. This method used only displacement vs force receptances. This result in the other three receptances became zero. Then they improved the method using Euler-Bernoulli method to calculate all four receptances of the spindle-holder-tool system to achieve the exact solution.

Area and area moment of inertia of the fluted tool can be calculated using FEM software. Tunc [37] used stereolithographic (STL) slicing algorithm to find cross sectional properties to use in RCSA method as given in Figure 1-8. He achieved that using this method cross sectional properties can be found with more accurate and faster way.

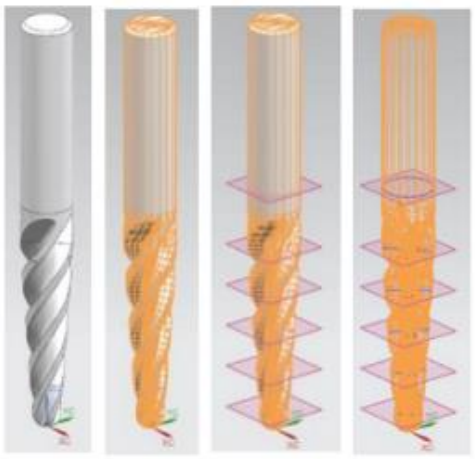

Figure 1-8 STL Slicing of tool tip [37]

IRCSA method can be used to find dynamic properties of the contact region of assemblies other than holder-tool. For instance, Chen [38] used the IRCSA method to find dynamic properties of motor-shaft contact region. They first calculated the contact pressure. And performed modal analysis including the contact pressure as a pre-stress. Then they performed tests to prove validity and accuracy of the method.

Tol et al. [39] used FRF decoupling method to find dynamic properties of bolted contacts. They measured and also calculated the FRFs of the assemblies. Then using FRF decoupling method they found direct and cross stiffness and damping values for contact region. To eliminate the effect of the noise in the experimental result, they used an optimization algorithm. Then they performed tests to prove validity of the method.

1.3 Objective

The aim of this thesis is to identify the dynamic properties of contact regions. For this purpose, holder-extension and extension-tool assemblies are modelled using Finite element software. Since performing tests for every combination is not efficient, it is aimed to use simulations to obtain dynamic parameters. Using this method results in finding dynamic properties in a much more efficient and faster way. Besides, dynamic properties are also found using inverse RCSA. In theory, both methods should give comparable results.

1.4 Scope Of the Thesis

Outline of the thesis is as follows:

In Chapter 2, the finite element model is presented. For preprocessing and postprocessing stages MSC PATRAN is used. To solve the simulation MSC NASTRAN is used. Using 3D hex and wedge elements, the holder, extension and tool are modeled. The contact parameters are set, and the contact dynamic properties are found by running the simulation. Linear and nonlinear analysis are performed, and the results are compared. In addition, the effects of the assembly parameters are examined.

In Chapter 3, contact parameter identification theory are given in the closed form. The receptance coupling equation is used to obtain a closed-form for contact parameters identification and the dynamic properties are calculated. Different matrix inversion methods are examined to find effective method for calculating the dynamic properties.

In Chapter 4, experimental studies are presented to validate the Finite element model and the receptance coupling method. Because of this, modal testing is used to measure displacement-force receptance values of the holder-extension and holder-extension-tool assembly. The tip point FRFs are compared for the extension-holder assembly and holder-extension-tool assembly. In addition, different combinations of extension and tool overhang length are considered. Performing tests with new combinations, applicability of the FEM results proved. Then the dynamic properties of the contact regions are recalculated using experiemental results and compared with the result obtained from PATRAN.

In Chapter 5, summary and conclusion of the thesis is provided. The scope of potential future work is also suggested.

CHAPTER 2

FINITE ELEMENT MODELING

In this section, holder-extension-tool assembly is modeled using Finite Element Modelling (FEM). For the modeling of the shrink fit connnections at the holder-extension and extension-tool interfaces 3D Hex elements are used in MSC PATRAN. Then from the static analysis, interface parameters are identified and effects of interface parameters and the clamping conditions on contact stiffness are analyzed through constructed FE model.

2.1 Creating the Model

A 20 mm diameter steel extension (HAIMER 77.202.08) is inserted in the HAIMER steel shrink fit holder (HAIMER A63.140.20) and the tool (HAIMER F2004NNH0800CDA) is inserted to extension as shown in Figure 2-1. Technical drawings of the holder, extension and tool are given in Figure 2-2 to 2-4 and dimensions of the holder, extension and tool are also given in Table 2-1 to 2-3 respectively.

Figure 2-1 Holder-extension-tool assembly

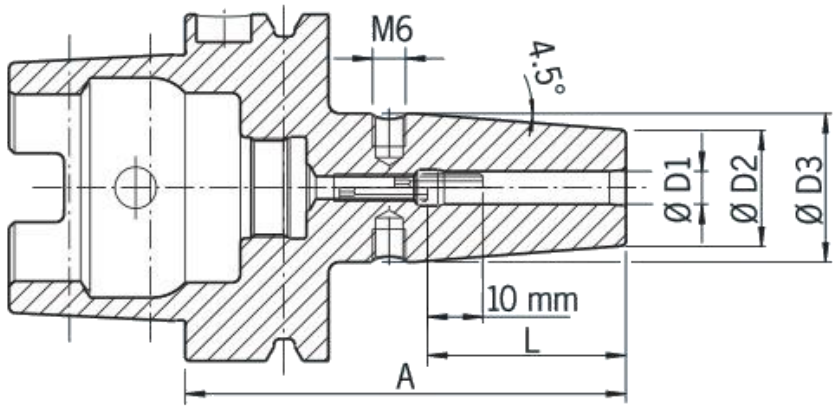

Figure 2-2 Technical drawing of the holder [41]

Table 2-1 Dimensions of the holder

Ø D1 [mm]	Ø D2 [mm]	Ø D3 [mm]	L [mm]	A [mm]
20	33	42	52	100

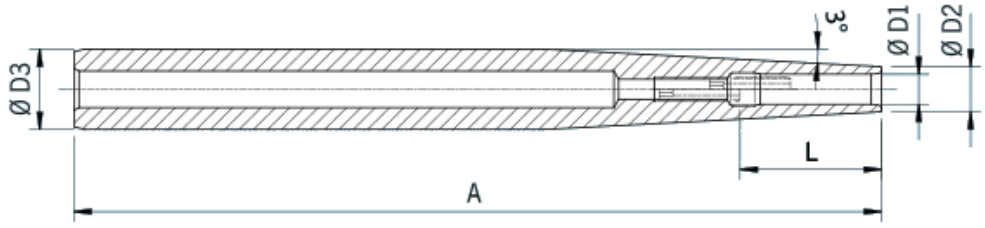

Figure 2-3 Technical drawing of the extension [42]

Table 2-2 Dimensions of the extension

Ø D1 [mm]	Ø D2 [mm]	Ø D3 [mm]	L [mm]	A [mm]
8	14	20	34	200

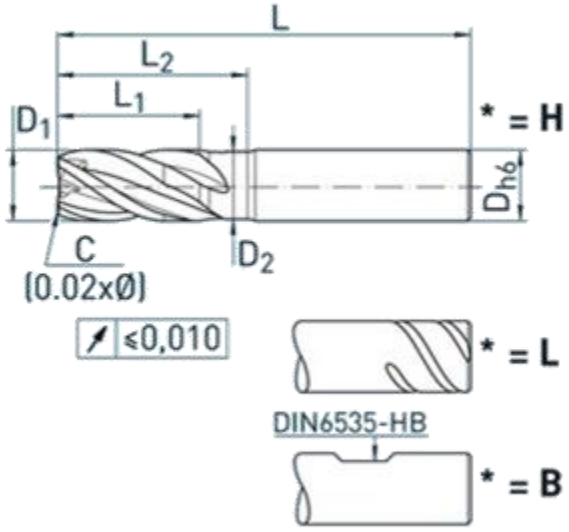

Figure 2-4 Technical drawing of the tool [43]

Table 2-3 Dimensions of the tool

Ø D1 [mm]	Ø D2 [mm]	Ø D3 [mm]	L_1 [mm]	L_2 [mm]	L [mm]
8	7.6	8	19	26	64

For the defined geometry, holder-extension-tool assembly (Figure 2-1) is modeled in MSC PATRAN as shown in Figure 2-5. In the model 22920 8-node cubic elements (HEX8) and 816 Wedge6 elements are created which consisted of 28478 nodes. The x direction is along the tool axis, the y direction is horizontal, and the z direction is vertical direction. Because there is no gravitational force in the model, rotation of the holder-extension assembly can't cause any problem. 52 mm of the extension is inserted into the holder and 18 mm of the tool is inserted into the extension. The holder and the extension are both made of steel, the tool is made of carbide. The material properties are also given in Table 2-4, where E is the elastic modulus, ρ is the density and ν is the Poisson's ratio. Friction coefficient μ between steel holder and steel extension is 0.7, and friction coefficient μ between steel extension and carbide tool is 0.5.

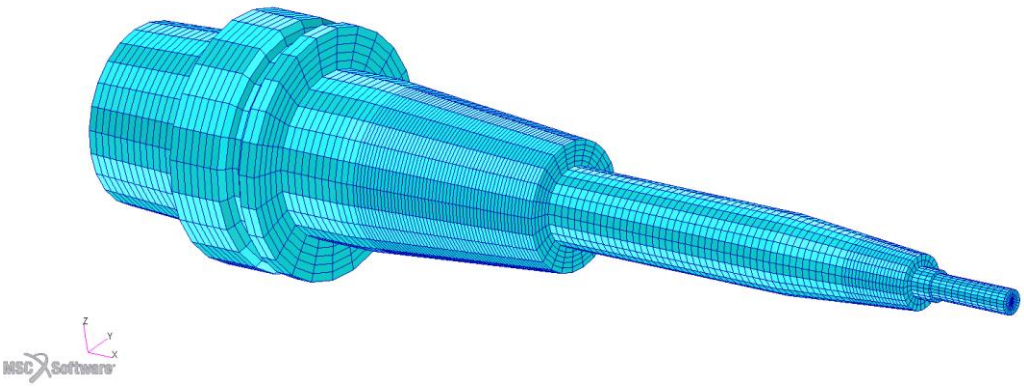

Figure 2-5 Finite Element Model

Table 2-4 Material Properties

	E [GPa]	ρ [kg/m^3]	ν
Holder	200	7850	0.29
Extension	200	7850	0.29
Tool	560	14400	0.22

The extension has shrank tolerance of h6. For 20 mm extension h6 shrank tolerance is about 0-12.7 μm. The touching contact property is set at the interface between holder and extension with 10 μm radial interference. The tool has also shrank tolerance of h6. For 8 mm tool h6 shrank tolerance is about 0-9 μm. The touching contact property is set at the interface between extension and tool with 9 μm radial interference which is close to interference of extension. The interference amount is set using Interference Closure (CINTERF) property card in Geometric Contact Parameters tab. CINTERF value defines the interference amount of two touching nodes in unit of milimeters. Therefore, to obtain 10 μm radial interference, CINTERF value should set as 0.01. The nodes of the elements of the holder and the extension should overlap to run interference fit analysis as shown in Figure 2-6.

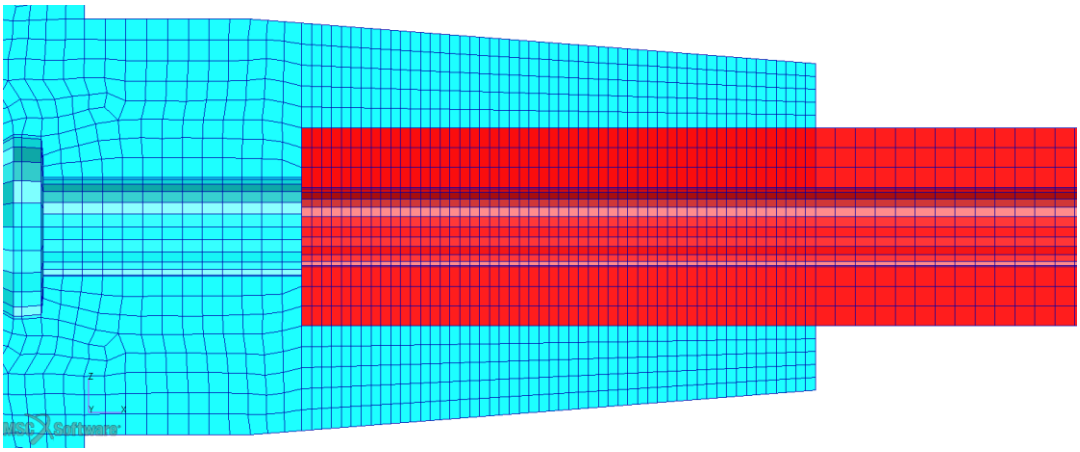

Figure 2-6 Overlapping nodes

To identify the contact parameters force-displacement relationship is used. A z direction 2000-N force is applied to the extension after the end of the contact. The

magnitude of the force is taken arbitrary. Effect of the magnitude of the applied force will be discussed in next section. 75% of the inserted force is applied at inner top three nodes and 25% of the force is applied to two outer nodes to minimize localized deformation effects. Figure 2-7 shows the force distributions.

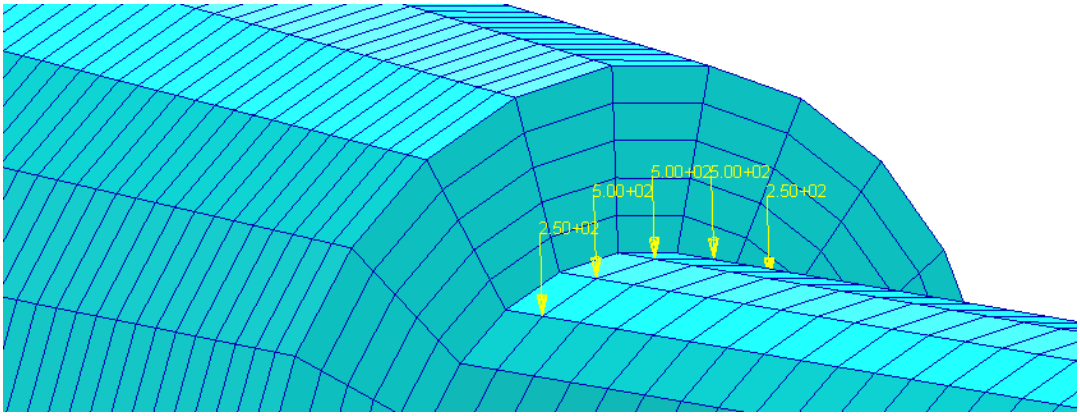

Figure 2-7 Applied forces on the extension

To find the dynamic properties caused by momentum, a 20 Nm momentum is applied to the extension after the end of the contact. Because the 3D element cannot carry rotation, applying momentum directly to the 3D element don't give any result. Therefore, instead of applying momentum directly, a force couple is is applied. The diameter of the extension is 20 mm, so 1000 N force couple is applied at the top and bottom of the extension. Figure 2-8 shows the applied force couple.

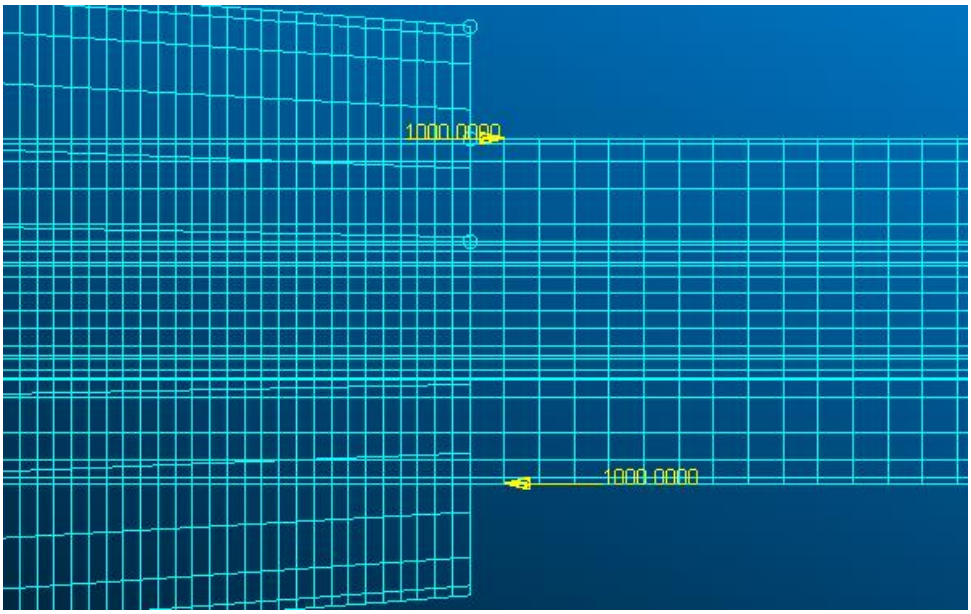

Figure 2-8 Applied force couple on the extension

The force is applied in 5 fixed increments with 1-second total time. In other words, in every 0.2 second 20% of the force is applied to the model. Force application is shown in Figure 2-9.

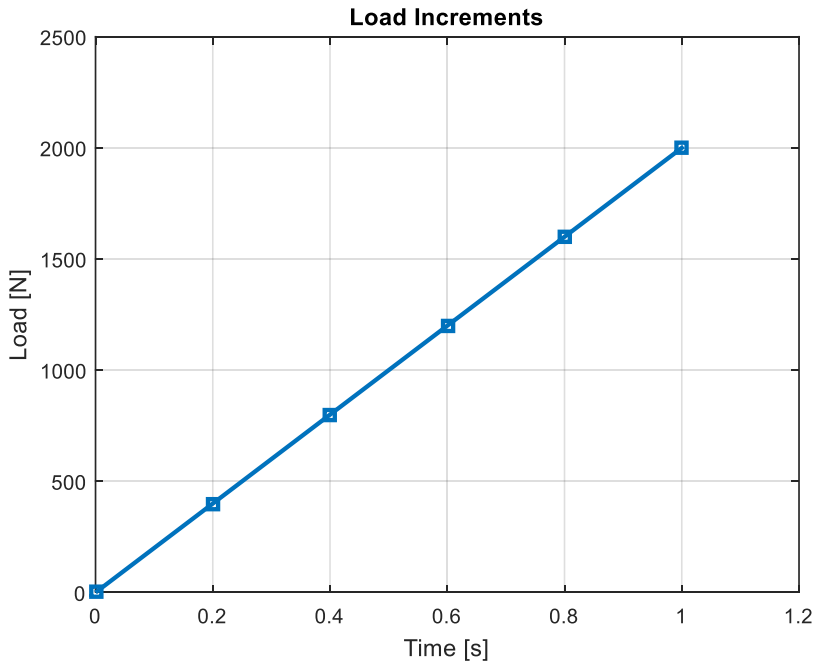

Figure 2-9 Load increments used in the simulation

Figure 2-10 and 2-11 demonstrates the contact stress profile for the extension and the tool. The units of the stress values are MPa. As expected the contact stress is concentrated at the bottom of the contact region, because the outside geometry is thicker at the bottom of the contact region and more resistant to deflection.

Figure 2-10 Contact stresses of the extension

Figure 2-11 Contact stresses of the tool

2.2 Calculating The Stiffness at the Interface

By using the finite element model mentioned in the previous section linear static analysis is performed. Then, the translational and rotational stiffness values across the contact region are determined using displacement results. SOL101 is used for linear static analysis, but it cannot solve the model with load increments. Therefore, SOL400 is used instead of SOL101. Running 5 analysis with SOL101 and running only one analysis using 5 load increment with SOL400 gives the same results. At every load increment the displacement values at the z axis of the extension at the nodes across the extension upper midline are enlisted. Using the load vs displacement slopes for every node, the k_{yf} translational stiffness values are calculated. For example, the displacement values according to the applied forces for the first node at the contact region is shown in Figure 2-12 and the equation of the trendline of the curve is given in equation 2-1. Therefore, the k_{yf} stiffness value at this node is calculated as $7.42*10^7$ N/m. As expected, when the force increases, the displacement values also increase.

$$y = 7.42 * 10^7 x - 509.53 \quad (2.1)$$

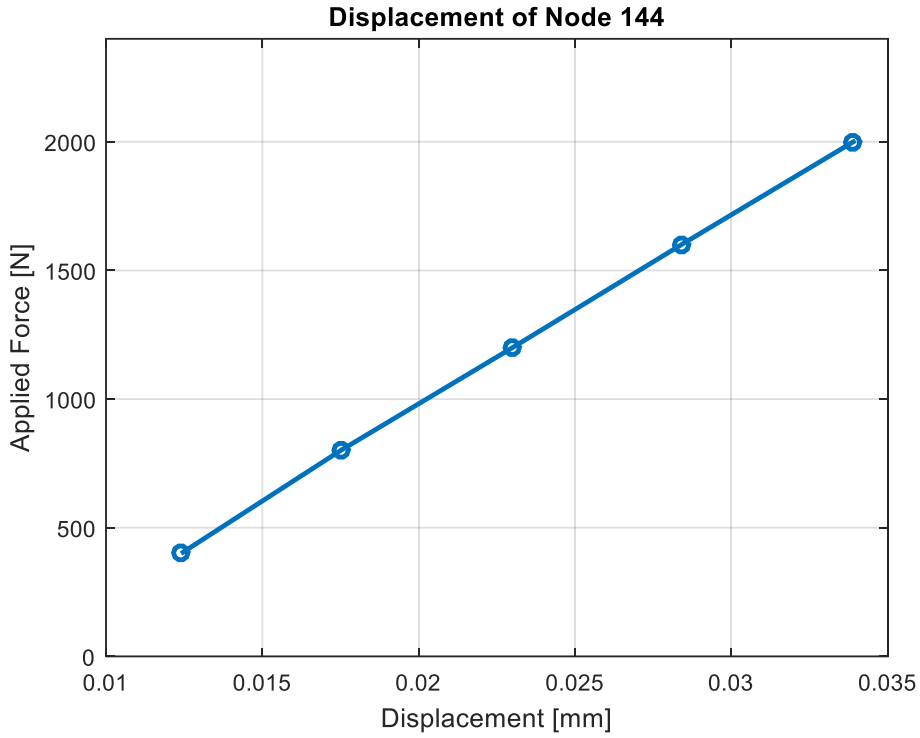

Figure 2-12 Displacement values of node 144

For $k_{\theta f}$ rotational stiffness values, first the rotation is found using central difference of the displacement values in z axis. Then the rotational stiffness values are calculated using the load rotation curve. For example, to find rotational stiffness of the node located at 0.07 m in x direction for the first load increment, the following calculations are made.

$$rotation = \tan^{-1}\left(\frac{displacement\ of\ next\ node - displacement\ of\ previous\ node}{location\ of\ next\ node - location\ of\ previous\ node}\right) \quad (2.2)$$

$$rotation = \tan^{-1}\left(\frac{0.01086-0.01061}{0.071-0.069}\right) = \tan^{-1}(0.128) = 0.0022\ rad \quad (2.3)$$

Using the same procedure, the rotation is calculated in every 5-load increment. The rotation-load curve is given in Figure 2-13. The slope of the curve gives rotational stiffness values which is $2.21*10^5$ N/rad.

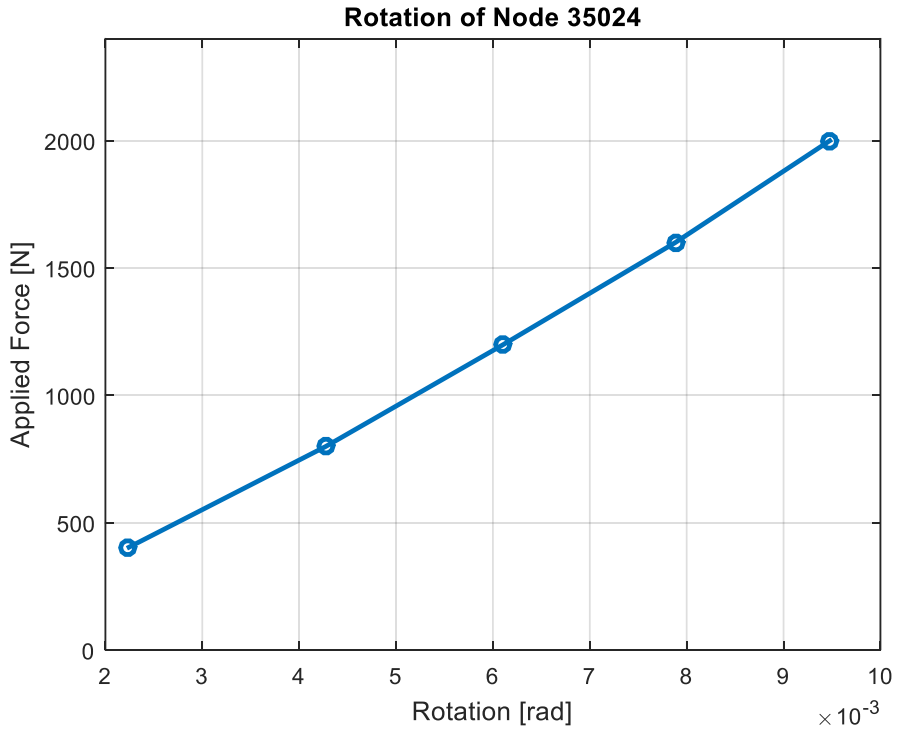

Figure 2-13 Rotation values of node 35024

The k_{yf} and $k_{\theta f}$ stiffness values for the contact region are given in Figure 2-14 and Figure 2-15. Because there is a numerical noise in finite differences, the rotational stiffness curve is not smooth as translational stiffness curve. In addition, it is seen that the stiffness values are decreasing towards the end of the contact region. The main reason of this result is the stiffness values are related to contact stress and the contact stress is also decreasing towards the end of the contact region.

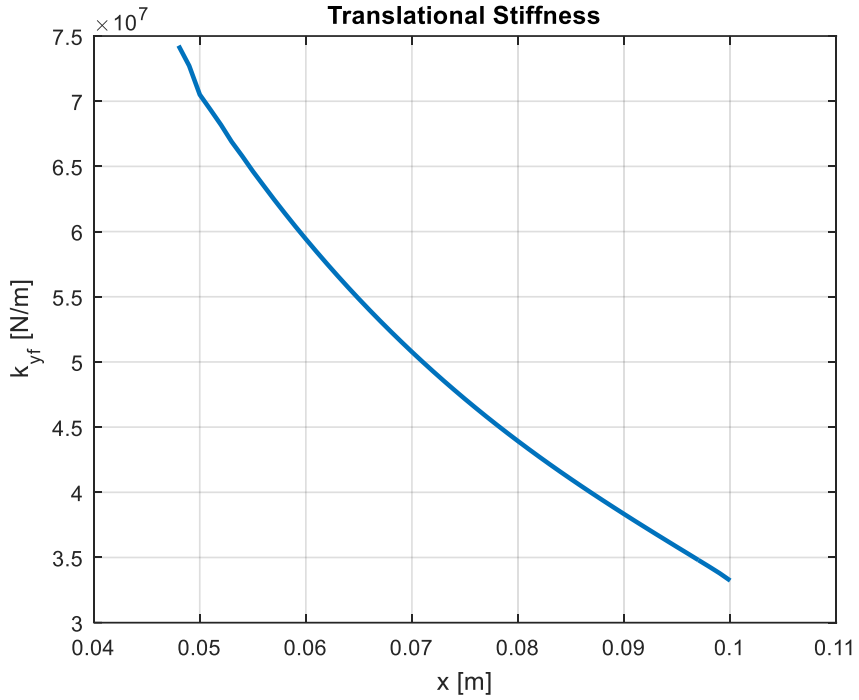

Figure 2-14 Translational stiffness values due to force at holder-extension interface

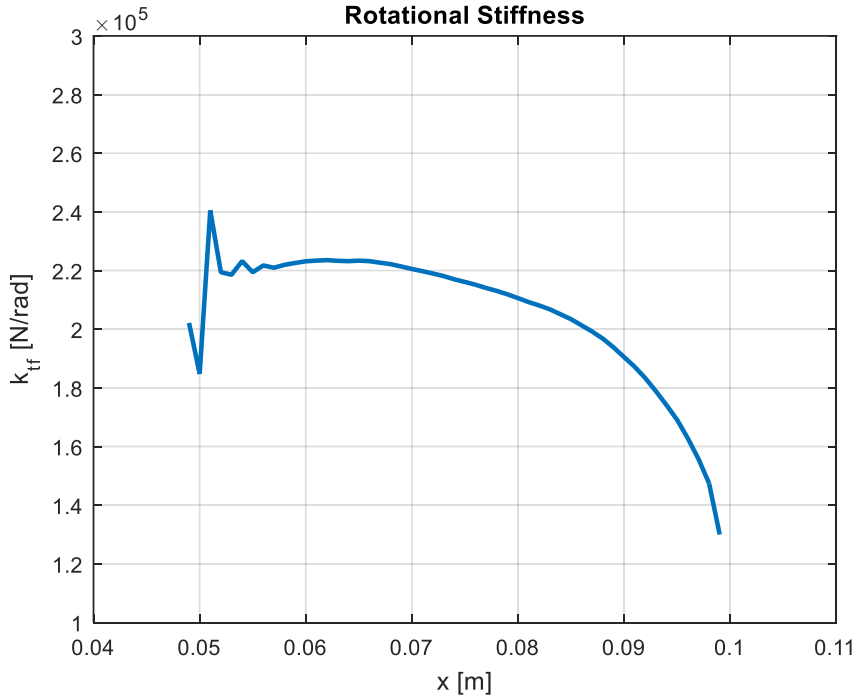

Figure 2-15 Rotational stiffness values due to force at holder-extension interface

Using the same method 20 Nm force couple is also applied to the extension and translational and rotational stiffness values calculated for the extension. The k_{ym} and $k_{\theta m}$ stiffness values for the contact region are given in Figure 2-16 and Figure 2-17.

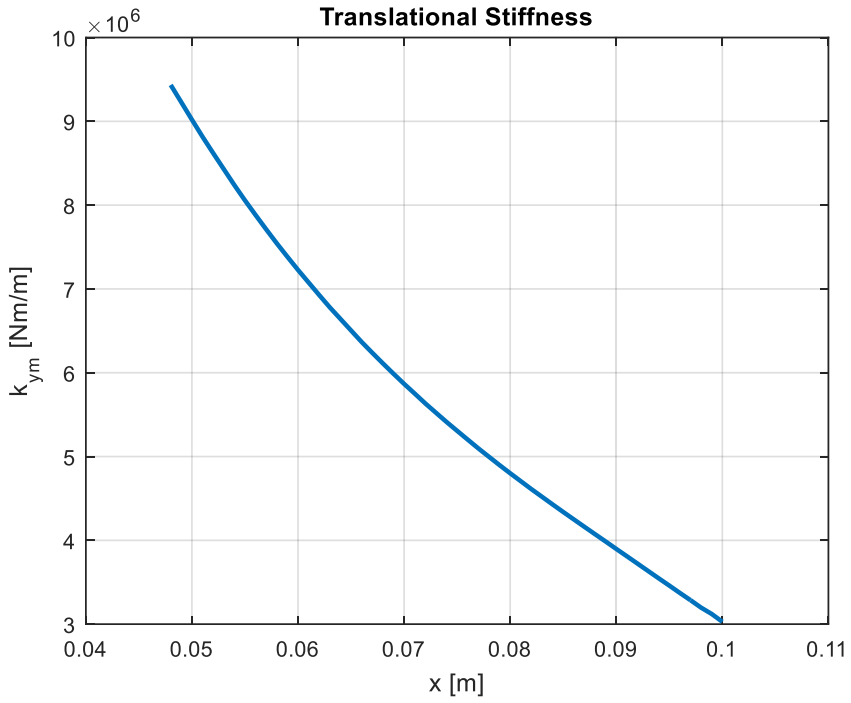

Figure 2-16 Translational stiffness values due to moment at holder-extension interface

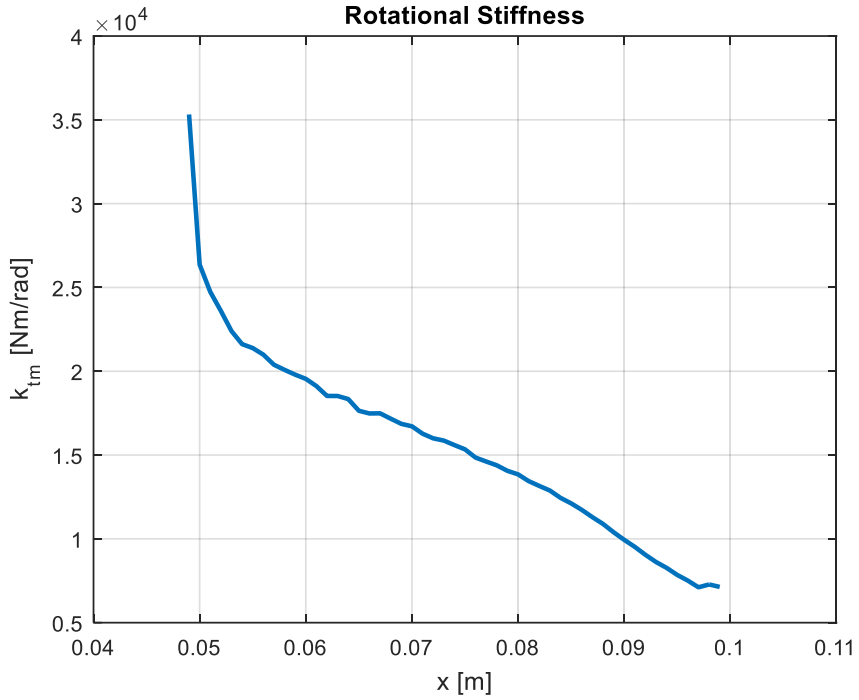

Figure 2-17 Rotational stiffness values due to moment at holder-extension interface

After adding the tool to the Finite Element Model, the translational and rotational stiffness values due to force and moment is calculated for tool-extension contact region. The $k_{yf,}$ $k_{\theta f}$, $k_{ym,}$ $k_{\theta m,}$ stiffness values for the tool is given in Figure 2-18 to 2-21.

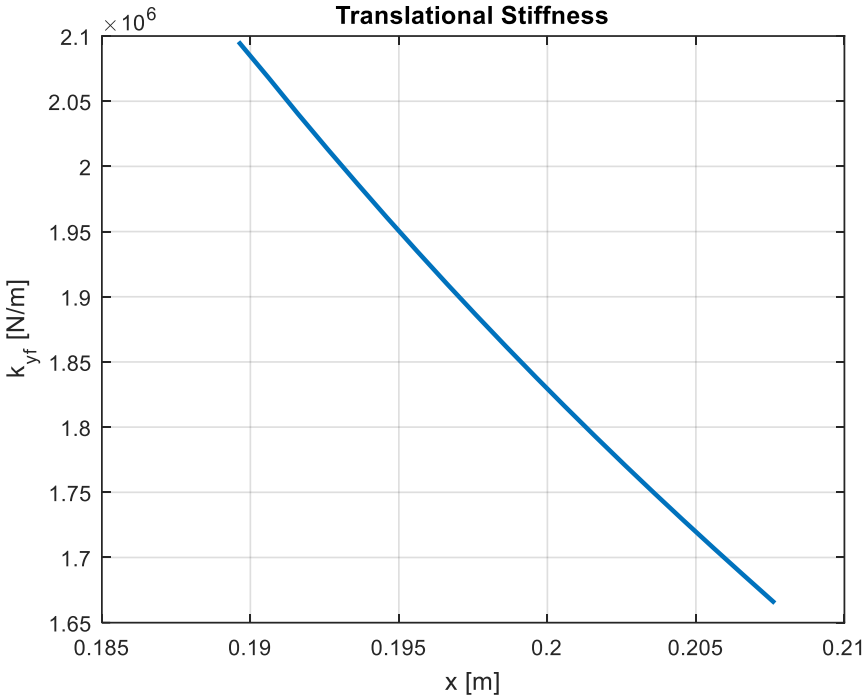

Figure 2-18 Translational stiffness values due to force at extension-tool interface

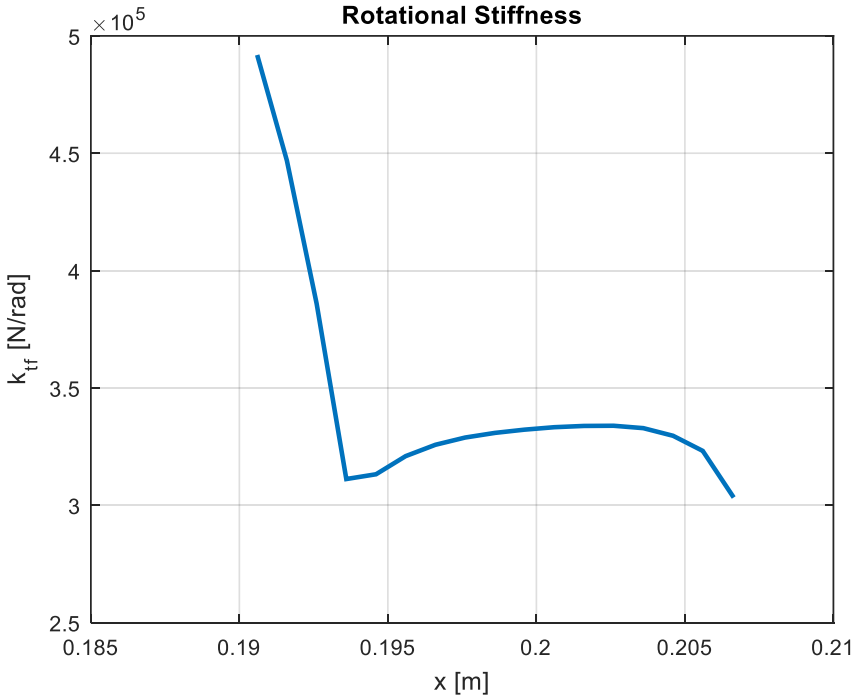

Figure 2-19 Rotational stiffness values due to force at extension-tool interface

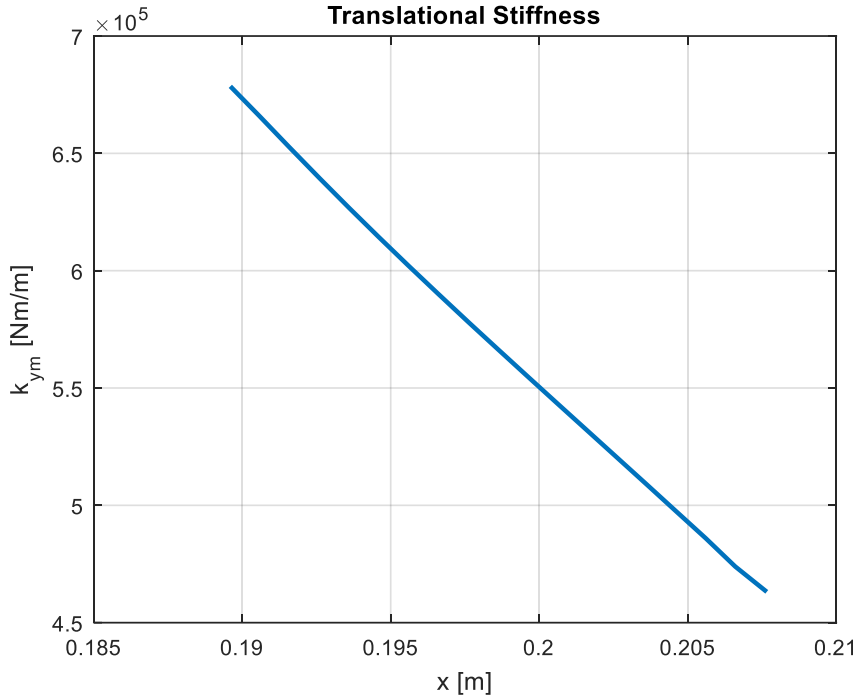

Figure 2-20 Translational stiffness values due to moment at extension-tool interface

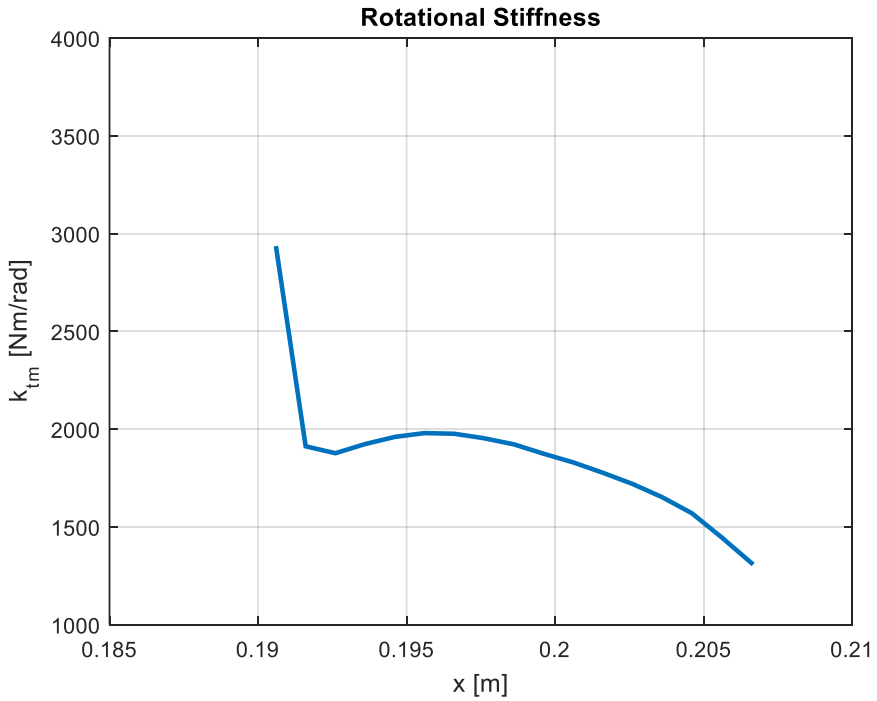

Figure 2-21 Rotational stiffness values due to moment at extension-tool interface

Schmitz et al [1] also find the translational stiffness values linearly decreasing towards to end of the contact region and rotational stiffness values are also decreasing but with numerical errors. The magnitude of the stiffness values are close to values at the holder-extension interface.

2.3 Effect Of Assembly Parameters and Machining Conditions on Contact Stiffness

In this section different assembly parameters and machining conditions are used to find their effects on stiffness values using linear analysis.

First, different values for applied load are used. 1250 N, 2000 N and 5000 N force is applied. Because the external force is selected arbitrarily, its effect on the dynamic properties must be examined. Figure 2-22 shows that translational stiffness values are not sensitive to applied force. The reason of this result is the load-displacement curve is used to determine stiffness values. When the force changes, the displacement values also change accordingly. Therefore, the slope of the load-displacement curve is constant.

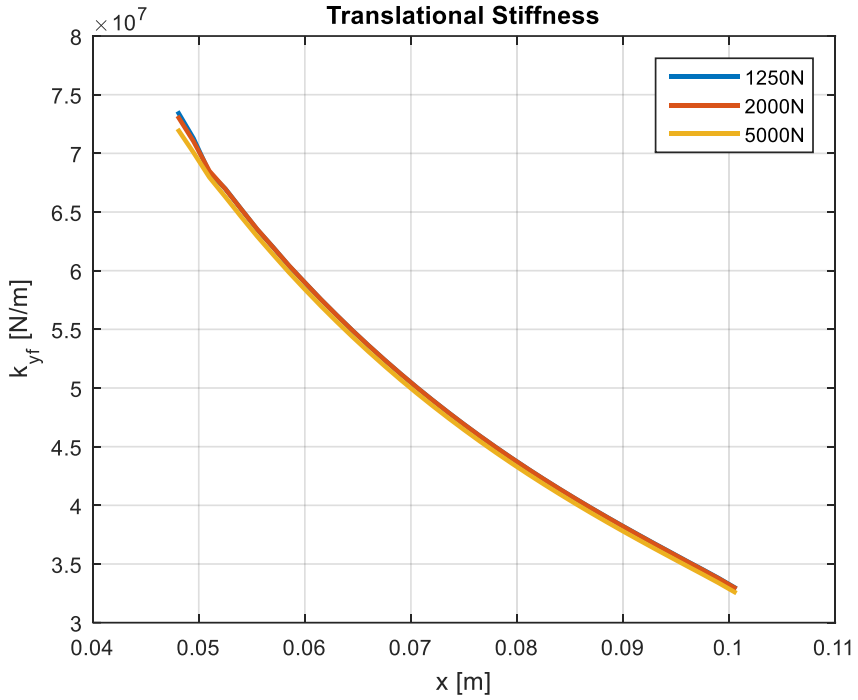

Figure 2-22 Effects of applied force on translational stiffness value at the holder-extension interface

However, as seen in Figure 2-23, rotational stiffness values are sensitive to applied force. The rotational stiffness also increases when the applied force increased. For translational stiffness values displacement values at the z axis are used, however for rotational stiffness values the rotation is used. When the applied force changes the rotation of the nodes does not change linearly. For the forces with relatively small magnitude the stiffness values are close to each other. The difference of the values for the 5000 N applied force may be caused by computational errors.

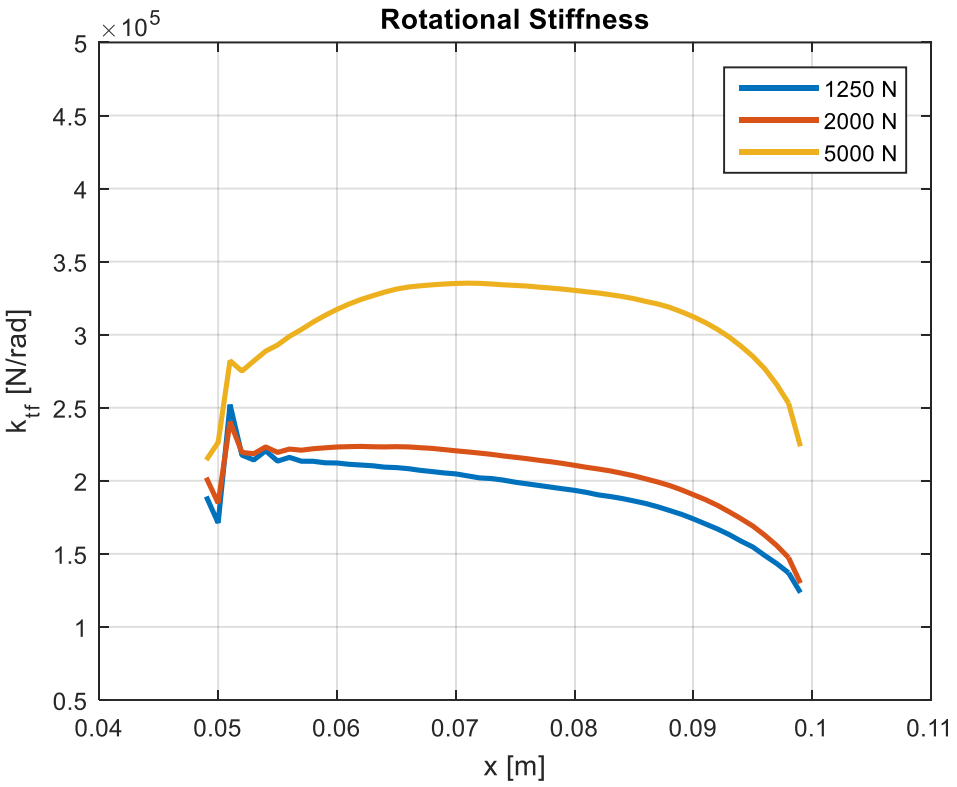

Figure 2-23 Effects of applied force on rotational stiffness value at the holder-extension interface

The external forces are applied just at the end of the contact region to determine dynamic properties. However, during machining operation, axial forces at the tip of the tool occurs. Comparison of these two situations are demonstrated in Figure 2-24. When the load is applied at the tool tip, the nodal displacement values increases, because the distance to the end of the tool also increases. In previous analysis, the displacement values increase with the applied force, so the slope of the load-displacement curve could remain same. However, when the application location changes, although the magnitude of the load remains the same, the displacement increases. This results in a decrease in translational stiffness values towards the end of the holder-extension interface. The maximum difference between two stiffness values is 3%. Therefore, the effect of the applied load location can be ignored.

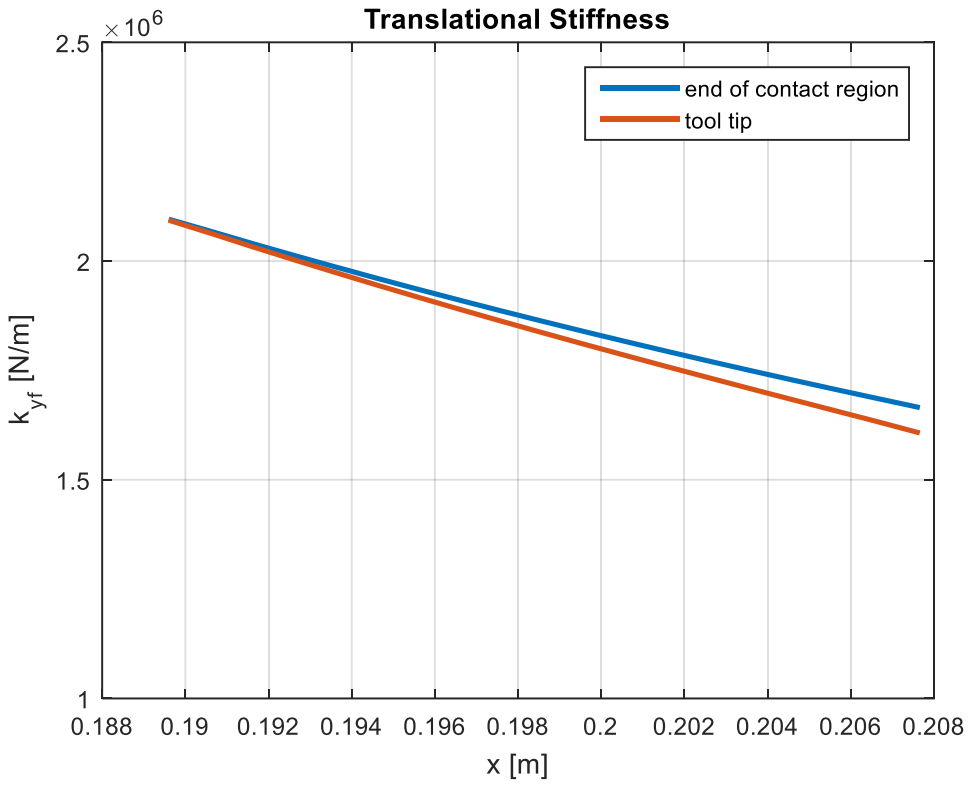

Figure 2-24 Effects of the location of 2000 N applied force on translational stiffness value at the extension-tool interface

To investigate the effect of interference on contact dynamics, different interference values (5 µm, 10 µm and 50 µm) are used at the holder-extension interface. For 50 µm, at the end of the extension the stiffness values are quite different from other cases but it could be computational error. For other values the translational stiffness values are not sensitive to interference amount. Figure 2-25 shows the comparison of translational stiffness values. This is because the interference amount changes the displacement before the load is applied. However, the stiffness values are calculated using the load-displacement curve. The difference between displacements from the first and fifth load increment remains same. Therefore, the stiffness values do not change with interference amount. Schmitz et al. [1] also examine effect of the different interference amount on the translational stiffness values and concluded that the stiffness values are not sensitive to the interference amount. As seen in Figure 2-

26, the rotational stiffness values are also close to each other. For 50 μm interference, rotational stiffness values have huge error. This is caused by computational errors with huge interference. The tolerance of the extension is 0-12.6 μm and 50 μm interference is not realistic.Therefore, the results for 50 μm interference can be ignored.

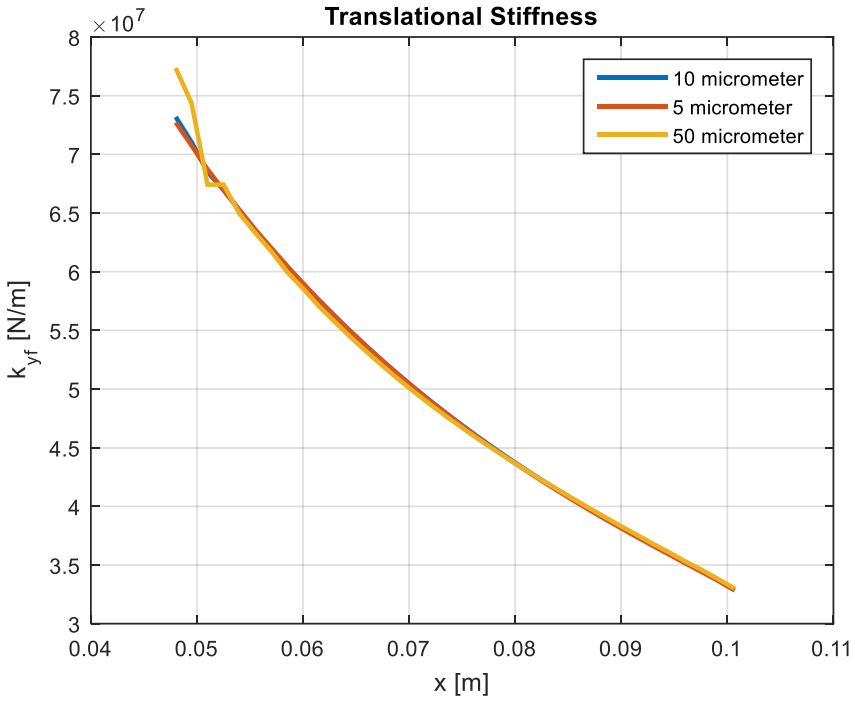

Figure 2-25 Effects of interference amounts on translational stiffness value at the holder-extension interface

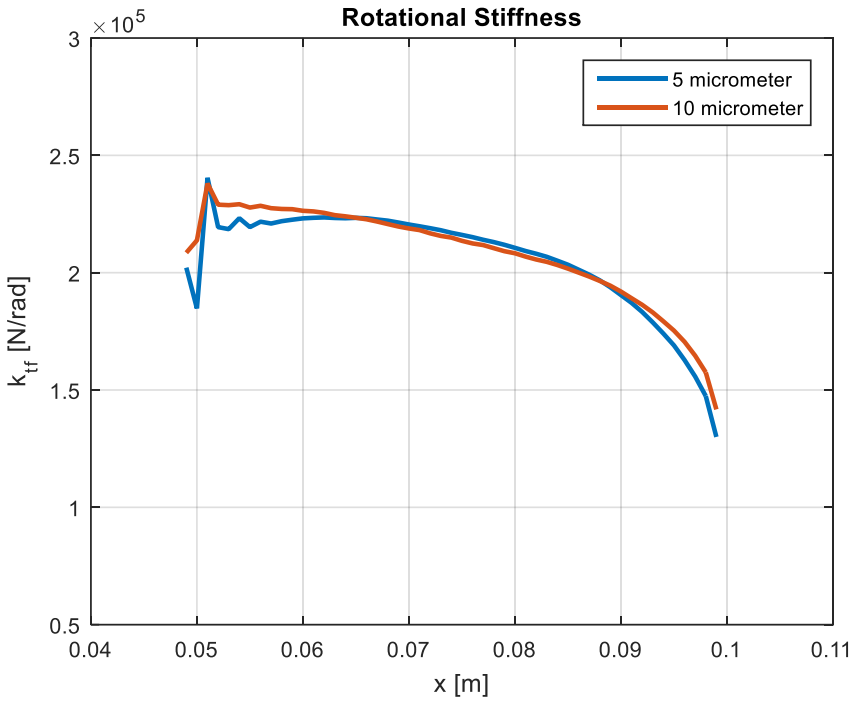

Figure 2-26 Effects of interference amounts on rotational stiffness value at the holder-extension interface

During machining operations, spindle-holder-extension-tool assembly rotates at high spindle speeds. Decrease of the bearing stiffness directly affects spindle dynamics and cause deviations in the tool point FRFs. Similarly, contact dynamics at the holder-extension and extension-tool interfaces directly affect the tool point FRFs. Therefore, to examine the effect of spindle speed on the contact parameters, contact stiffness values at the holder-extension interface are calculated under various spindle speeds (10000 rpm, 30000 rpm and 50000 rpm). 10 μm interference amount is used for all cases. The effect of the rotational speed is given in Figure 2-27. Liao et al. [3] show that, decrease in stiffness values, when the rotational speed increases is expected.

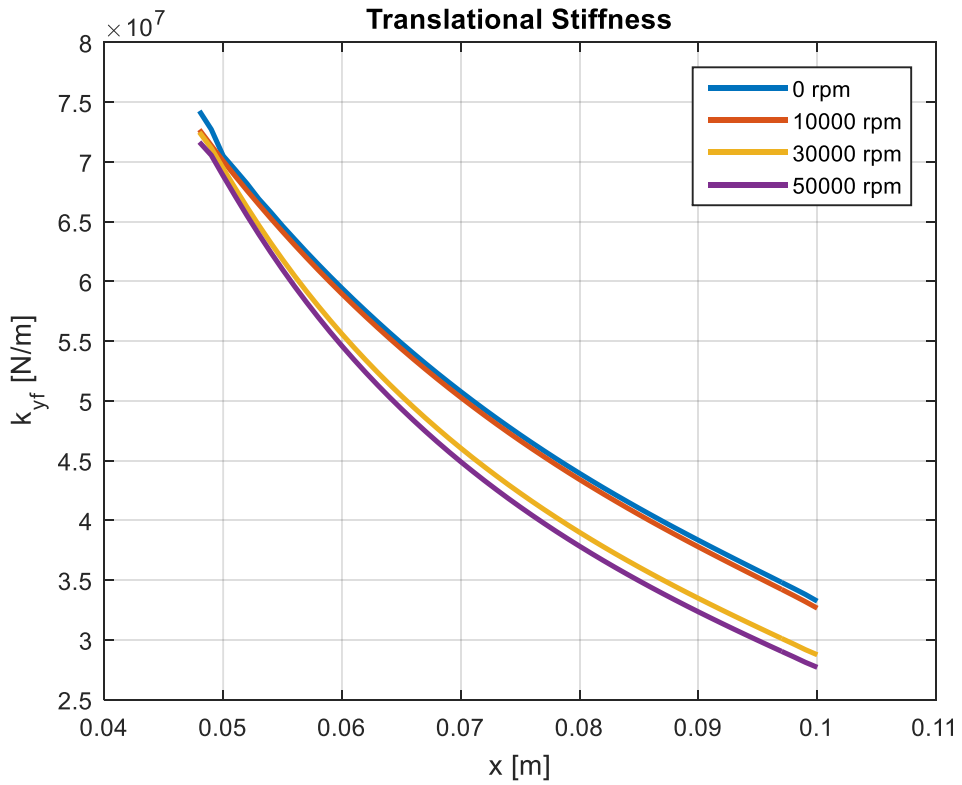

Figure 2-27 Effects of rotational speed on translational stiffness value at the holder-extension interface

In addition, different interference amounts are examined when the holder-extension assembly rotates. For this purpose, translational stiffness at holder-extension interference with 10 μm and 50 μm are compared when the model rotates at 30000 rpm. Figure 2-28 shows that, stiffness values increases slightly with the interference amount. When the assembly is stationary, the dynamic properties are not dependent to the interference amount, but when the assembly rotates, the dynamic properties also changes with the interference amount. This is because, the rotation affect the displacement of the nodes at the contact region. It is seen that, at the beginning of the contact region two stiffness values are close to each other. However, towards to end of the contact region difference between two stiffness values are increasing, because when the assembly rotates, the node towards to end of the contact region stretches more than the previous ones.

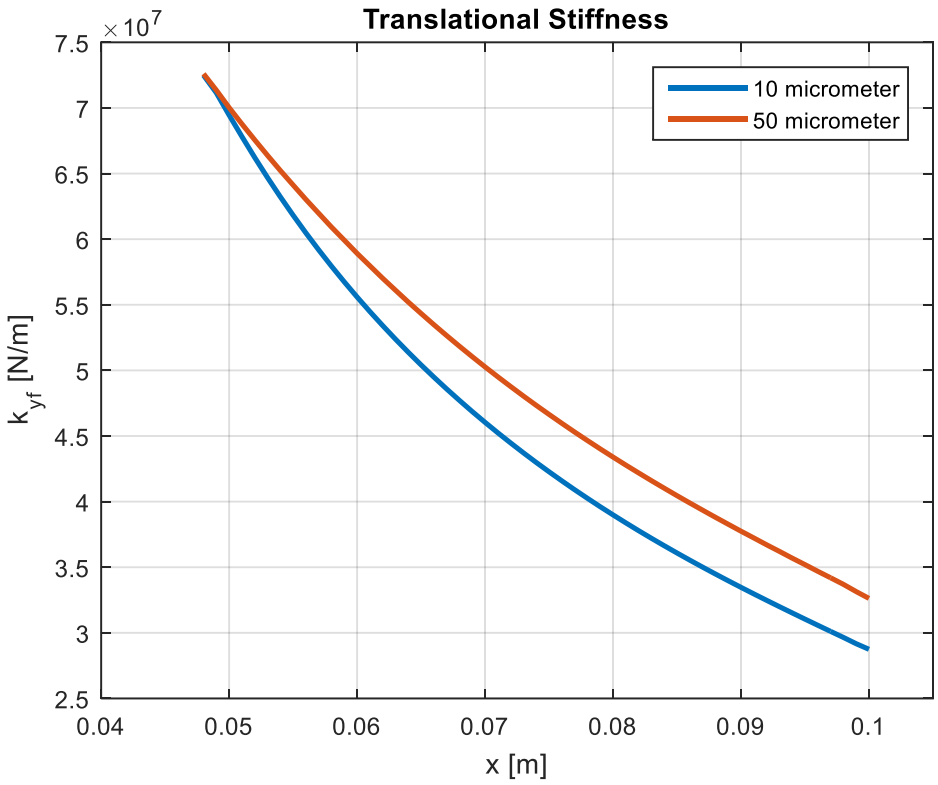

Figure 2-28 Effect of interference amount on translational stiffness at the holder-extension interface with 30000 rpm spindle speed

Lastly, the effect of the material of the tool is examined. The stiffness values are calculated for the tool made from carbide and the stiffness values are recalculated by changing the tool material to steel. 9 μm interference applied to the model. Figure 2-29 shows that stiffness values are not sensitive to material properties. Because the load application location is not close to the end of the assembly which has fixed boundary condition and the tool length inside the extension is too short compared to whole assembly, changing material properties has small effect on displacement. Therefore, its effect on dynamic properties for the tool can be ignored.

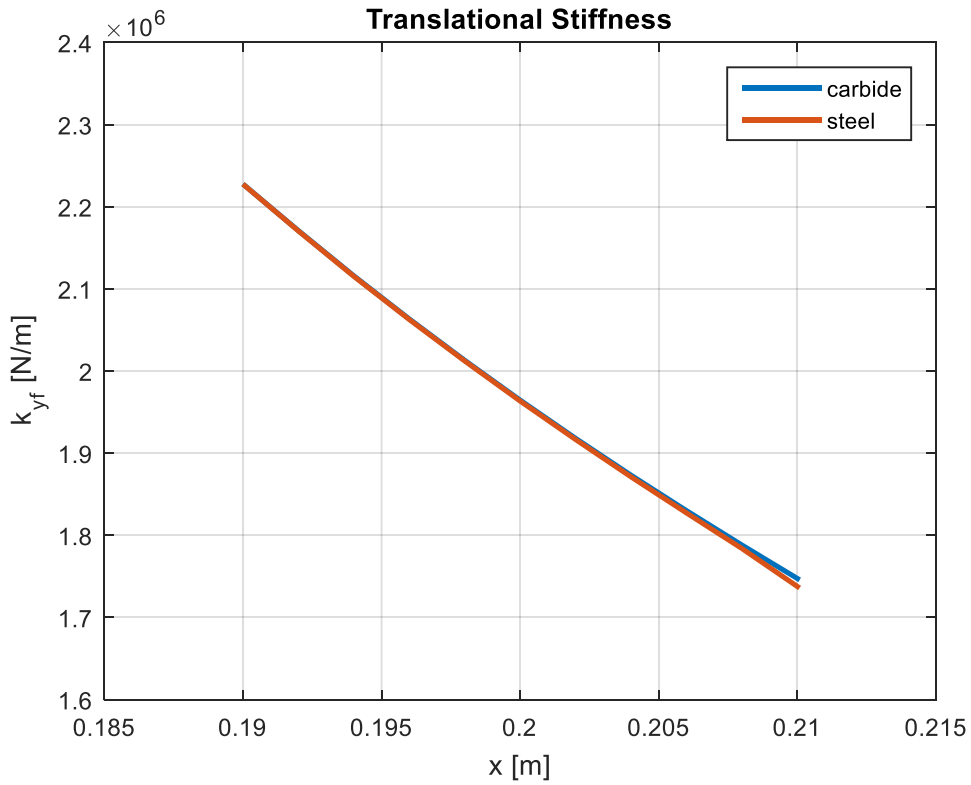

Figure 2-29 Effects of material properties on translational stiffness value at the extension-tool interface

2.4 Effect of Nonlinear Analysis on the Identified Contact Parameters

In this section different assembly parameters are used to find their effects on stiffness values using nonlinear analysis.

First, different magnitudes of applied load are used. 1250 N, 2000 N, 3000 N and 5000 N force is applied. Figure 2-30 shows that translational stiffness values are not sensitive to applied force. And, when the applied force increases the rotational stiffness also increases as seen in Figure 2-31. At the previous section, using linear analysis the same results are obtained. This means that both nonlinear and linear analysis do not depend on the external load.

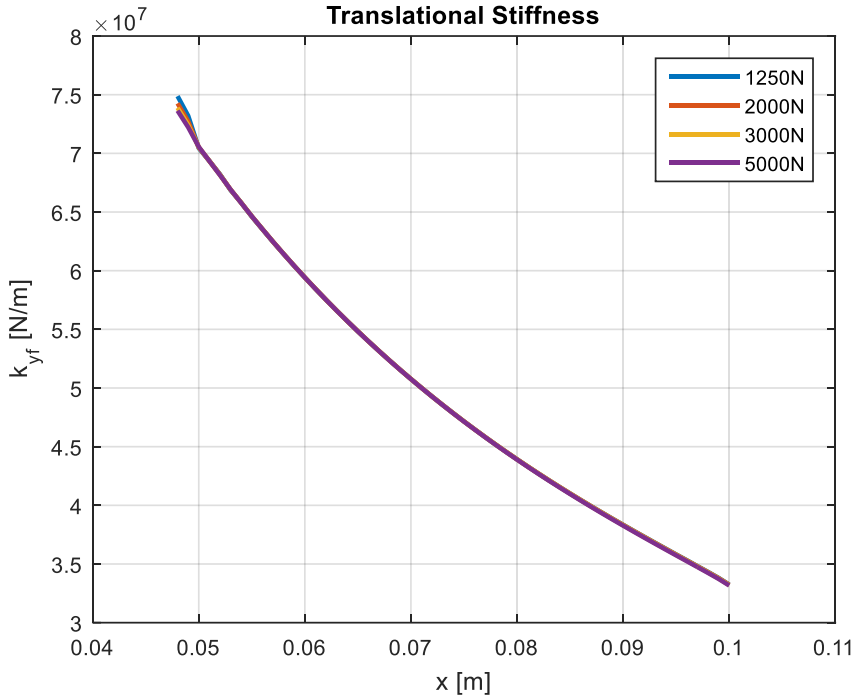

Figure 2-30 Effects of applied force on translational stiffness value at the holder-extension interface

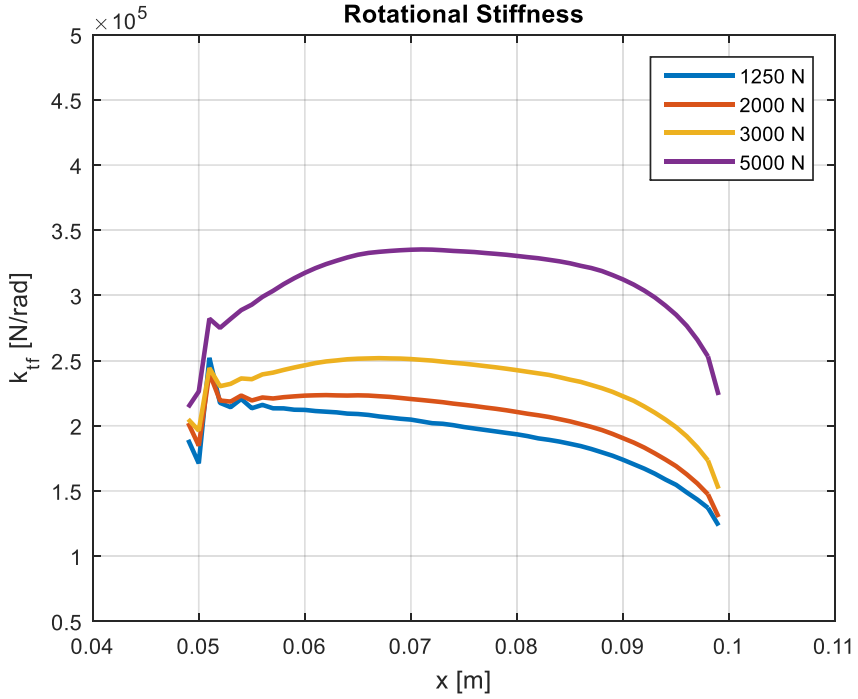

Figure 2-31 Effects of applied force on rotational stiffness value at the holder-extension interface

Then, different interference amounts is evaluated. 0.005 µm, 5 µm, 10 µm and 50 µm interference amounts are used. Unlike the linear analysis, for this case, when the interference amount is increased the stiffness values are increased slightly. And when using 0.005 µm the stiffness values towards the end of contact region decrease. Using too small interference values may cause a failure in creating contact and the nodes without contact deforms less than the other nodes. This affects slope of load-displacement curve and the stiffness values accordingly. Figure 2-32 shows the comparison of translational stiffness values. This results in, using nonlinear analysis, the effect of the interference amount can be observed but the sensitivity is small.

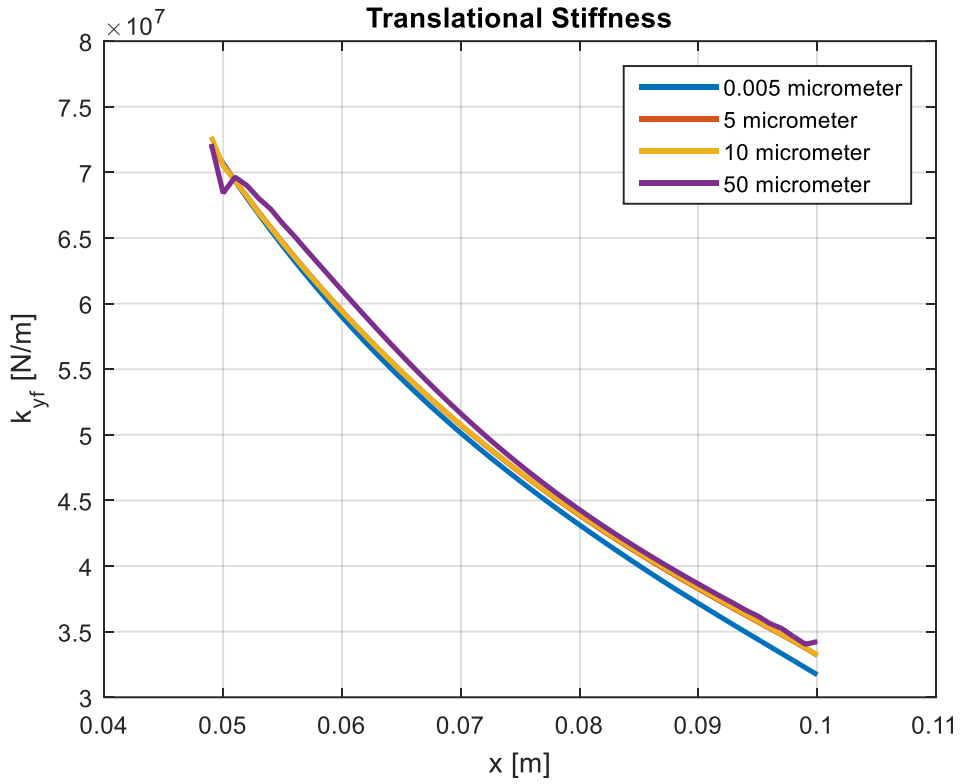

Figure 2-32 Effects of interference amounts on translational stiffness value at the holder-extension interface

Then, the effect of insertion length of the extension on the holder is examined. 52 mm, 45 mm and 40 mm insertion length in holder is used. As expected, the

distributed stiffness values remains the same within contact regions. The length of the extension outside the holder does not affect the stiffness values because the external load is applied just at the end of the contact region. Figure 2-33 shows the effect of the insertion length. Although the stiffness values remains same for the contact region, the equivalent stiffness values that are used to find tool tip FRF, the insertion length has significant effect on FRFs. Schmitz et al. [1] also examined the insertion length and they concluded that the part outside the holder does not affect the stiffness values, and the stiffness values of the contact region inside the holder are same.

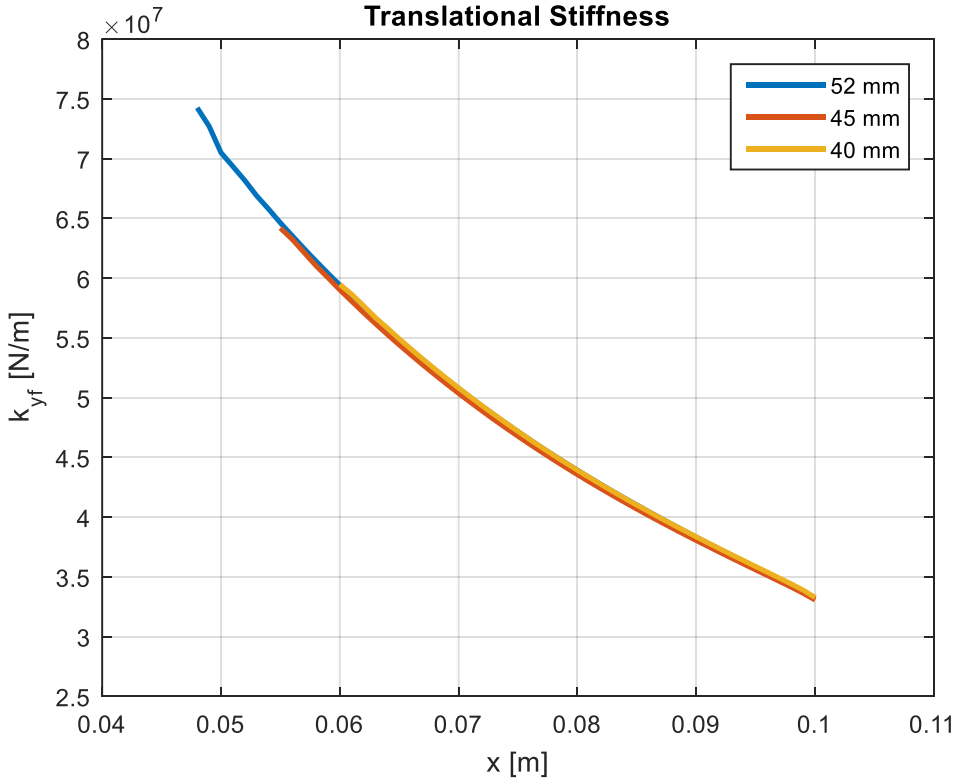

Figure 2-33 Effects of insertion length of the extension on translational stiffness value at the holder-extension interface

Then, the effect of element length is examined. At contact regions, smaller element size is used to examine the dynamic properties in detail. For this purpose, 1 mm and 1.5 mm element length is used. For other regions 2 mm element size is used. The stiffness values are the same for both results. It concludes that the element length is small enough to converge the results. Figure 2-34 shows the effect of the element length.

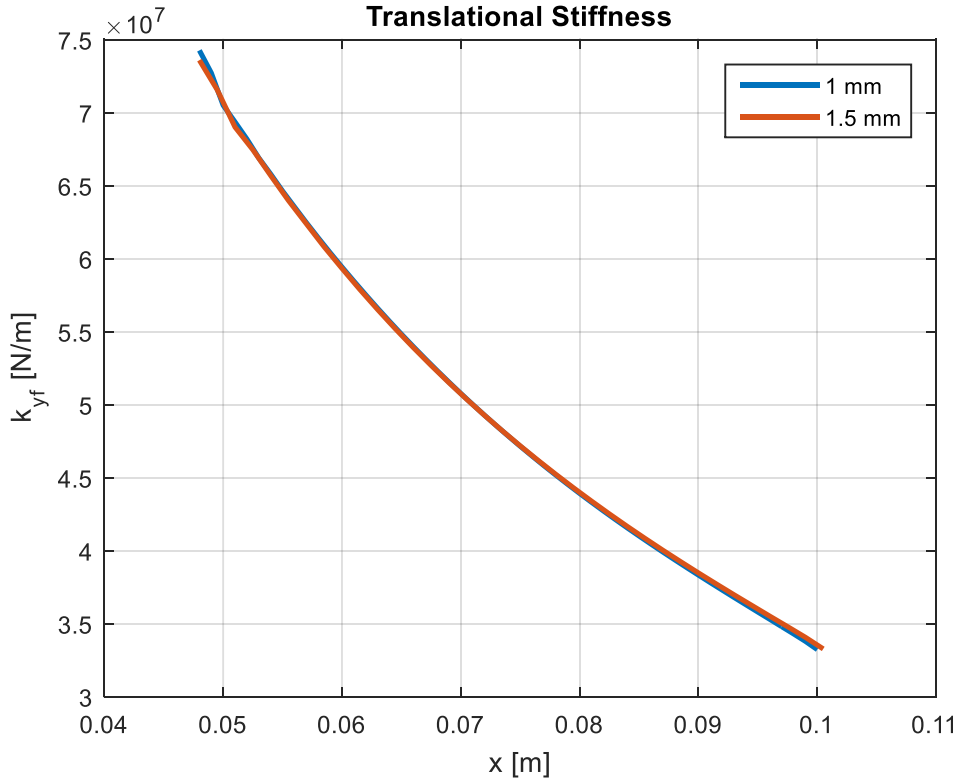

Figure 2-34 Effects of element length on translational stiffness value at the holder-extension interface

Lastly, the effect of the material of the tool is examined. The stiffness values are calculated for the tool made from carbide and the stiffness values are recalculated by changing the tool material to steel using nonlinear analysis. 9 μm interference applied

to the model. Like the linear analysis, stiffness values are not sensitive to material properties. Figure 2-35 shows the effects of material properties.

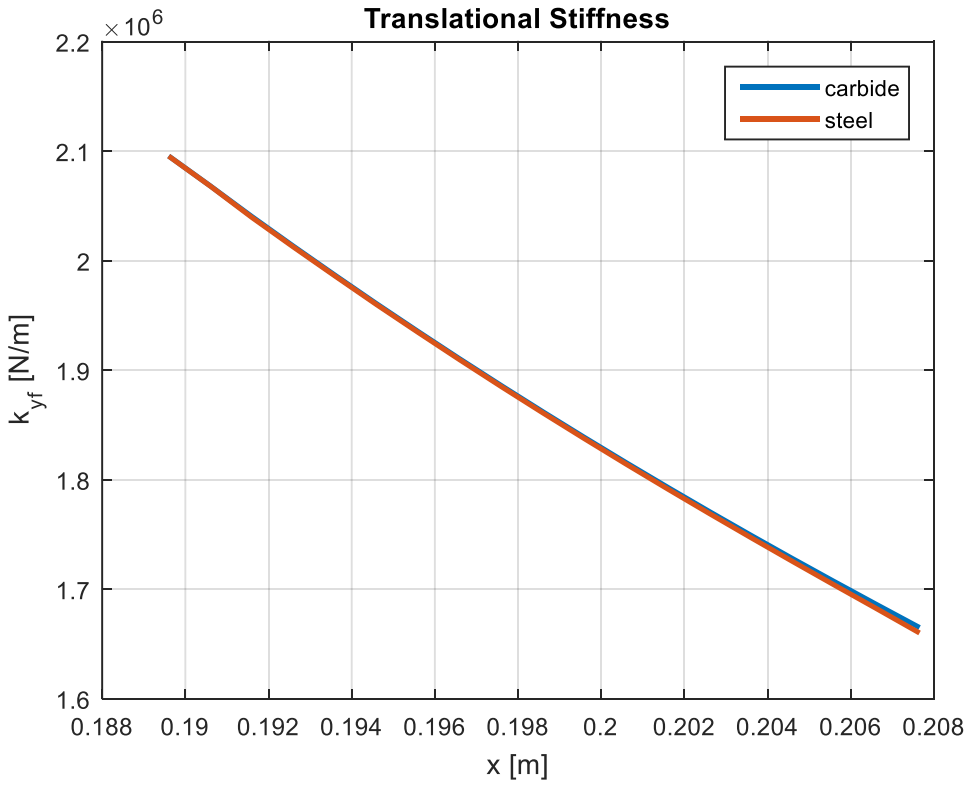

Figure 2-35 Effects of material properties on translational stiffness value at the extension-tool interface

2.5 Comparison of Linear and Nonlinear Analysis

When examining the effects of different combinations, nonlinear and linear analysis are both used. The effects are similar for both cases except interference amount. And Figure 2-36 and 2-37 show that stiffness values are also similar for both analysis types. (There is 5% error for stiffness values of the tool-extension contact region.) It can conclude that both linear and nonlinear analysis can be used to find stiffness values, because the results are close to each other.

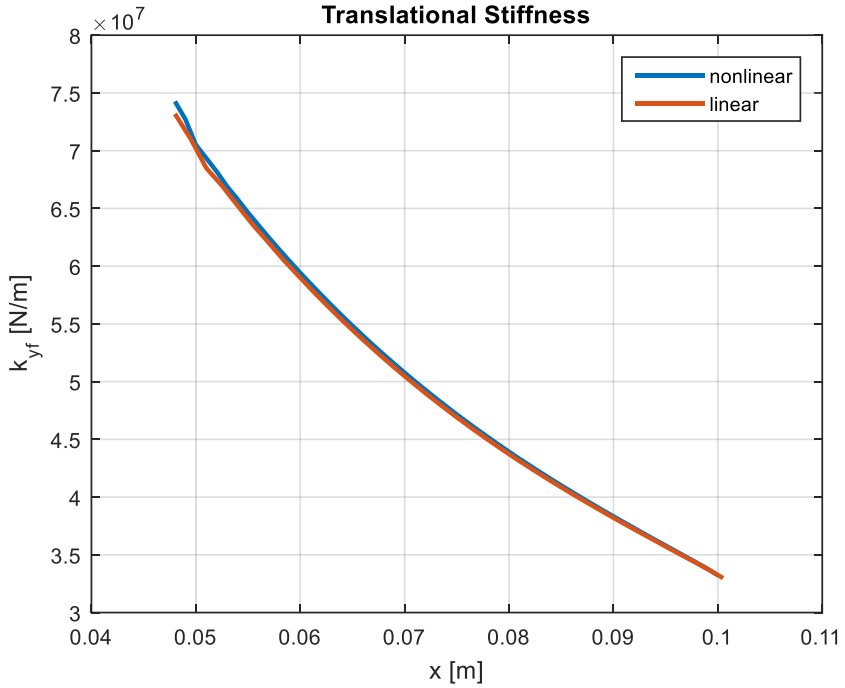

Figure 2-36 Comparison of linear and nonlinear analysis on translational stiffness value at the holder-extension interface

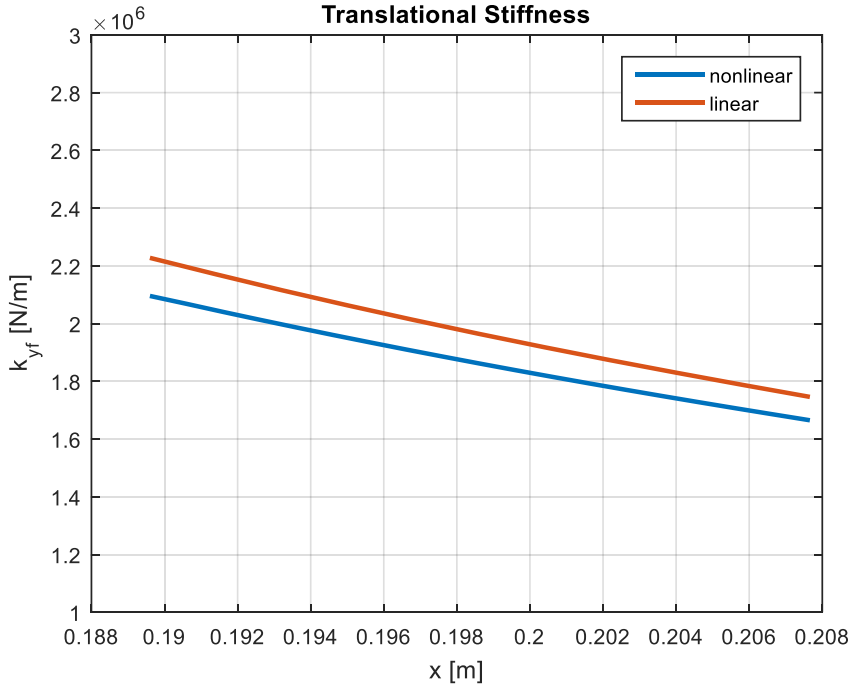

Figure 2-37 Comparison of linear and nonlinear analysis on translational stiffness value at the extension-tool interface

2.6 Calculating The Damping at the Interface

Energy dissipation for the interference fit caused by the friction between holder and extension and tool and extension along the x direction. The Coulomb damping is calculated using the friction force F_d for each element, x displacement values for each element along the tool axis. Damping values are summed for the nodes along the tool circumference. Equation 2.4 is used to calculate the damping values for each node.

$$c_{eq,n} = \frac{4 * F_{d,n}}{\pi * \omega * x_n} \tag{2.4}$$

Figure 2-38 and 2-39 shows the distributed viscous damping values for the holder-extension interface due to force and due to moment respectively. The same method is used to calculate distributed damping values for the extension-tool interface and Figure 2-40 and 2-41 shows the distributed viscous damping values due to force and due to moment respectively.

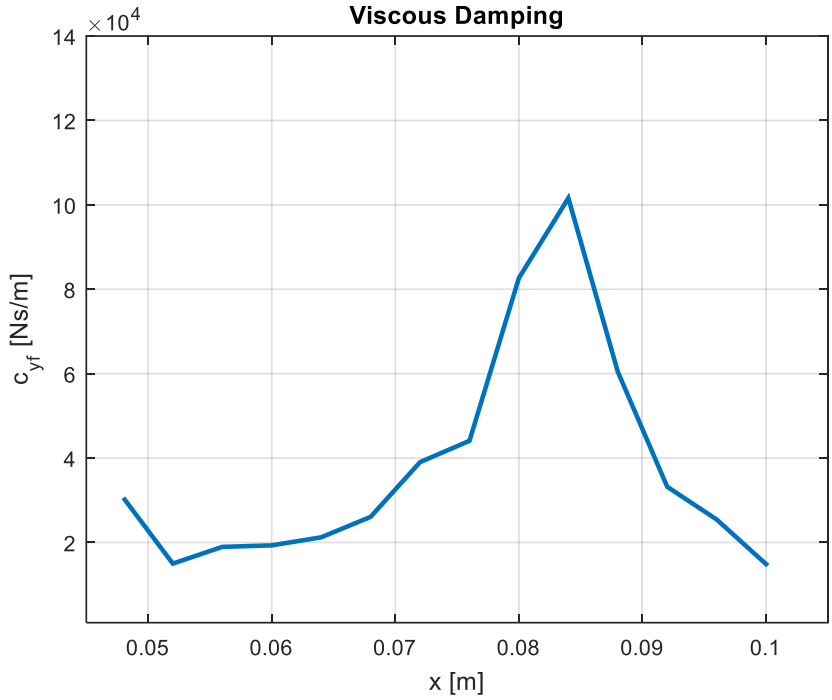

Figure 2-38 Distributed viscous damping values for holder-extension interface due to force

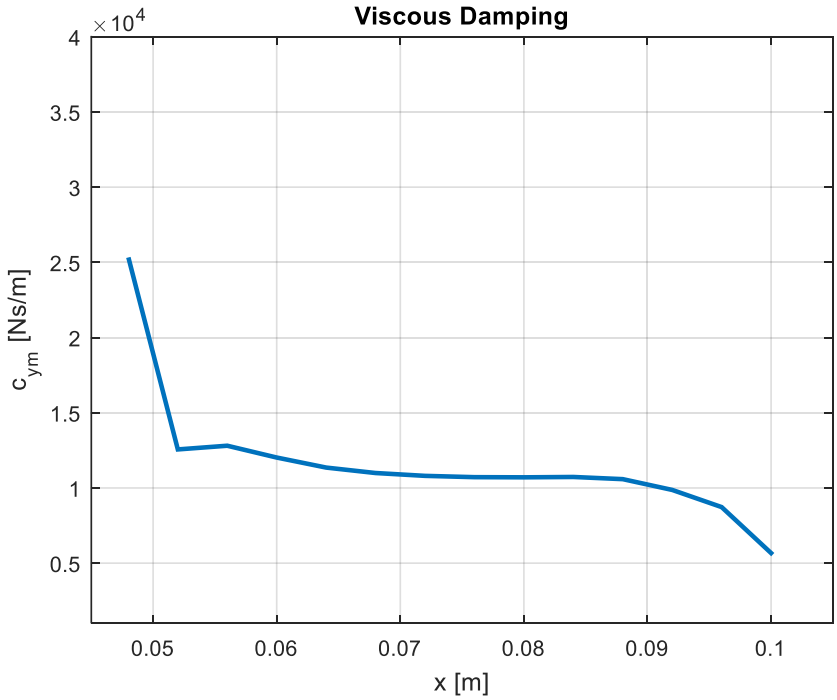

Figure 2-39 Distributed viscous damping values for holder-extension interface due to moment

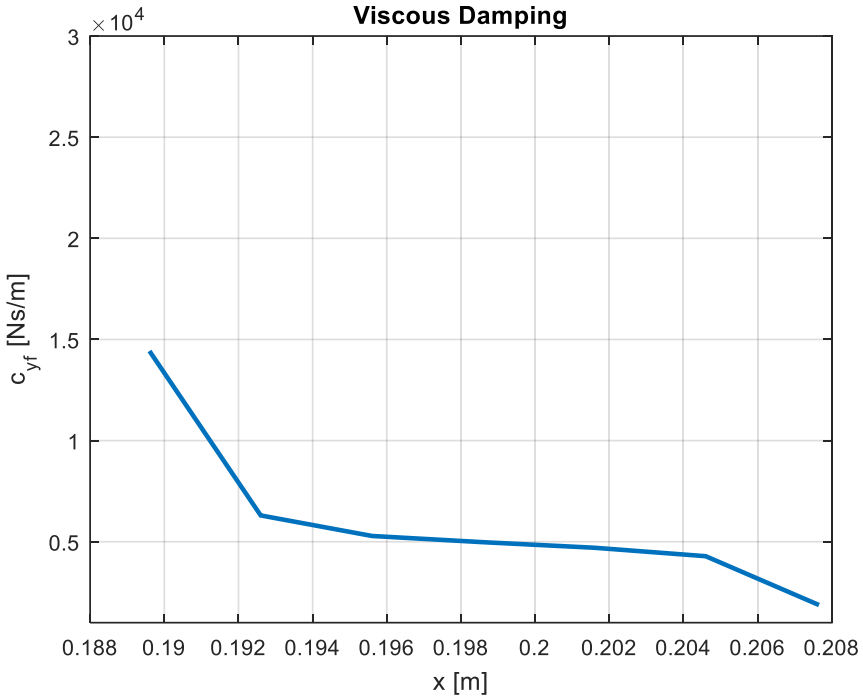

Figure 2-40 Distributed viscous damping values for extension-tool interface due to force

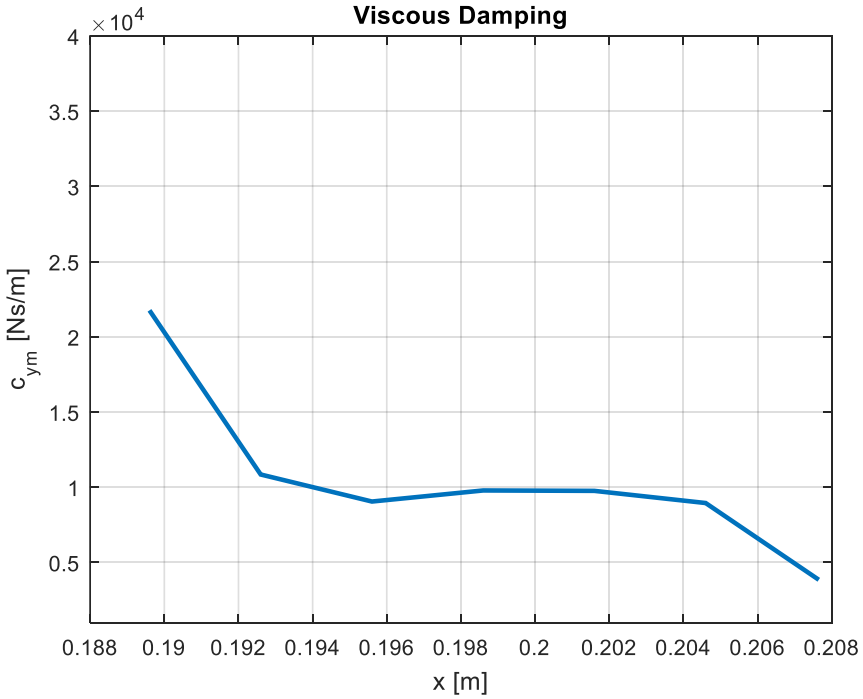

Figure 2-41 Distributed viscous damping values for extension-tool interface due to moment

In this chapter, dynamic properties are calculated using PATRAN and effects of contact parameters and machining conditions examined. However, it is not practical to use dozens of dynamic properties in RCSA method. Therefore, the proposed method of Schmitz et al. [1] is used. The contact between the parts are modeled as two spring-damper elements connected as series at two ends of the contact region as seen in Figure 2-42. The two stiffness values are summed up, because they are connected in series and for the damping, the average of the damping values along the contact region is used. The dynamic properties of the contact region of holder-extension interface and extension-tool interface are given in Table 2-5 and 2-6 respectively.

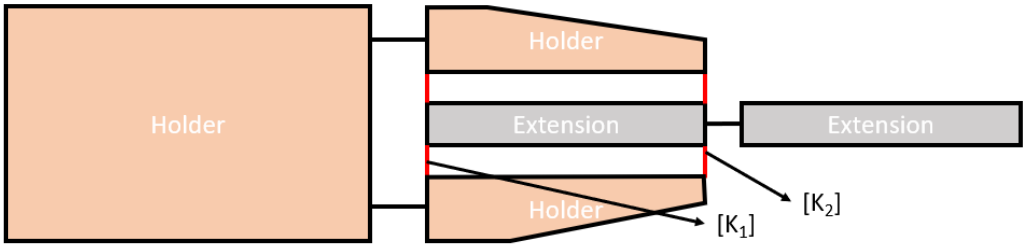

Figure 2-42 Modeling the contact at the holder-extension interface

Table 2-5 Dynamical contact properties at the holder-extension interface

k_{yf} [N/m]	$1.07*10^8$
k_{tf} [N/rad]	$4.38*10^5$
k_{ym} [Nm/m]	$1.25*10^7$
k_{tm} [Nm/rad]	$4.25*10^4$
c_{yf} [Ns/rad]	$3.80*10^4$
c_{ym} [Nms/rad]	$1.16*10^4$

Table 2-6 Dynamical contact properties at the extension-tool interface

k_{yf} [N/m]	$3.76*10^6$
k_{tf} [N/rad]	$4.96*10^5$
k_{ym} [Nm/m]	$1.14x10^6$
k_{tm} [Nm/rad]	$4.25*10^3$
c_{yf} [Ns/rad]	$6.00*10^3$
c_{ym} [Nms/rad]	$1.06*10^4$

CHAPTER 3

IDENTIFICATION OF CONTACT DYNAMICS USING INVERSE RECEPTANCE COUPLING

3.1 Inverse Receptance Coupling Substructure Analysis

To combine two substructures elastically, frequency response function coupling is used frequently. Coupling of two substructures, A and B with a flexible element is given in Figure 3.1

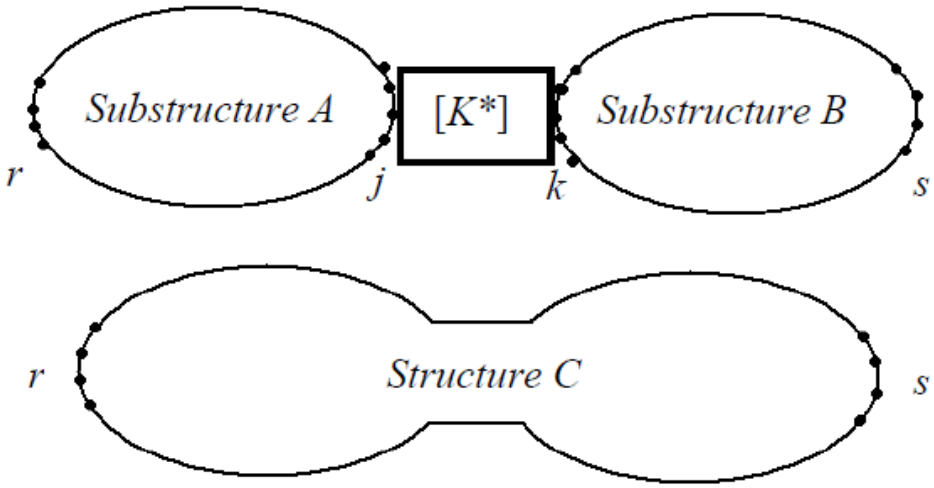

Figure 3-1 Coupling of two substructures with elastic element [39]

j and k are connection coordinates of substructure A and B respectively. r is coordinates of substructure A only and s is coordinates of substructure B only. FRF matrices of substructure A, B and coupled structure C is as follows:

$$[H_A(\omega)] = \begin{bmatrix} H_{rr}(\omega) & H_{rj}(\omega) \\ H_{jr}(\omega) & H_{jj}(\omega) \end{bmatrix} \tag{3.1}$$

$$[H_B(\omega)] = \begin{bmatrix} H_{kk}(\omega) & H_{ks}(\omega) \\ H_{sk}(\omega) & H_{ss}(\omega) \end{bmatrix} \tag{3.2}$$

$$[H_C(\omega)] = \begin{bmatrix} H_{rr}(\omega) & H_{rs}(\omega) \\ H_{sr}(\omega) & H_{ss}(\omega) \end{bmatrix} \tag{3.3}$$

For substructure A, displacement vectors can be written as following equations using force vectors.

$$\{x_A\} = \begin{Bmatrix} \{x_r\} \\ \{x_j\} \end{Bmatrix} = [H_A]\{f_A\} = [H_A] \begin{Bmatrix} \{f_r\} \\ \{f_j\} \end{Bmatrix} \tag{3.4}$$

$$\{x_r\} = [H_{rr}(\omega)]\{f_r\} + [H_{rj}(\omega)]\{f_j\} \tag{3.5}$$

$$\{x_j\} = [H_{jr}(\omega)]\{f_r\} + [H_{jj}(\omega)]\{f_j\} \tag{3.6}$$

For substructure B:

$$\{x_B\} = \begin{Bmatrix} \{x_k\} \\ \{x_s\} \end{Bmatrix} = [H_B]\{f_B\} = [H_B] \begin{Bmatrix} \{f_k\} \\ \{f_s\} \end{Bmatrix} \tag{3.7}$$

$$\{x_k\} = [H_{kk}(\omega)]\{f_k\} + [H_{ks}(\omega)]\{f_s\} \tag{3.8}$$

$$\{x_s\} = [H_{sk}(\omega)]\{f_k\} + [H_{ss}(\omega)]\{f_s\} \tag{3.9}$$

When no external moments or forces are action on joints, compatibilty of displacement and equilibrium of the forces equations at the connection DOFs can be written as:

$$\{f_j\} + \{f_k\} = 0 \tag{3.10}$$

$$\left\{\{x_j\} - \{x_k\}\right\}[K^*(\omega)] = \{f_k\} \tag{3.11}$$

Where $[K^*(\omega)]$ is the complex stiffness matrix that consists of the stiffness and damping elements.

Using equations (3.6) and (3.8) in equation (3.11) gives,

$$\left[H_{jr}(\omega)\right]\{f_r\} + \left[H_{jj}(\omega)\right]\{f_j\} - [H_{kk}(\omega)]\{f_k\} - [H_{ks}(\omega)]\{f_s\} = [K^*(\omega)]^{-1}\{f_k\} \tag{3.12}$$

Using equations (3.10) in equation (3.12) and after rearranging the equation, we get,

$$\{f_j\} = \left[\left[H_{jj}(\omega)\right] + [H_{kk}(\omega)] + [K^*(\omega)]^{-1}\right]^{-1}[H_{ks}(\omega)]\{f_s\} - \left[\left[H_{jj}(\omega)\right] + [H_{kk}(\omega)] + [K^*(\omega)]^{-1}\right]^{-1}\left[H_{jr}(\omega)\right]\{f_r\} \tag{3.13}$$

Then applying the equation (3.13) in equation (3.5) we can obtain,

$$\{x_r^C\} = \left[[H_{rr}(\omega)] - \left[H_{rj}(\omega)\right]\left[\left[H_{jj}(\omega)\right] + [H_{kk}(\omega)] + [K^*(\omega)]^{-1}\right]^{-1}\left[H_{jr}(\omega)\right]\right]\{f_r\} + \left[H_{rj}(\omega)\right]\left[\left[H_{jj}(\omega)\right] + [H_{kk}(\omega)] + [K^*(\omega)]^{-1}\right]^{-1}\left[H_{jr}(\omega)\right]\{f_s\} \tag{3.14}$$

Where $\{x_r^C\}$ is the displacement vector of the joint coordinates of the coupled structure C.

Using the equation (3.14), two of the receptance matrices of the assembly can be found as follows. (for simplification the frequency dependency is not included)

$$[H_{rr}^{C}] = [H_{rr}] - \left[H_{rj}\right]\left[\left[H_{jj}\right] + [H_{kk}] + [K^{*}]^{-1}\right]^{-1}\left[H_{jr}\right] \tag{3.15}$$

$$[H_{rs}^{C}] = \left[H_{rj}\right]\left[\left[H_{jj}\right] + [H_{kk}] + [K^{*}]^{-1}\right]^{-1}[H_{ks}] \tag{3.16}$$

In order to obtain the other two receptance matrices, equation (3.10) is used and we obtain,

$$\{f_k\} = -\left[\left[H_{jj}(\omega)\right] + [H_{kk}(\omega)] + [K^{*}(\omega)]^{-1}\right]^{-1}[H_{ks}(\omega)]\{f_s\} + \left[\left[H_{jj}(\omega)\right] + [H_{kk}(\omega)] + [K^{*}(\omega)]^{-1}\right]^{-1}\left[H_{jr}(\omega)\right]\{f_r\} \tag{3.17}$$

Then applying the equation (3.17) in equation (3.9) we can obtain,

$$\{x_s^{C}\} = [H_{sk}(\omega)]\left[\left[H_{jj}(\omega)\right] + [H_{kk}(\omega)] + [K^{*}(\omega)]^{-1}\right]^{-1}\left[H_{jr}(\omega)\right]\{f_r\} + \Big[[H_{ss}(\omega)] - [H_{sk}(\omega)]\left[\left[H_{jj}(\omega)\right] + [H_{kk}(\omega)] + [K^{*}(\omega)]^{-1}\right]^{-1}[H_{ks}(\omega)]\Big]\{f_s\} \tag{3.18}$$

Using the equation (3.18), the remaining two receptance matirces of the assembly can be found as follows. (for simplification the frequency dependency is not included)

$$[H_{sr}^{C}] = [H_{sk}]\left[\left[H_{jj}\right] + [H_{kk}] + [K^{*}]^{-1}\right]^{-1}\left[H_{jr}\right] \tag{3.19}$$

$$[H_{ss}^{C}] = [H_{ss}] - [H_{sk}]\left[[H_{jj}] + [H_{kk}] + [K^{*}]^{-1}\right]^{-1}[H_{ks}] \tag{3.20}$$

Rearranging the equations (3.15), (3.16), (3.19) and (3.20), we can obtain the complex stiffness matrix for every equation. It is given as follows:

$$[K^{*}] = \left[[H_{jr}][[H_{rr}] - [H_{rr}^{C}]]^{-1}[H_{rj}] - [H_{jj}] - [H_{kk}]\right]^{-1} \tag{3.21}$$

$$[K^{*}] = \left[[H_{ks}][H_{rs}^{C}]^{-1}[H_{rj}] - [H_{jj}] - [H_{kk}]\right]^{-1} \tag{3.22}$$

$$[K^{*}] = \left[[H_{jr}][H_{sr}^{C}]^{-1}[H_{sk}] - [H_{jj}] - [H_{kk}]\right]^{-1} \tag{3.23}$$

$$[K^{*}] = \left[[H_{ks}][[H_{ss}] - [H_{ss}^{C}]]^{-1}[H_{sk}] - [H_{jj}] - [H_{kk}]\right]^{-1} \tag{3.24}$$

Theoretically, to find joint properties any one of the four equations can be used. For every equation we must get same complex stiffness values. However, because of the identification of cross-coupling and rotational elements, as Tol et al [39] observed the performance of the four equations, the equation (3.21) gives the most accurate results. In addition, noise in the practical application affects the performance of the equations. For frequencies the system is very sensitive to noise, it is very difficult to use these equations to calculate dynamic properties. However, at the frequencies where joint properties are dominant, the equations gives more accurate results.

3.2 Identification of Contact Dynamics at the Holder-Extension and Extension-Tool Interface

3.2.1 Closed Form Approach in Identification of Contact Parameters

Components of the holder-extension-tool assembly and the stiffness matrices used in the RSCA are given in Figure 3-2. To achieve the tool point FRF of the assembly analytically, Timoshenko beam model proposed by Erturk et at [21] is used. Every part is considered individually and divided into segments, then receptance matrices are calculated and combined with rigid receptance coupling. After obtaining the receptance matrices, the holder and the extension is coupled with stiffness matrix K_{HE}. The tip point receptance matrix of the assembly can be obtained as follows:

$$[HE_{11}] = [E_{11}] - [E_{12}]\left[[E_{22}] + [H_{11}] + [K_{HE}]^{-1}\right]^{-1}[E_{21}] \tag{3.25}$$

Then, holder-extension assembly and the tool is coupled with complex stiffness matrix K_{ET}. The tip point receptance matrix of the assembly can be obtained as follows:

$$[HET_{11}] = [T_{11}] - [T_{12}]\left[[T_{22}] + [HE_{11}] + [K_{ET}]^{-1}\right]^{-1}[T_{21}] \tag{3.26}$$

The receptances given in Equation 3.25 and 3.26 are 2x2 matrices.

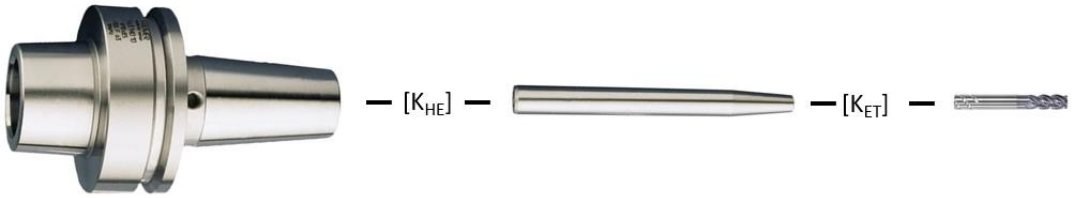

Figure 3-2 Holder-extension-tool assembly [41-43]

To eliminate the complication of modeling the contact at the interfaces, the part of the extension inside the holder is coupled with the holder rigidly and the hanging part is coupled with complex stiffness matrix K_{HE}. The same method is used for extension-tool interface (The part of the tool inside the extension is coupled with the extension rigidly and the remaining part is coupled with complex stiffness matrix K_{ET}). Therefore equation 3.25 and 3.26, H represents the holder and the extension part inside holder, and HE represents the holder, extension and the tool part inside the extension.

In order to calculate contact parameters, receptance coupling equations for holder-extension-tool assembly can be rearranged. For the holder-extension assembly complex stiffness matrix K_{HE} and for the extension-holder assembly complex stiffness matrix K_{ET} can be found as follows:

$$[K_{HE}] = \left[[E_{21}]\left[[E_{11}] - [HE_{11}]\right]^{-1}[E_{12}] - [E_{22}] - [H_{11}]\right]^{-1} \tag{3.27}$$

$$[K_{ET}] = \left[[T_{21}]\left[[T_{11}] - [HET_{11}]\right]^{-1}[T_{12}] - [T_{22}] - [HE_{11}]\right]^{-1} \tag{3.28}$$

The complex stiffness matrix proposed by Schmitz et al [1] can be used for Equations 3.27 and 3.28. The modified versions for the stiffness matrix is given below:

$$[K_{HE}] = \begin{bmatrix} k_{yf}^{HE} + i\omega c_{yf}^{HE} & k_{yM}^{HE} + i\omega c_{yM}^{HE} \\ k_{\theta f}^{HE} + i\omega c_{yf}^{HE} & k_{\theta M}^{HE} + i\omega c_{yM}^{HE} \end{bmatrix} \tag{3.29}$$

$$[K_{ET}] = \begin{bmatrix} k_{yf}^{ET} + i\omega c_{yf}^{ET} & k_{yM}^{ET} + i\omega c_{yM}^{ET} \\ k_{\theta f}^{ET} + i\omega c_{yf}^{ET} & k_{\theta M}^{ET} + i\omega c_{yM}^{ET} \end{bmatrix} \tag{3.30}$$

where k_{yf} is the diplacement to force stiffness, $k_{\theta f}$ is the rotation to force stiffness, k_{yM} is the diplacement to moment stiffness, $k_{\theta M}$ is the rotation to moment stiffness, c_{yf} is the diplacement to force damping, c_{yM} is the diplacement to moment damping, ω is the excitation frequency and i is the unit imaginary number.

3.2.2 Analytical Calculation Receptance Matrices

In order to calculate the tool point FRF of the holder-extension-tool assembly the Timoshenko model with free-free boundary conditions proposed by Ertürk et al [21] is used. The point and cross receptances of the tool are given as follows:

$$[T_{11}] = \begin{bmatrix} H_{11}^{T} & L_{11}^{T} \\ N_{11}^{T} & P_{11}^{T} \end{bmatrix} \tag{3.31}$$

$$[T_{12}] = \begin{bmatrix} H_{12}^{T} & L_{12}^{T} \\ N_{12}^{T} & P_{12}^{T} \end{bmatrix} \tag{3.32}$$

$$[T_{21}] = \begin{bmatrix} H_{21}^{T} & L_{21}^{T} \\ N_{21}^{T} & P_{21}^{T} \end{bmatrix} \tag{3.33}$$

$$[T_{22}] = \begin{bmatrix} H_{22}^{T} & L_{22}^{T} \\ N_{22}^{T} & P_{22}^{T} \end{bmatrix} \tag{3.34}$$

where;

$$H_{ij} = \frac{x_i}{F_j}\ , L_{ij} = \frac{\theta_i}{F_j}\ , N_{ij} = \frac{x_i}{M_j}\ , P_{ij} = \frac{\theta_i}{M_j} \tag{3.35}$$

In equation 3.35, x is the displacement, θ is the rotation, F is the transverse force and M is the bending moment. The following formulations can be used to calculate the relevant receptance components:

$$H_{ij} = \frac{-1}{\rho AL\omega^2} + \frac{-3}{\rho AL\omega^2} + \sum_{r=1}^{\infty} \frac{\phi_r(x_i)\phi_r(x_j)}{(1+i\gamma)\omega_r^2 - \omega^2} \tag{3.36}$$

$$L_{ij} = \frac{-6}{\rho AL\omega^2} + \sum_{r=1}^{\infty} \frac{\phi_r(x_i)\phi_r{}'(x_j)}{(1+i\gamma)\omega_r^2 - \omega^2} \tag{3.37}$$

$$N_{ij} = \frac{-6}{\rho AL\omega^2} + \sum_{r=1}^{\infty} \frac{\phi_r{}'(x_i)\phi_r(x_j)}{(1+i\gamma)\omega_r^2 - \omega^2} \tag{3.38}$$

$$P_{ij} = \frac{-12}{\rho AL\omega^2} + \sum_{r=1}^{\infty} \frac{\phi_r{}'(x_i)\phi_r{}'(x_j)}{(1+i\gamma)\omega_r^2 - \omega^2} \tag{3.39}$$

where ρ is the density, A is the cross-sectional area, γ is the loss factor, ω_r is the r-th natural frequency, $\phi_r(x)$ is the r-th mode shape and $\phi_r{}'(x)$ is the derivative of the r-th mode shape.

3.2.3 RDOF Estimation

In order to use IRCSA method, besides the translational DOFs, the rotational DOFs should also be obtained. However, as Duarte and Ewins [45] stated measuring the rotational DOFs requires special equipment, such as angular transducers and lasers,

and techniques, such as block, the estimation and finite difference. Special equipment are not easily accessible because of their excessive cost. Among the special techniques the finite difference method provides an effective and simple solution for obtaining RDOFs. This finite difference method requires two or three accelerometers placed with constant spacing (s) as shown in Figure 3.3.

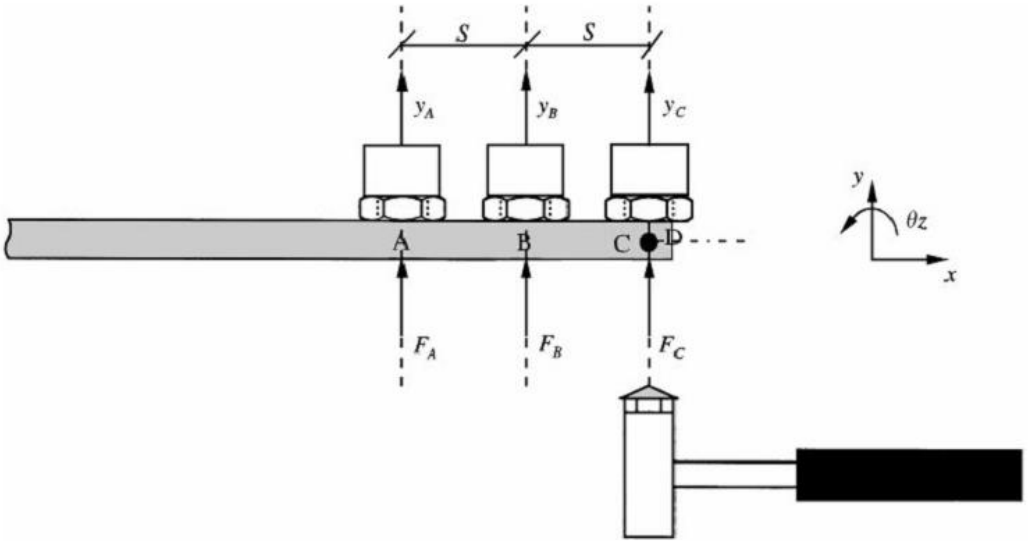

Figure 3-3 Calculating rotational degrees of with finite-difference technique [45]

The second order central approximation is used to find RDOFs. To use this formulation three measurement points are utilized. And the formulation for the second order-central transformation matrix is given as follows:

$$[T_{2c}] = \frac{1}{2s}\begin{bmatrix} 0 & 2s & 0 \\ -1 & 0 & 1 \end{bmatrix} \tag{3.40}$$

And the rotational FRF can be obtained as follows:

$$[H_{est}] = \begin{bmatrix} H_{yy} & H_{y\theta} \\ H_{\theta y} & H_{\theta\theta} \end{bmatrix} = [T_{2c}][H_{meas}][T_{2c}]^T \tag{3.41}$$

Where $[H_{meas}]$ is obtained with the measured FRFs at the points A, B and C. And it is defined as:

$$[H_{meas}] = \begin{bmatrix} H_{AA} & H_{AB} & H_{AC} \\ H_{BA} & H_{BB} & H_{BC} \\ H_{CA} & H_{CB} & H_{CC} \end{bmatrix} \tag{3.42}$$

3.3 Analytical Case Study

3.3.1 Receptance Coupling of Holder-Extension Assembly

In this section receptance coupling of holder-extension assembly is given. In order to use RCSA method, receptance matrices of the holder and the extension is calculated using Equations 3.36 to 3.39. After calculating the receptance matrices contact parameters found in Section 3 is used. The stiffness and damping values for the holder-extension interface is given in Table 2.5.

The tip point FRF of the holder-extension assembly is obtained using the RCSA method and the first element of the receptance matrix is given in Figure 3.4. The tip point FRF is also obtained by experiment and using PATRAN. Comparison of three methods is given in Figure 3.5. Analytically obtained FRF is quite different from the other two graphs. The formulations used to calculate receptances and the method of using dynamic properties at the contact region may result in this difference.

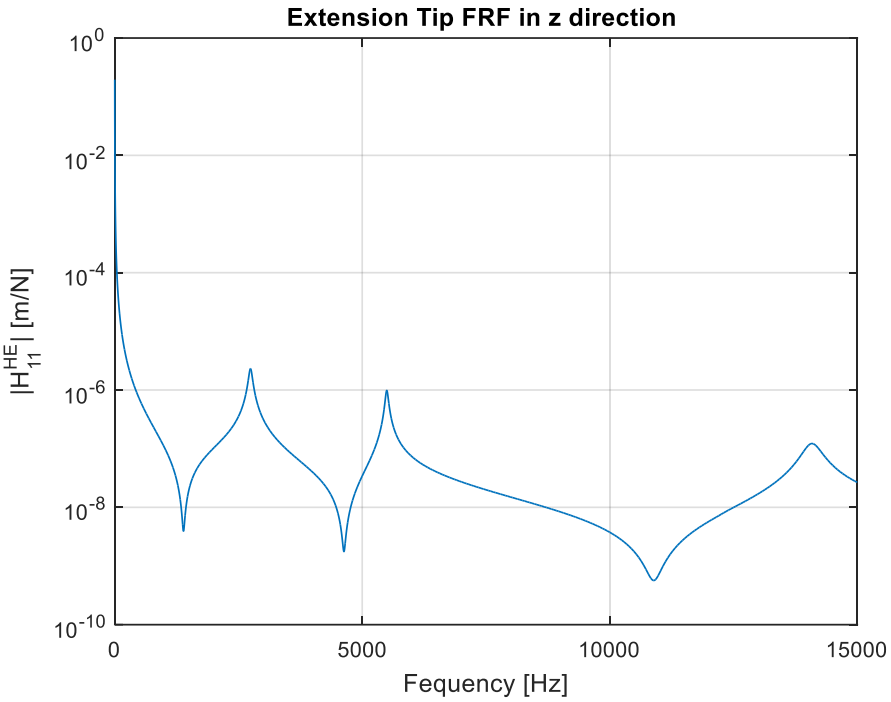

Figure 3-4 Analytically obtained extension tip FRF

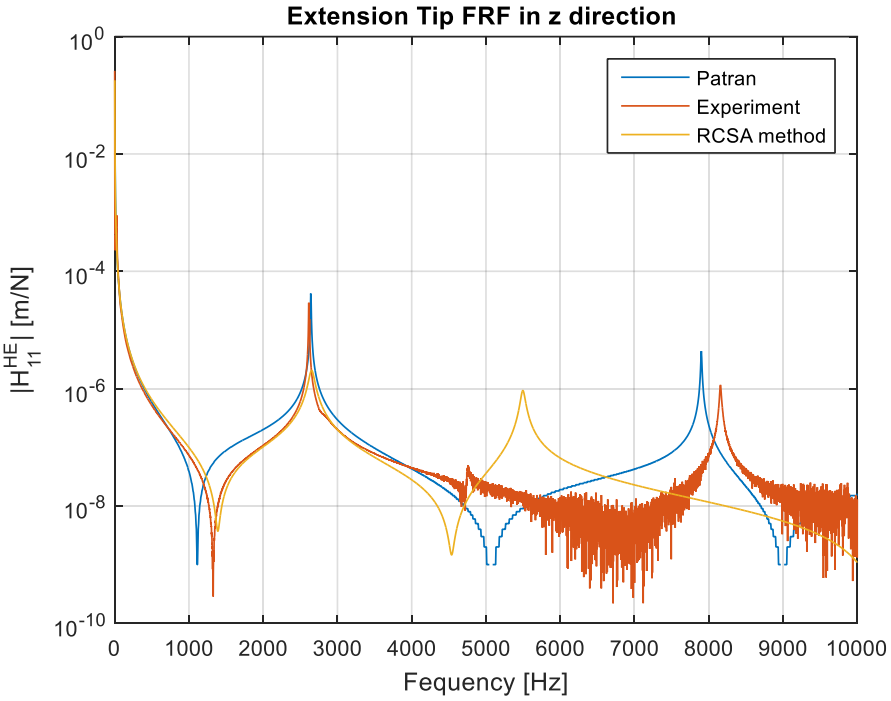

Figure 3-5 Comparison of extension tip point FRF

3.3.2 Inverse Receptance Coupling of Holder-Extension Assembly

The receptance of the assembly is calculated successfully. Therefore using IRCSA method, the dynamical contact parameters can also be obtained via inverse function in MATLAB. As seen in Figure 3-6 and 3-7, dynamical contact properties can be calculated exactly same as the values used in RCSA method.

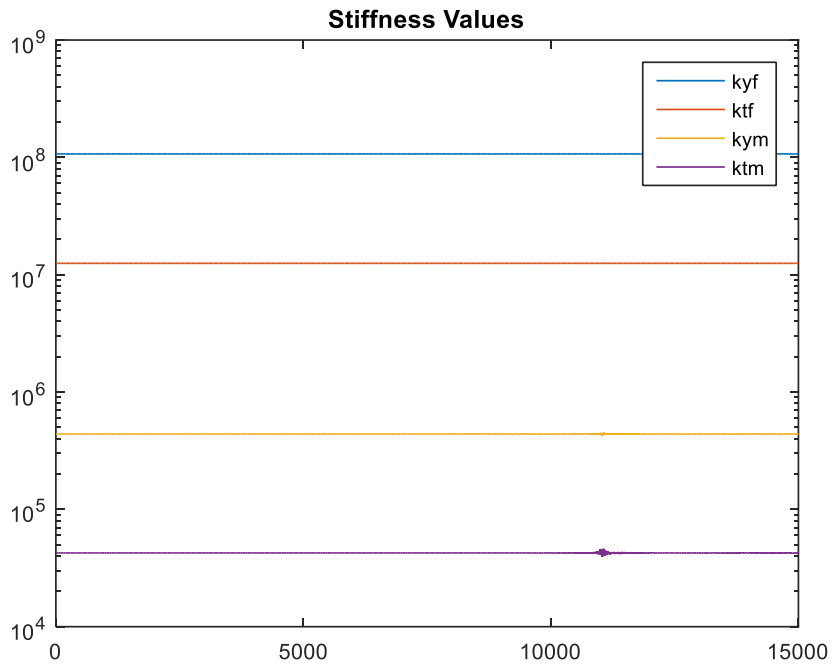

Figure 3-6 Analytically obtained stiffness values at the holder-extension contact interface

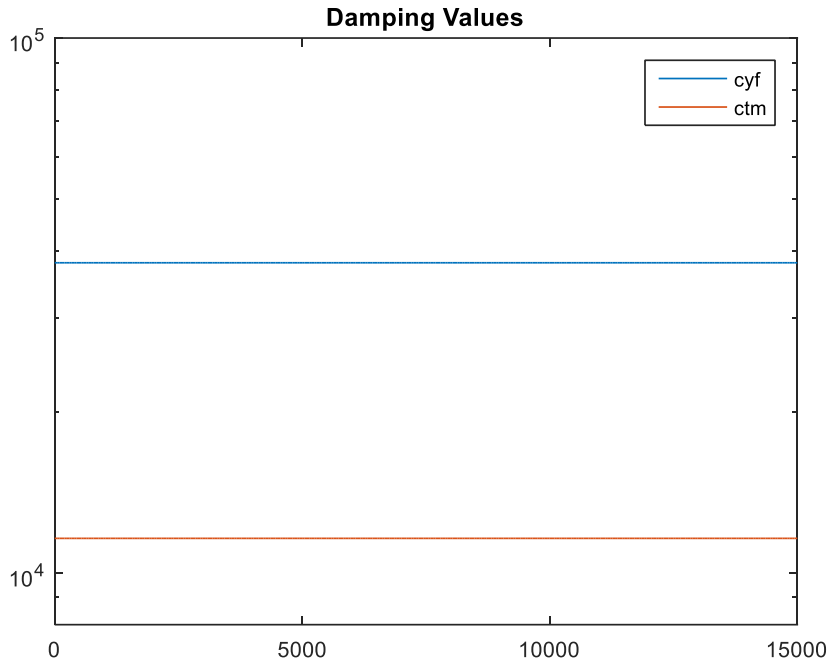

Figure 3-7 Analytically obtained damping values at the holder-extension contact interface

The dynamic properties at the contact region can be found using analytically obtained receptances for the assembly, but this approach is not realistic. In order to simulate the experimental results, random noise should be added to the receptance matrices. Using normrnd function in MATLAB, a random number of arrays with standart deviation 5% is multiplied with the extension tip point FRF. The new FRF with noise is given in figure 3-8.

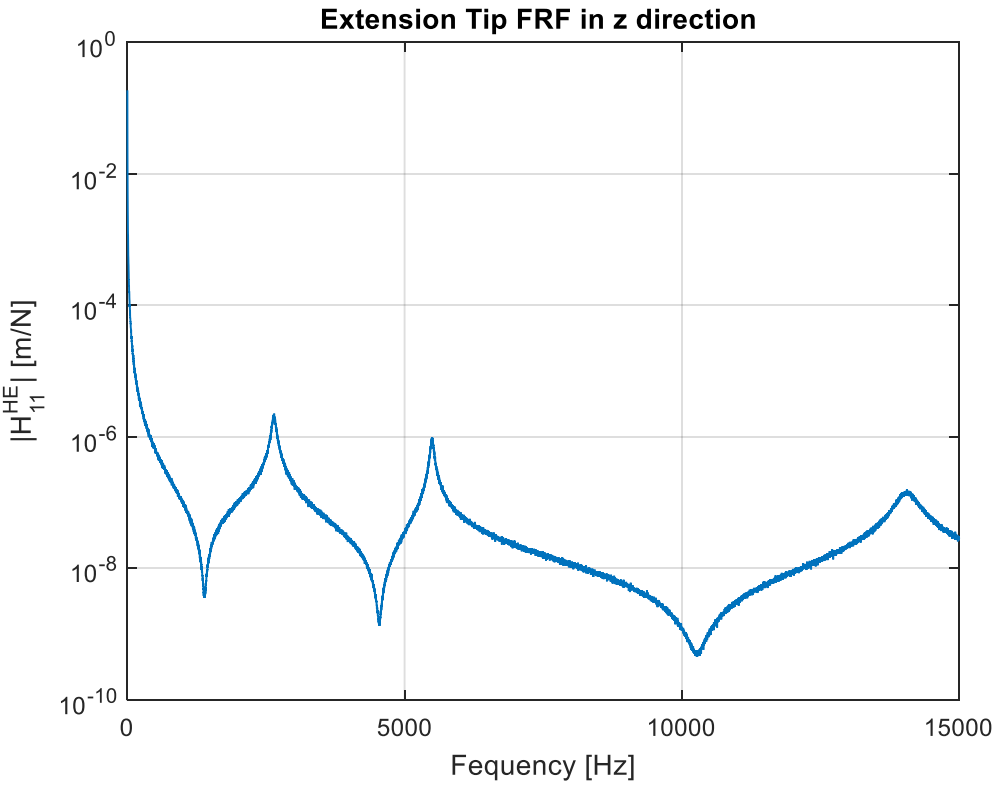

Figure 3-8 Analytically obtained extension tip point FRF with noise

With new tip point FRF with noise, the dynamic properties at the holder-extension interface is calculated again using inv function in MATLAB. However, dynamic properties are very sensitive to noise. The displacement to force stiffness and displacement to force damping values are given in Figure 3-9 and 3-10 respectively. The similar results are obained for the remained dynamic parameters. Although, there is a significant noise in the calculated values, near the natural frequency of the assembly the dynamic parameters less sensitive. Therefore, considering frequency region near the natural frequency of the assembly gives reasonable results. The natural frequency of the assembly is around 2640 Hz. Average stiffness values between 2600-2700 Hz is 9.2e7 N/m and average damping values between 2000-2050 Hz is 2.7e4 Ns/m.

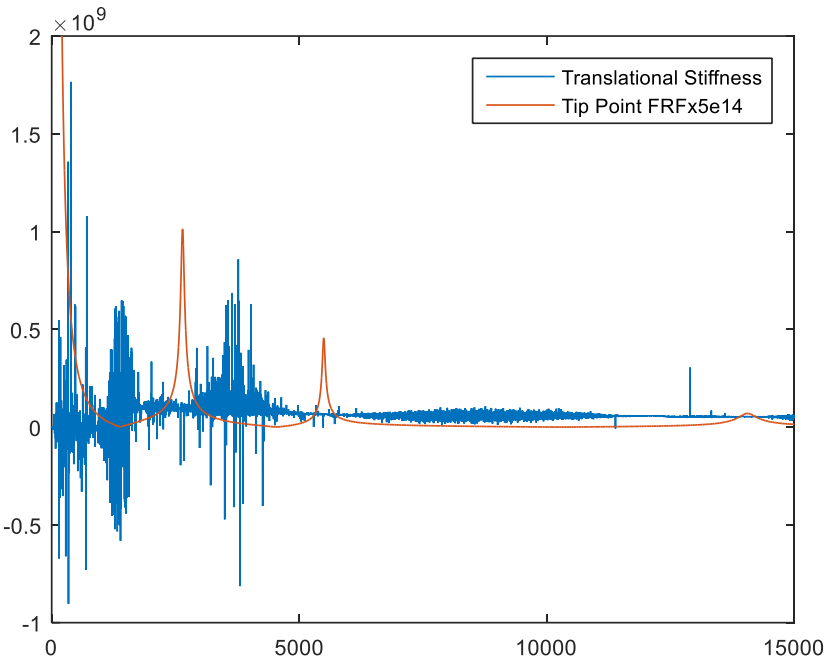

(a)

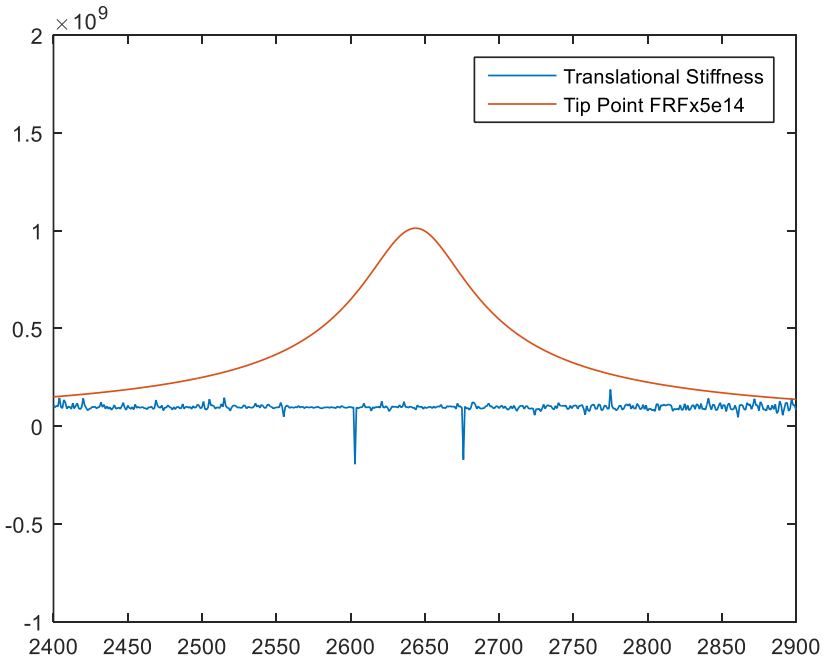

(b)

Figure 3-9 (a) Calculated displacement to force stiffness values for the holder-extension interface, (b) Calculated displacement to force stiffness values for the holder-extension interface focused around the natural frequency of the assembly

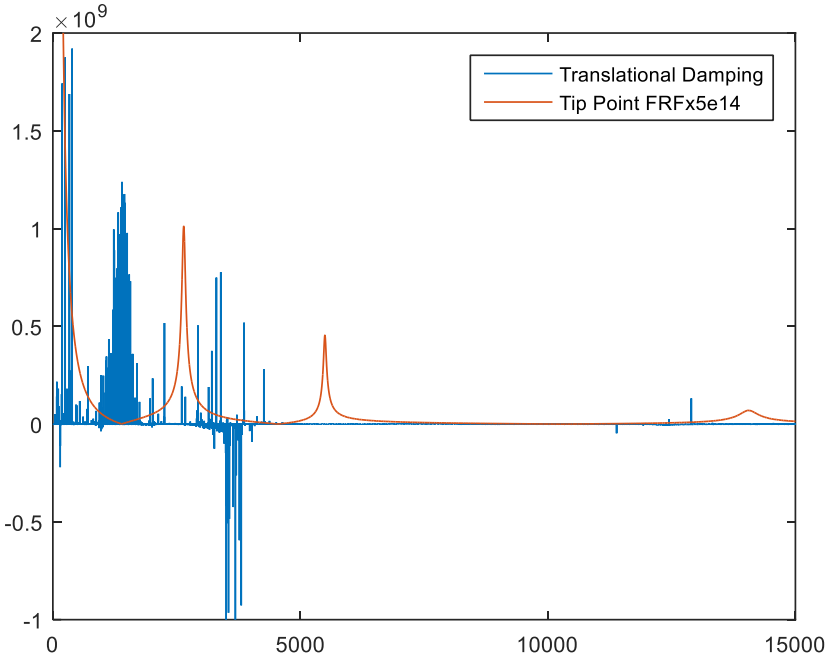

(a)

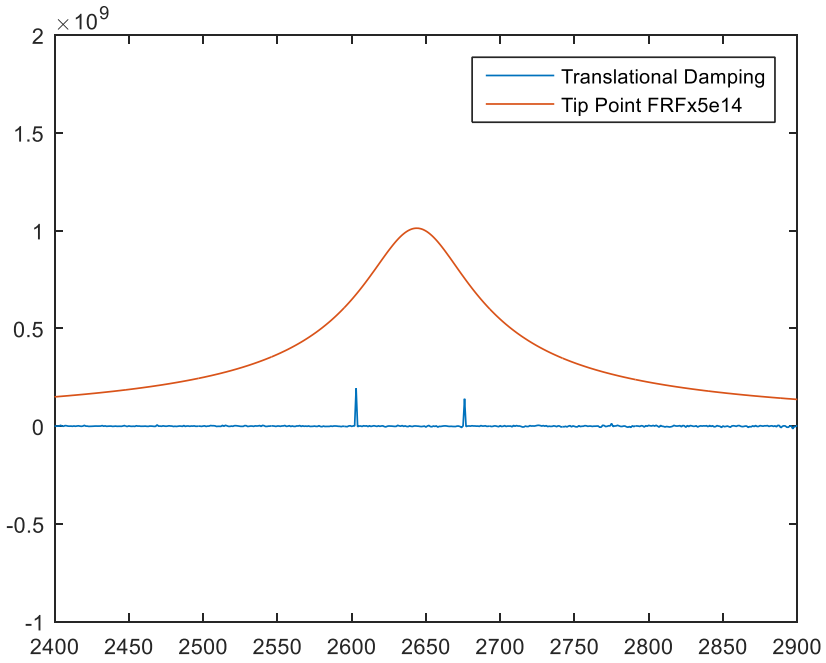

(b)

Figure 3-10 Calculated displacement to force damping values for the holder-extension interface, (b) Calculated displacement to force damping values for the holder-extension interface focused around the natural frequency of the assembly

Ozsahin et al. [20], also used the IRCSA method to find contact dynamics parameters at the holder-tool assembly. When they used direct inverse for matrix inversion, they got similar results.

The dynamical parameters are very sensitive to the noise, because the matrix inversion is used in the calculations. The built in inv function in MATLAB is used to calculate the inverse of the matrices. In the next section different matrix inversion method are used to obtain more accurate results.

3.3.3 Alternative Matrix Inversion Methods

3.3.3.1 Moore-Penrose Pseudoinverse

The most common alternative matrix inversion method is Moore-Penrose pseudoinverse. This method is based on Singular Value Decomposition. A brief explanation of the method is as follows:

A linear system can be defined as:

$$Ax = b \tag{3.43}$$

In order to calculate inversion of matrix A, the SVD of the matrix can be calculated as:

$$A = U\Sigma V^T \tag{3.44}$$

Inserting Equation 2.44 to 2.43, we get:

$$U\Sigma V^T x = b \tag{3.45}$$

To eliminate the coefficients of the x matrix, both side of the equation should be multiplied by $V\Sigma^{-1}U^T$

$$V\Sigma^{-1}U^T U\Sigma V^T x = V\Sigma^{-1}U^T b \tag{3.46}$$

$$x = V\Sigma^{-1}U^T b \tag{3.47}$$

Therefore pseudoinverse of the A matrix can be found as:

$$A^{\dagger} = V\Sigma^{-1}U^T \tag{3.48}$$

The Moore-Penrose pseudoinverse can be calculated easily in MATLAB with built in pinv function. The comparison of displacement to force stiffness and damping values for holder-extension interface obtained with direct inverse and Moore-Penrose pseudoinverse is given in Figure 3-11 and 3-12 respectively. It can be seen that, the Moore-Penrose pseudoinverse gives exactly same result as direct inverse method.

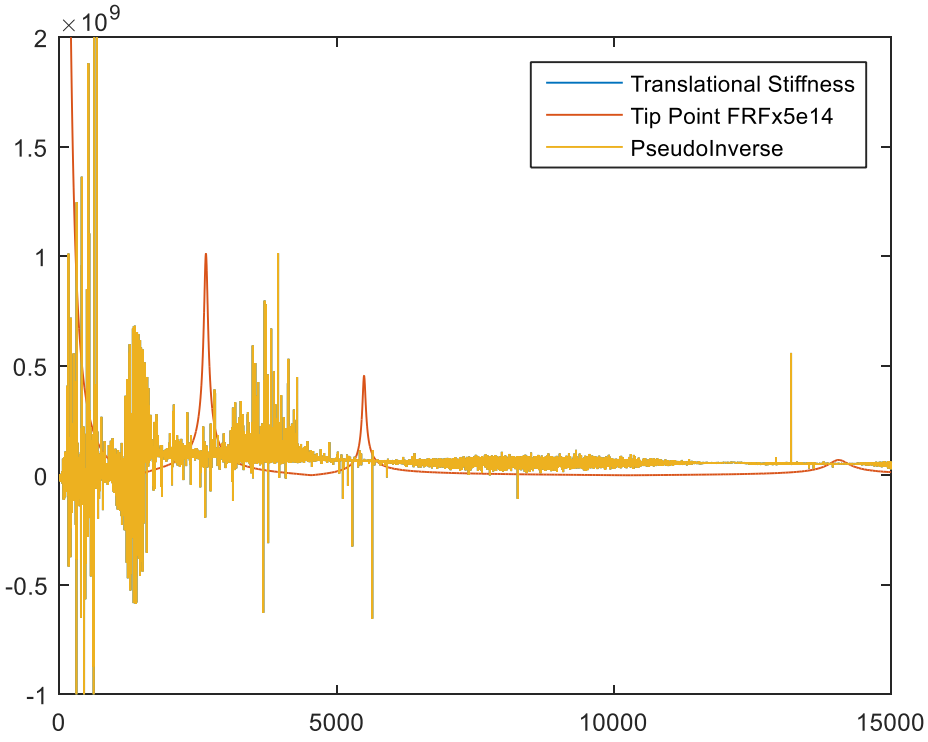

Figure 3-11 Comparison of direct inverse and Moore-Penrose pseudoinverse method for translational stiffness values for holder-extension interface

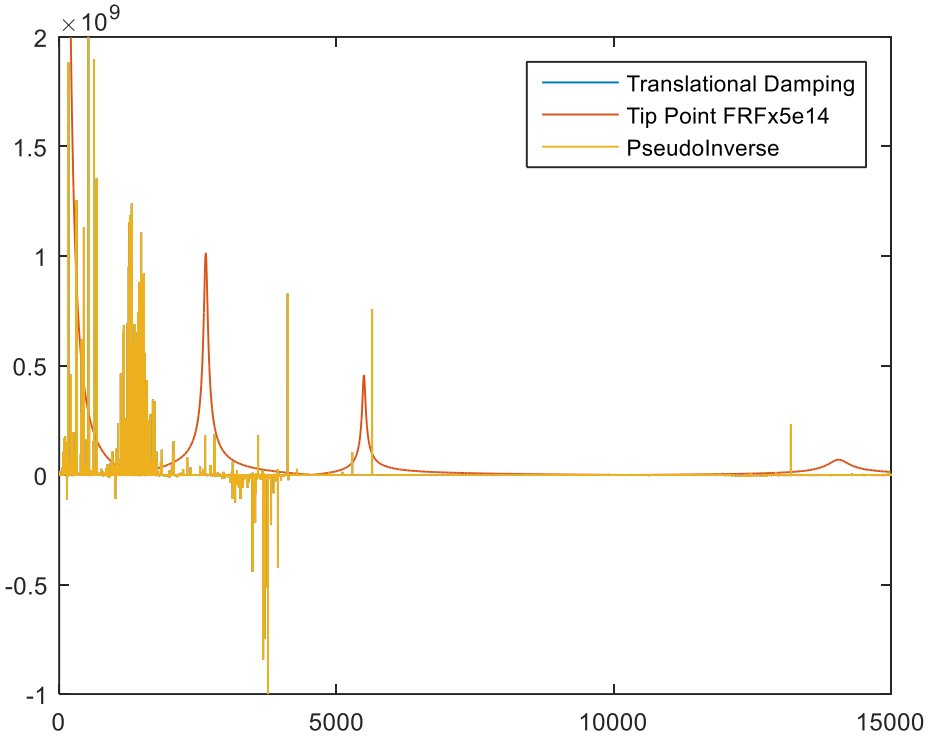

Figure 3-12 Comparison of direct inverse and Moore-Penrose pseudoinverse method for translational damping values for holder-extension interface

3.3.3.2 Wu's Inversion Method

Wu [40] proposed a matrix inversion method for severely ill-conditional matrices. The method is aimed to reduce the condition number of the matrix. The condition number of a matrix can be found as:

$$\kappa(A) = \frac{\sigma_n}{\sigma_1} \tag{3.49}$$

where σ_i's are the singular values of the A matrix. Therefore if $\sigma_n \gg \sigma_1$, the matrix is defined as ill-conditioned.

Diagonal perturbation of the matrix A and its excursion can be written as;

$$(A + \mu I)x = b + \Delta b \tag{3.50}$$

Where μ is the perturbation parameter and Δb is the excursion on b due to perturbation to the matrix A. Δb is equal to μx, therefore Equation (3.50) can be written as:

$$(A + \mu I)x = b + \mu x \tag{3.51}$$

Since $A + \mu I$ is invertible, we obtain,

$$(I - \mu(A + \mu I)^{-1})x = (A + \mu I)^{-1}b \tag{3.52}$$

Leaving the x alone on the left side of the equation, we obtain:

$$x = (I - \mu(A + \mu I)^{-1})^{-1}(A + \mu I)^{-1}b \tag{3.53}$$

Therefore Wu's method for inversion of a matrix is as follows:

$$A^{-1} = (I - \mu(A + \mu I)^{-1})^{-1}(A + \mu I)^{-1} \tag{3.54}$$

Where

$$\mu = M\lambda_{max}(A) \tag{3.55}$$

Where $\lambda_{max}(A)$ is the maximum eigenvalue of the A matrix. And 0<M<1. The value of M should be selected so that the matrix $I - \mu(A + \mu I)^{-1}$ must be a well-conditioned matrix. The comparison of displacement to force stiffness and damping values for holder-extension interface obtained with direct inverse and Wu's method is given in Figure 3-13 and 3-14 respectively. It can be seen that, Wu's method gives more stable results around the natural frequency of the assembly.

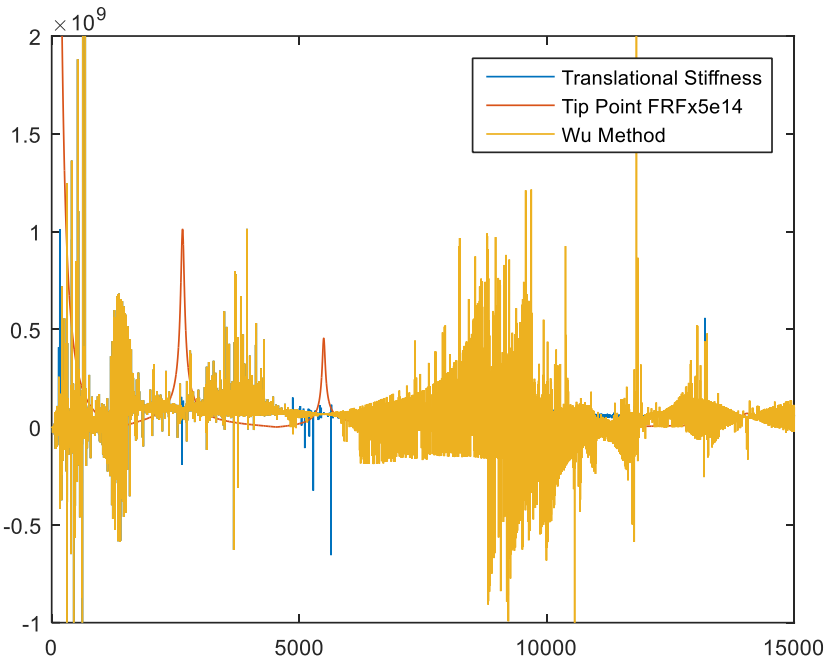

(a)

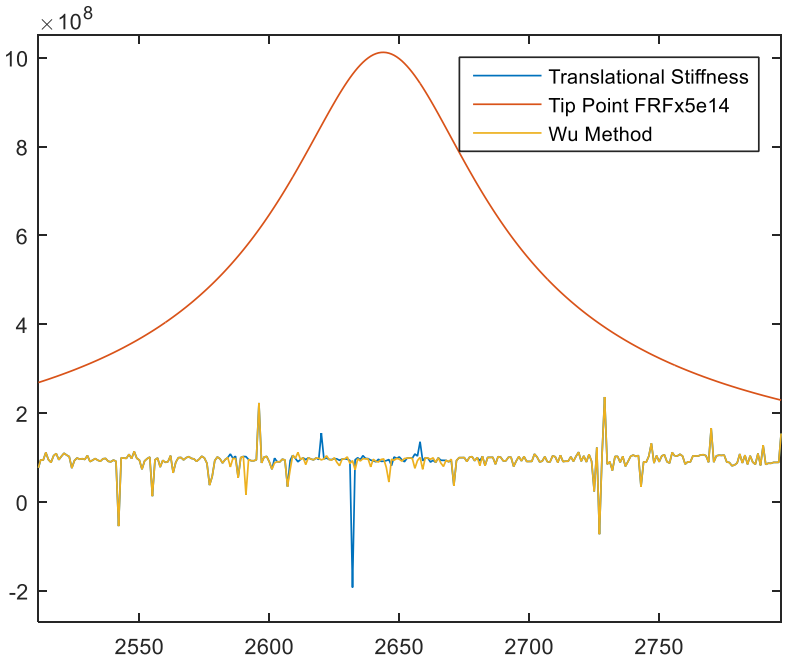

(b)

Figure 3-13 (a) Comparison of direct inverse and Wu's method for translational stiffness values for holder-extension interface (b) Comparison of direct inverse and Wu's method for translational stiffness values for holder-extension interface focused around the natural frequency of the assembly

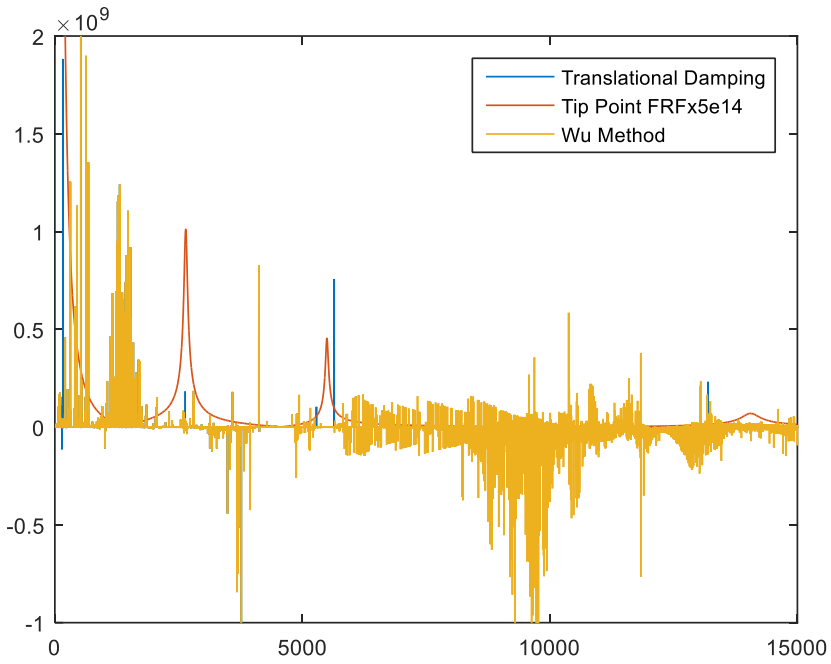

(a)

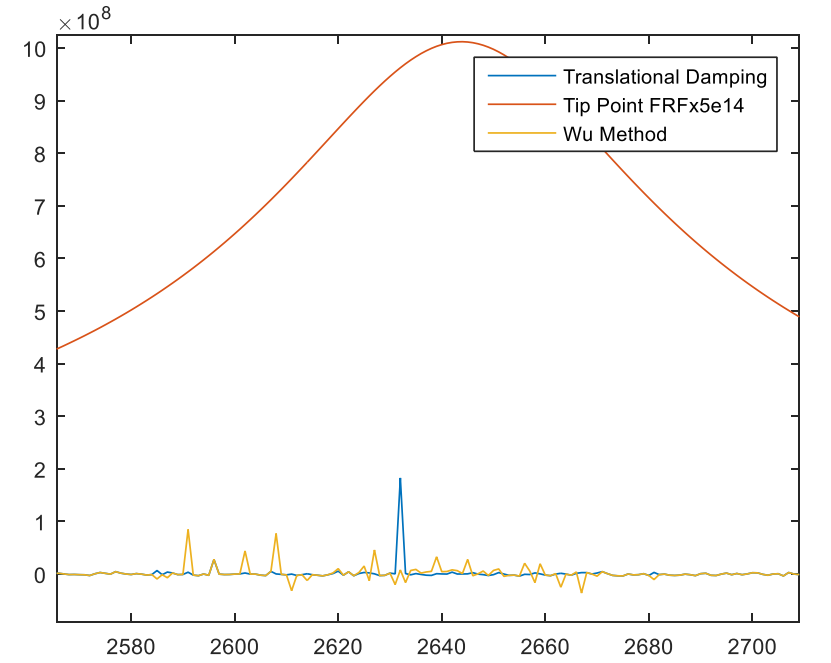

(b)

Figure 3-14 (a) Comparison of direct inverse and Wu's method for translational damping values for holder-extension interface (b) Comparison of direct inverse and Wu's method for translational damping values for holder-extension interface focused around the natural frequency of the assembly

3.3.3.3 Using Filter

To eliminate the effect of the noise, using filter is a common approach. For this purpose the built in filter function in MATLAB is used with window length 100. This means that the function calculates the avarage of the every 100 value. Filtering the result with the noise gives the most stable results for the translational stiffness and damping values. The comparison of the result obtained direct inverse method and result with filtered data is given in figures 3-15 and 3-16.

In this chapter, the closed form expression of the RCSA method is given and the dynamic properties obtained from PATRAN is used to calculate tip point FRFs. Then, using the receptances obtained analytically and receptances with noise to simulate experimental results, IRCSA method is used to determine dynamic properties of the contact region. Because the dynamic properties are sensitive to noise, four different inversion method is used to calculate dynamic properties at the holder-extension contact region. Although, the Wu's method and filtering the data gives more stable results, the error in the obtained dynamic properties are much higher than the direct inverse method. The comparison of the four method is given in Table 3.1.

Table 3-1 Comparison of inversion methods

	k_{yf} [N/m]	% error	c_{yf} [Ns/m]	% error
Direct Inverse	$9.44*10^7$	12	$5.74*10^4$	51
Pseudoinverse	$9.44*10^7$	12	$5.74*10^4$	51
Wu's Method	$9.16*10^7$	14	$3.46*10^6$	9005
Filter	$8.89*10^7$	17	$5.87*10^4$	54

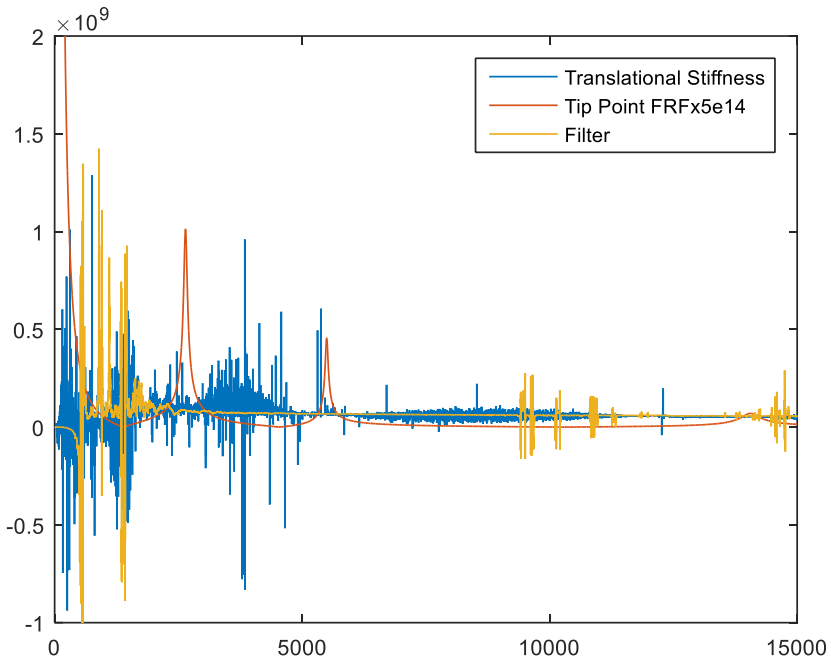

(a)

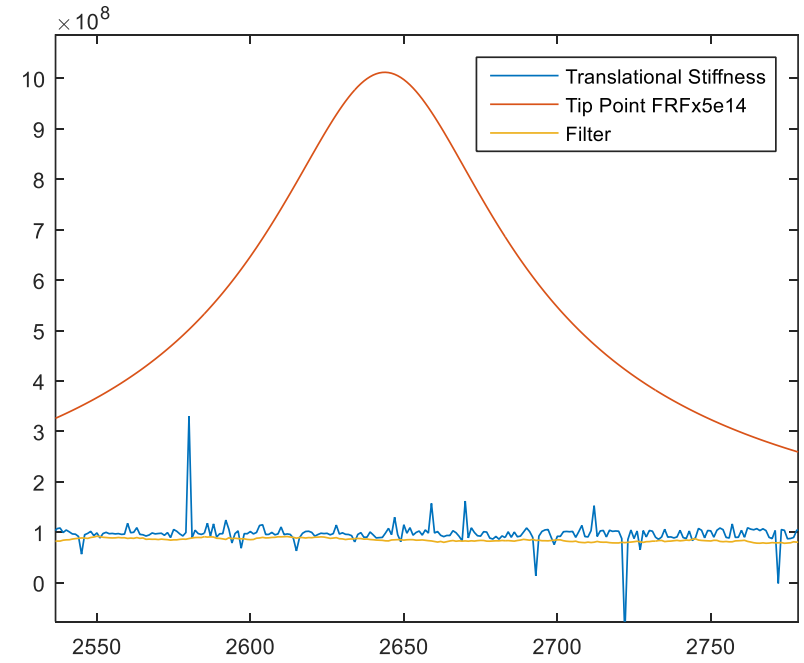

(b)

Figure 3-15 (a) Comparison of direct inverse and filtering method for translational stiffness values for holder-extension interface (b) Comparison of direct inverse and filtering method for translational stiffness values for holder-extension interface focused around the natural frequency of the assembly

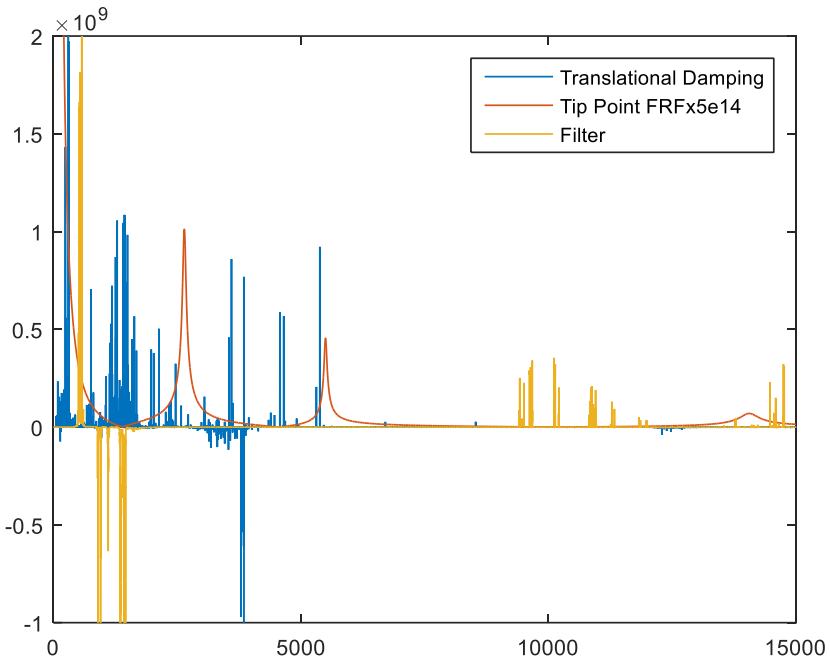

(a)

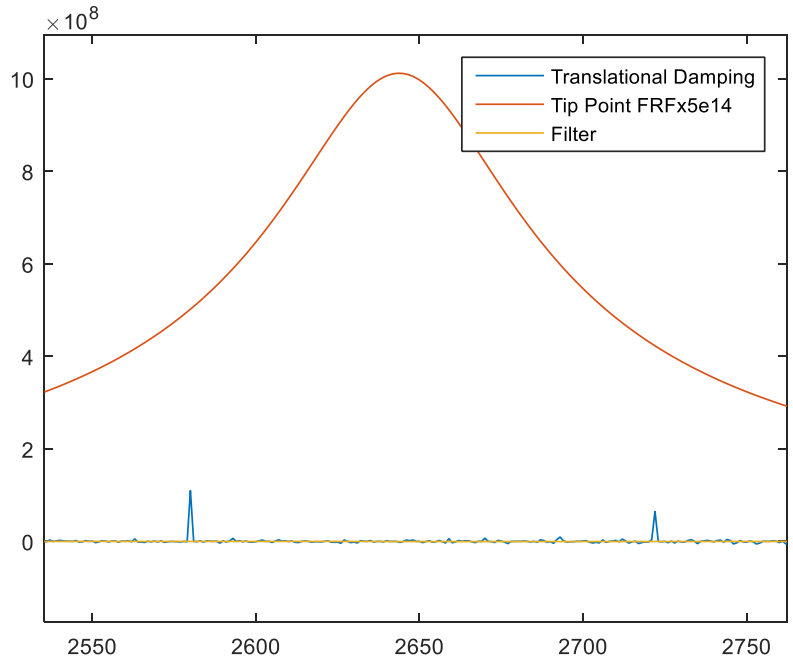

(b)

Figure 3-16 (a) Comparison of direct inverse and filtering method for translational damping values for holder-extension interface (b) Comparison of direct inverse and filtering method for translational damping values for holder-extension interface focused around the natural frequency of the assembly

CHAPTER 4

EXPERIMENTAL STUDIES

In this chapter, several experiments are performed to verify the FEM and contact indentification approach. In section 4.1, a brief information about the experimental set-up is given. In section 4.2, a modal test is performed with steel extension (HAIMER 77.202.08) and HAIMER steel shrink fit holder (HAIMER A63.140.20) and tip point FRF of the assembly is measured. Then, the tool (HAIMER F2004NNH0800CDA) is inserted to the extension and modal test performed again and tool tip point FRF is measured. In section 4.3, different extension and tool overhang is tested. In section 4.4, the dynamic properties of the contact interface are recalculated using experimental results. Lastly, result of the experimental identification outcomes are summed up and conclusions of performed experiments are given.

4.1 Experimental Set-up

In the experiment, CutPro simulation software, PCB miniature sensors and impact hammer were used. The sensitivity of the PCB 086C01 modal impact hammer is 11.2 mV/N and sensitivity of the PCB 352C23 accelerometer is 5.2 mV/N.

To simulate the free-free boundary conditions, a soft sponge is used as shown in Figure 4-1 . It does not restrict the motion and the part we examine behaves like two ends of it is free.

4.2 Modal Test

4.2.1 Holder- Extension Assembly

In the first set-up, holder and extension assembly are used. Using the impact hammer, the tip of the extension is excited as seen in Figure 4-1 and displacement-force results are obtained as in Figure 4-2.

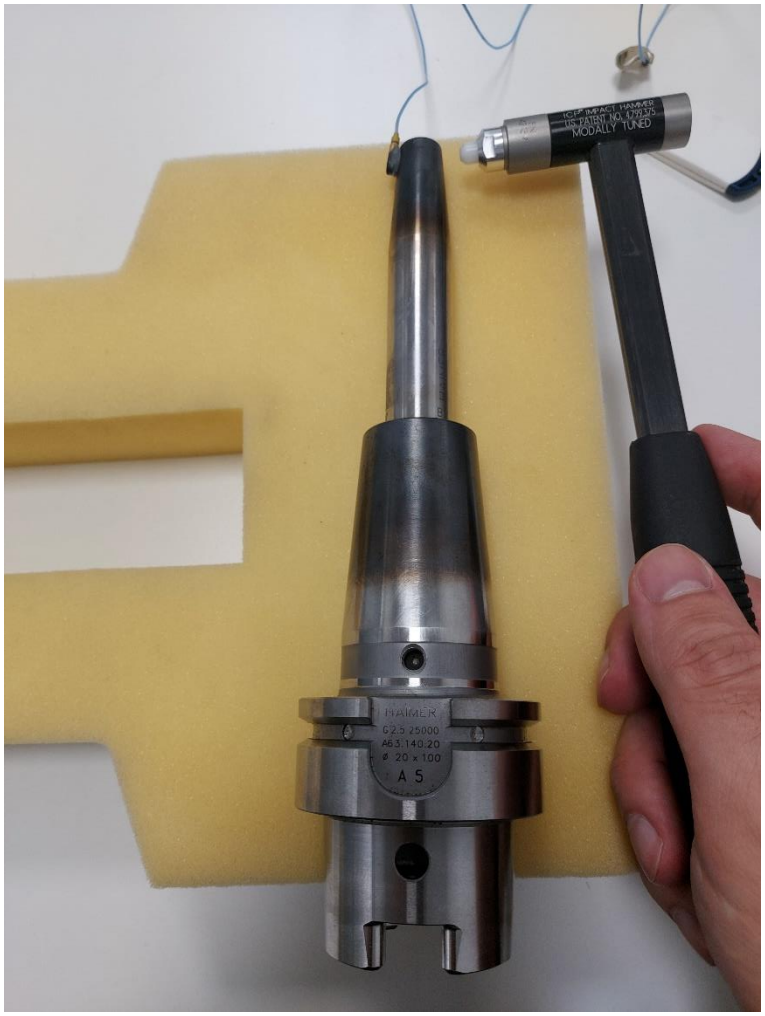

Figure 4-1 Modal testing of holder-extension assembly

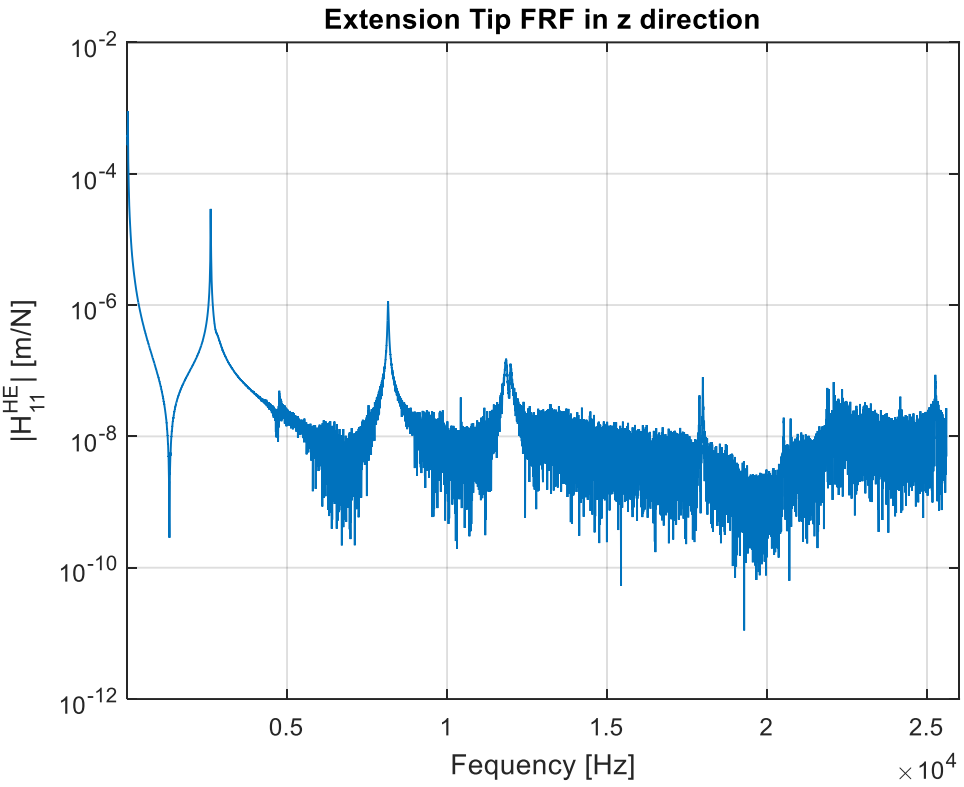

Figure 4-2 FRF of tip of the extension

4.2.2 Holder-Extension-Tool Assembly

In the second set-up, the tool is also inserted into the extension. Using the impact hammer, the tip of the tool is excited as seen in Figure 4-3. Displacement-force results for the tool tip are obtained as in Figure 4-4.

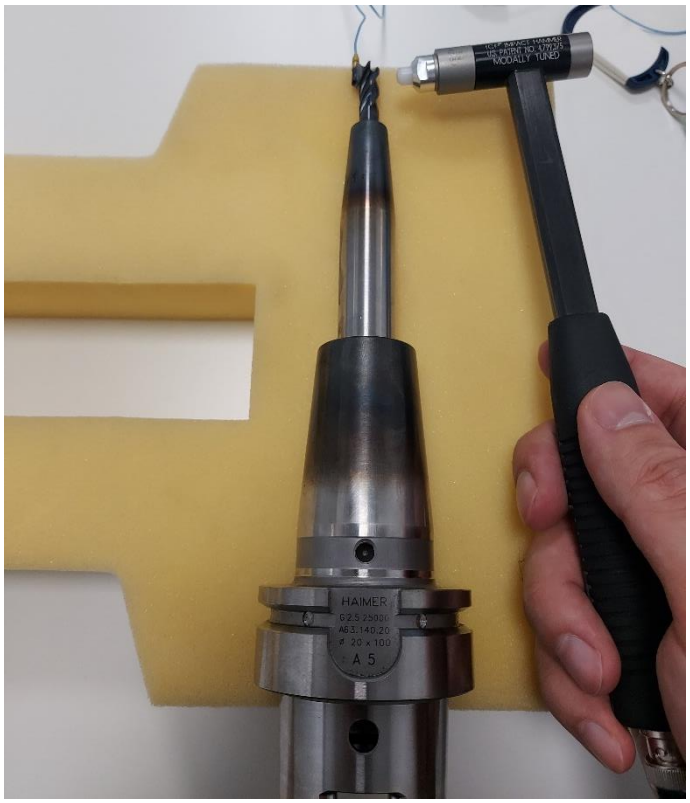

Figure 4-3 Modal testing of holder-extension assembly at the tip of the tool

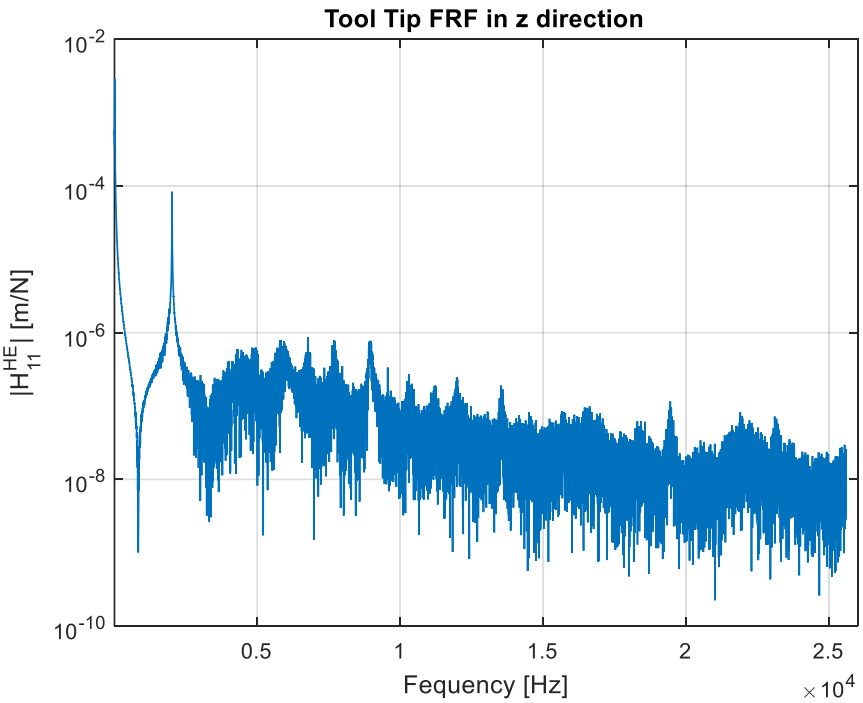

Figure 4-4 FRF of tip of the tool excited at the tip of the tool

As seen in Figures 4-2 and 4-4 there is a significant noise in experimental values after 4000 Hz. This is because the hammer test make reliable measurements for the low frequencies. It can be seen at the coherence graph for the holder-extension assembly in Figure 4-5, the coherence values are stable at lower frequencies. Therefore, the results for higher frequencies are not reliable, but it gives a rough information about the natural frequency of the system.

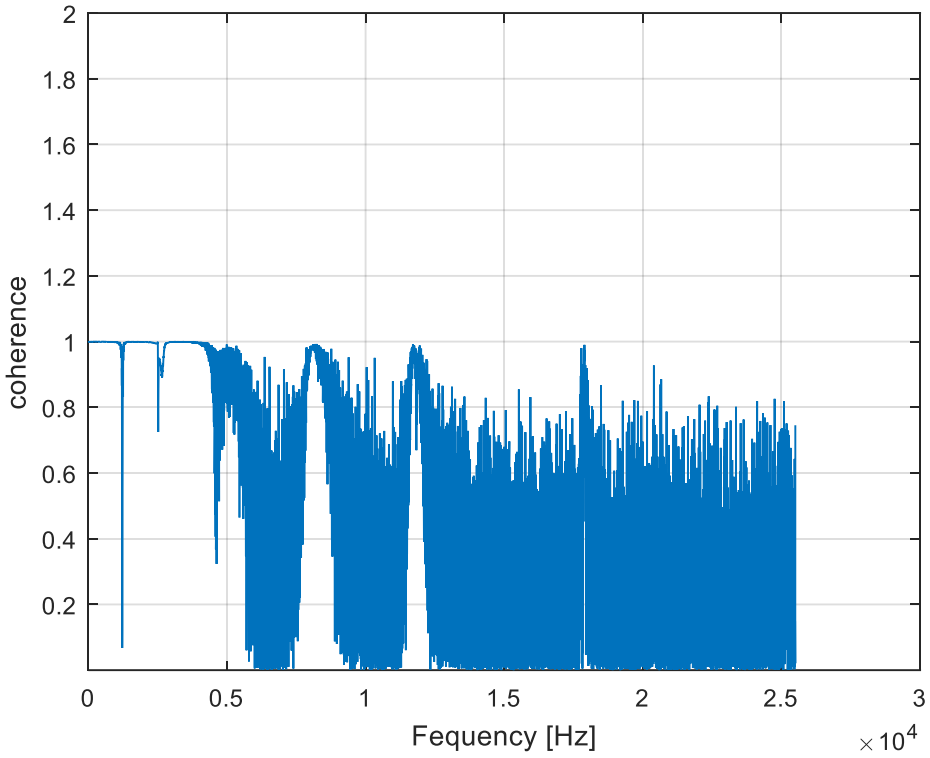

Figure 4-5 Coherence values for the holder-extension assembly

4.3 Testing Different Extension and Tool Overhang

In this section, the finite element simulations and experiments are repeated with different extension and tool overhang. First, with constant extension overhang (87 mm), the tool overhang is changed. 3 different tests are performed. The tool tip FRF for the 29 mm, 39 mm and 49 mm tool overhang is given in Figures 4-6 to 4-8

respectively. It is seen that the first mode of the assembly matches for both methods. However, for the other modes, the graphs are quite different. For the 39 mm overhang, the FRF obtained from the RCSA method is also given. The first and second natural frequency of the assembly obtained from the experiment are 1827 Hz and 4467 Hz respectively. The error percentages of the natural frequencies obtained from PATRAN and RCSA method is given in Table 4.1. It is seen that the RCSA method also gives accurate results for the first mode.

Table 4-1 Error percentages of the natural frequencies for the holder-extension-tool assembly

	First mode [Hz]	% error	Second Mode [Hz]	% error
Patran	1855	1.53	3460	22.54
RCSA	1863	1.97	3767	15.67

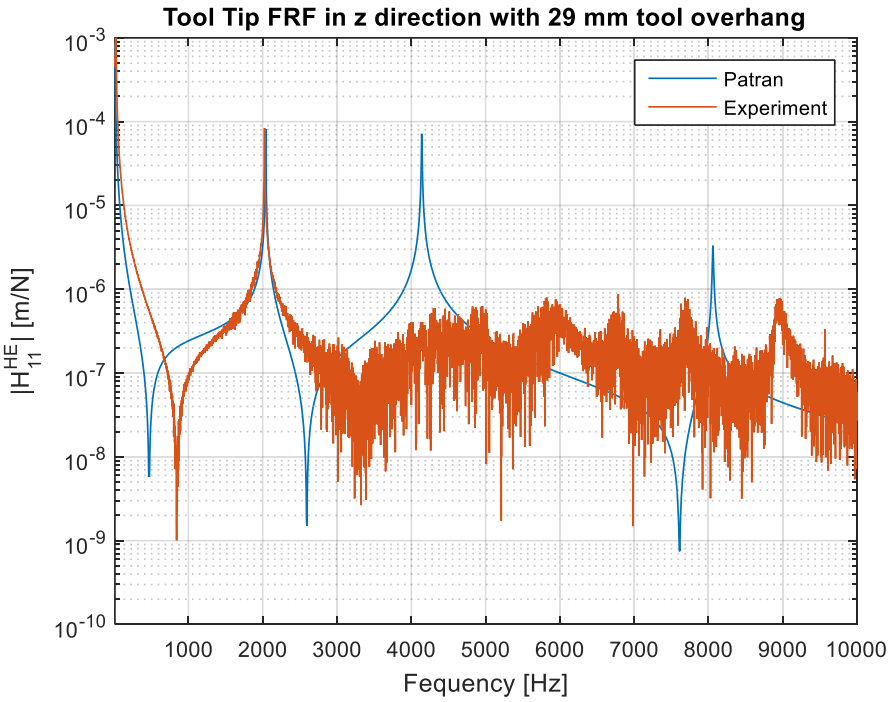

Figure 4-6 Tool tip FRF in z direction with 29 mm tool overhang

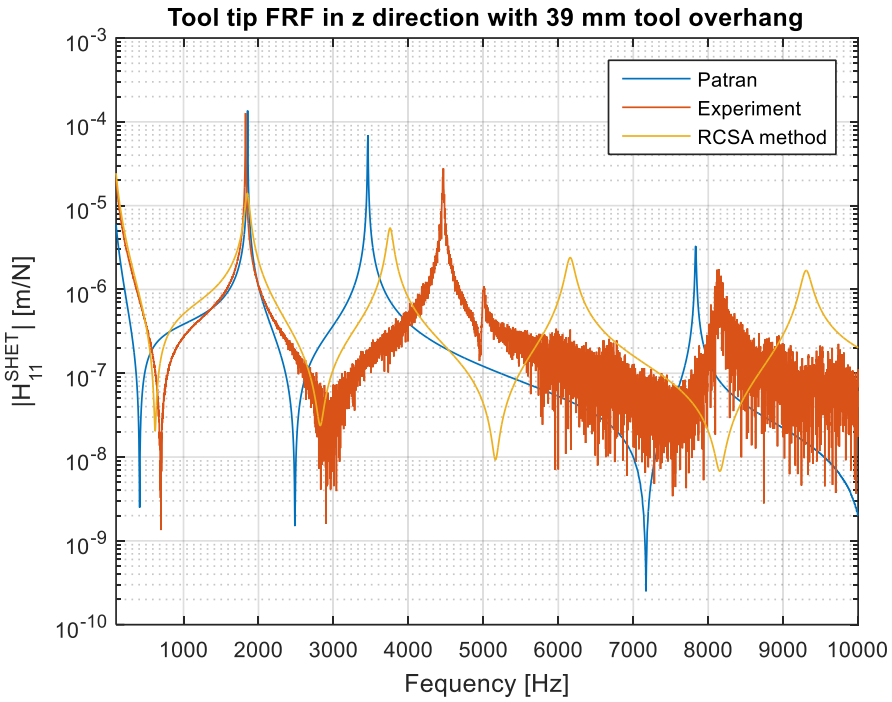

Figure 4-7 Tool tip FRF in z direction with 39 mm tool overhang

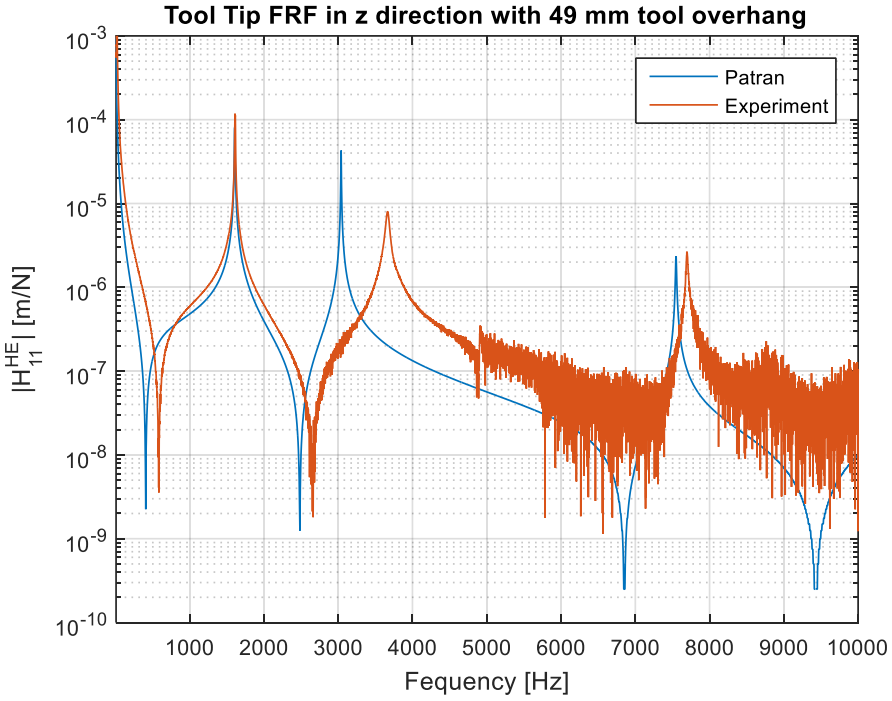

Figure 4-8 Tool tip FRF in z direction with 49 mm tool overhang

Then, the tool is removed, and the experiments and simulations are performed with only the holder and the extension. Extension tip FRF is measured with 10 different extension overhangs from 87 to 114 mm with 3 mm of increments. The comparison of the extension tip FRFs are given in Figures 4-9 to 4-18 respectively. It is seen that the first mode of the assembly matches for both methods. However, for the other modes, the graphs are quite different. For the extension-holder assembly the results are more reasonable than the holder-extension-tool assembly. It is because for the holder-extension-tool assembly two contacts are considered and error in calculating the contact dynamics are added up. In addition, complex fluted section of the tool is modeled approximately, so its dynamic behavior may differ from the real part. For the 87 mm overhang, the FRF obtained from the RCSA method is also given. The first and second natural frequency of the assembly obtained from the experiment are 2316 Hz and 8163 Hz respectively. The error percentages of the natural frequencies obtained from PATRAN and RCSA method is given in Table 4.2. It is seen that the RCSA method also gives accurate results for the first mode.

Table 4-2 Error percentages of the natural frequencies for the holder-extension assembly

	First mode [Hz]	% error	Second Mode [Hz]	% error
Patran	2640	1.03	7900	3.22
RCSA	2643	1.15	5488	32.77

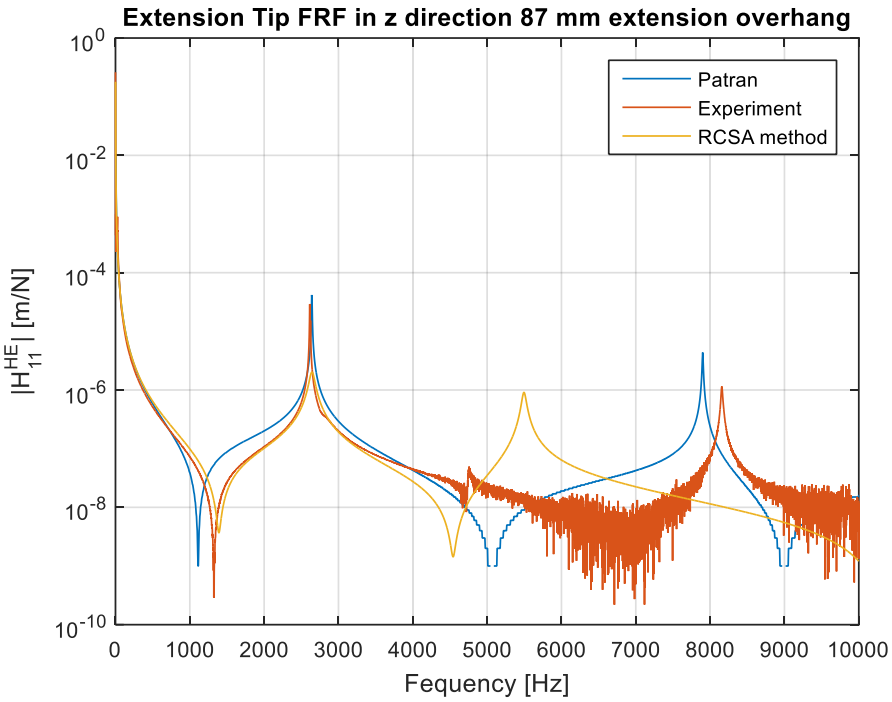

Figure 4-9 Extension Tip FRF in z direction with 87 mm extension overhang

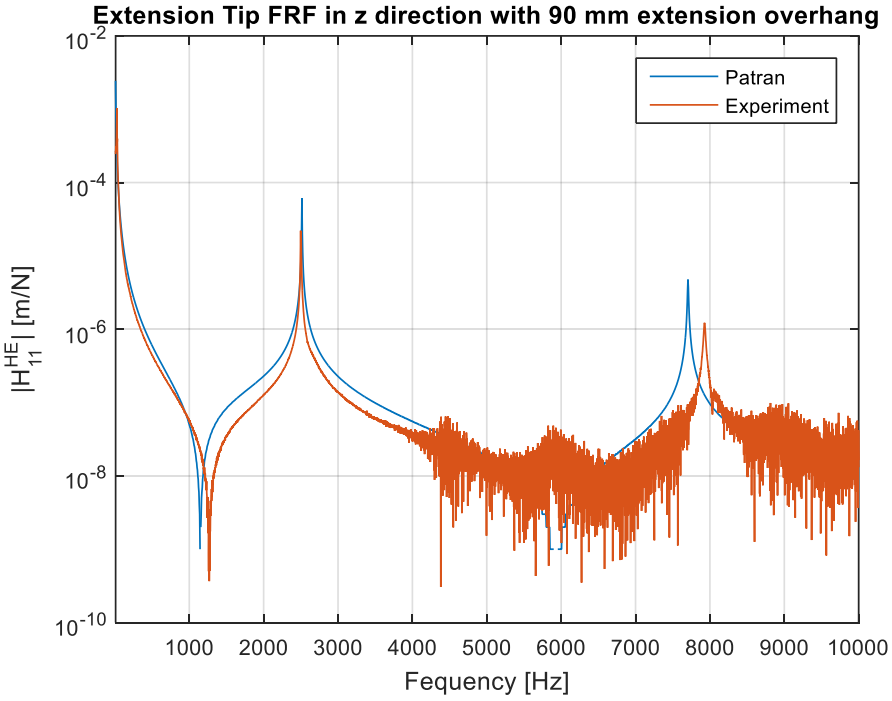

Figure 4-10 Extension Tip FRF in z direction with 90 mm extension overhang

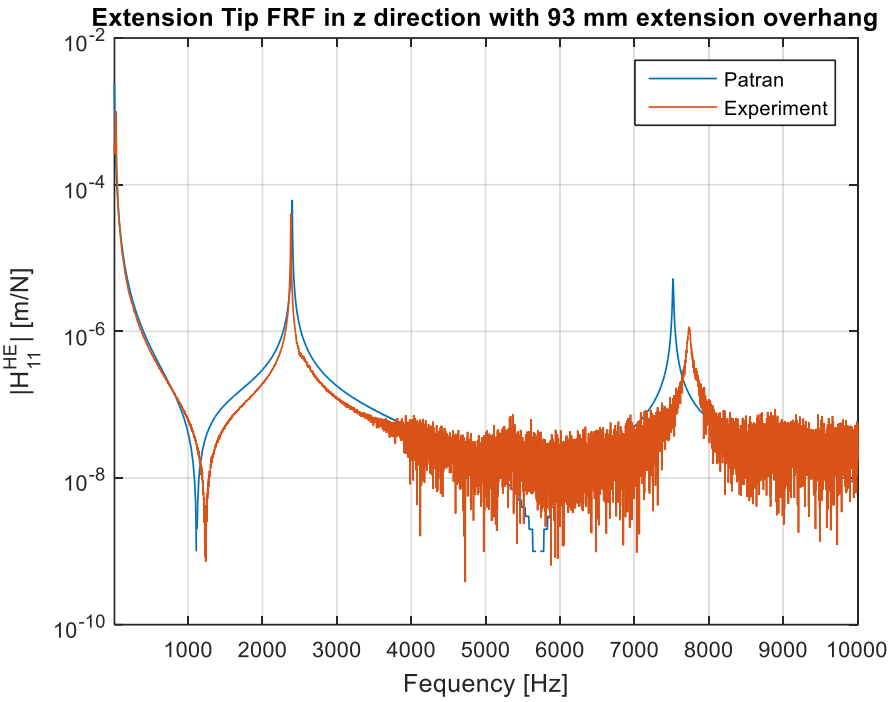

Figure 4-11 Extension Tip FRF in z direction with 93 mm extension overhang

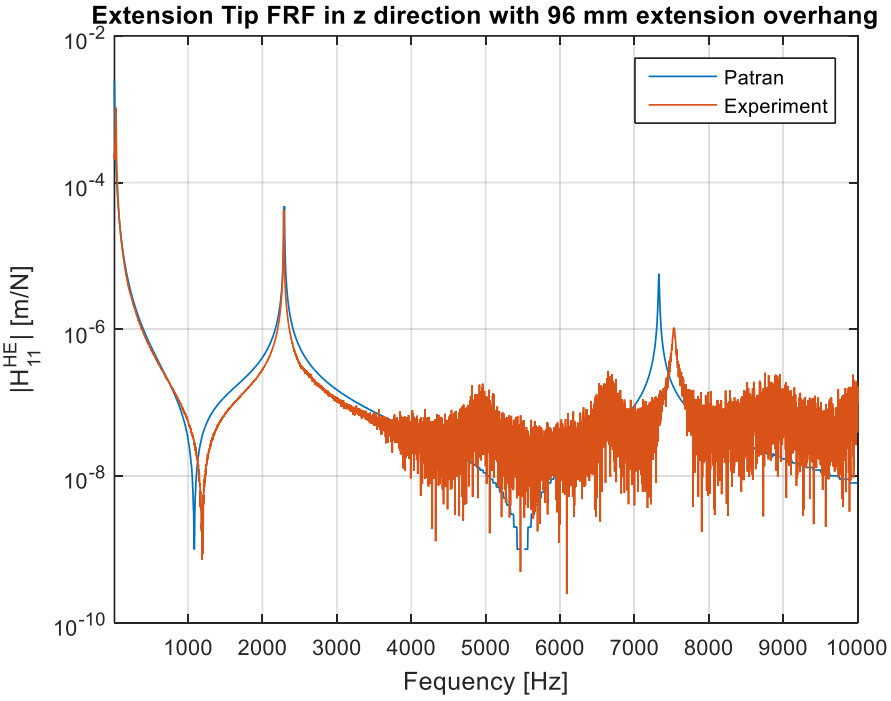

Figure 4-12 Extension Tip FRF in z direction with 96 mm extension overhang

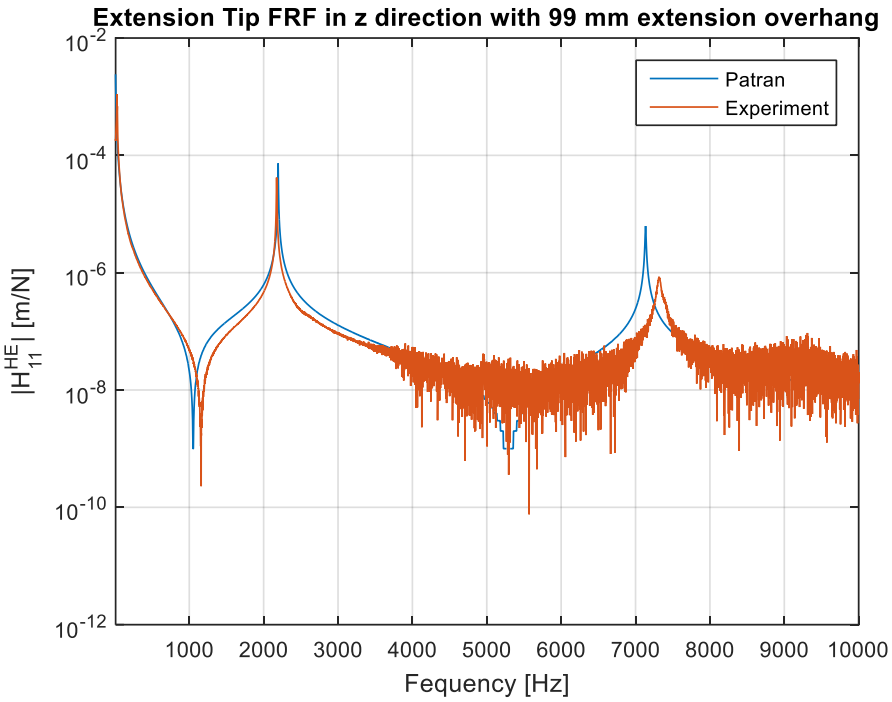

Figure 4-13 Extension Tip FRF in z direction with 99 mm extension overhang

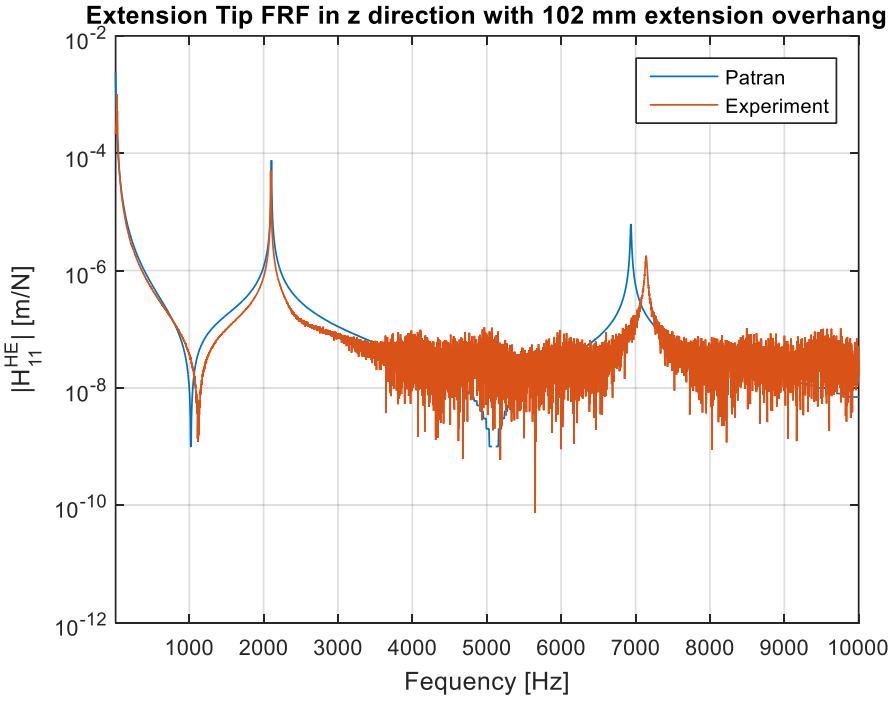

Figure 4-14 Extension Tip FRF in z direction with 102 mm extension overhang

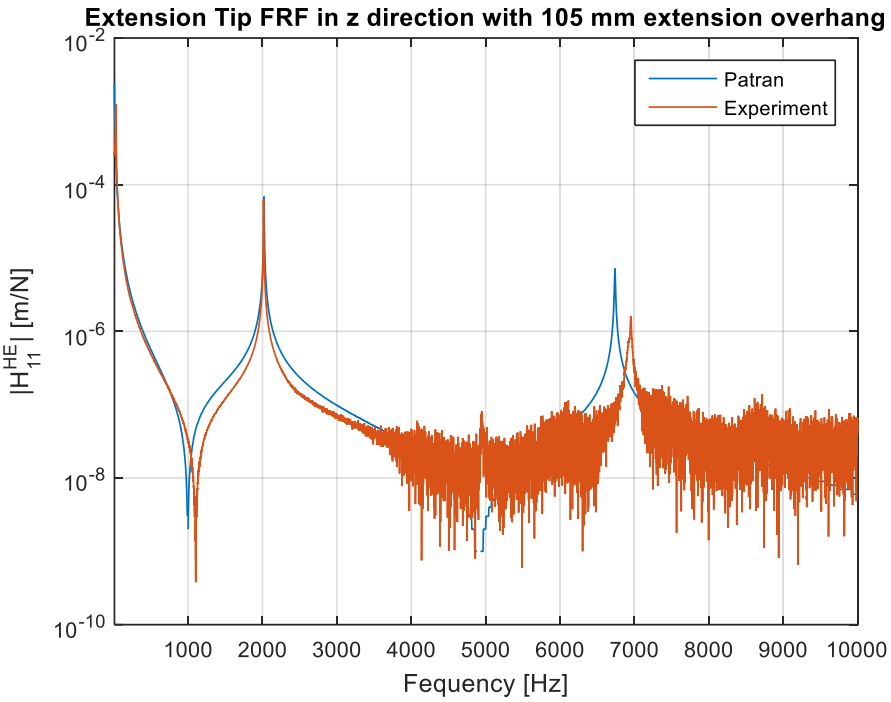

Figure 4-15 Extension Tip FRF in z direction with 105 mm extension overhang

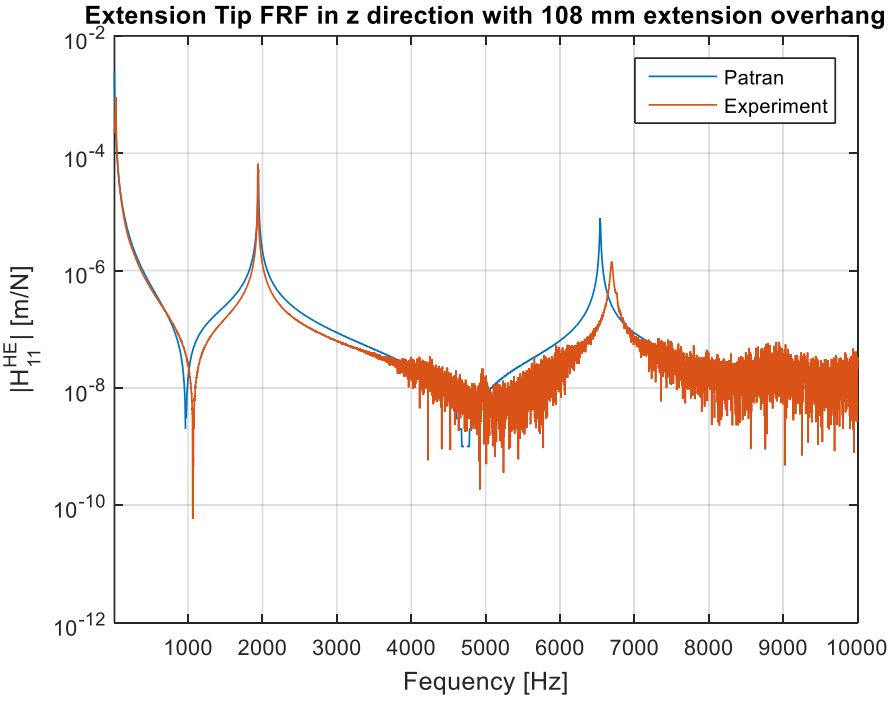

Figure 4-16 Extension Tip FRF in z direction with 108 mm extension overhang

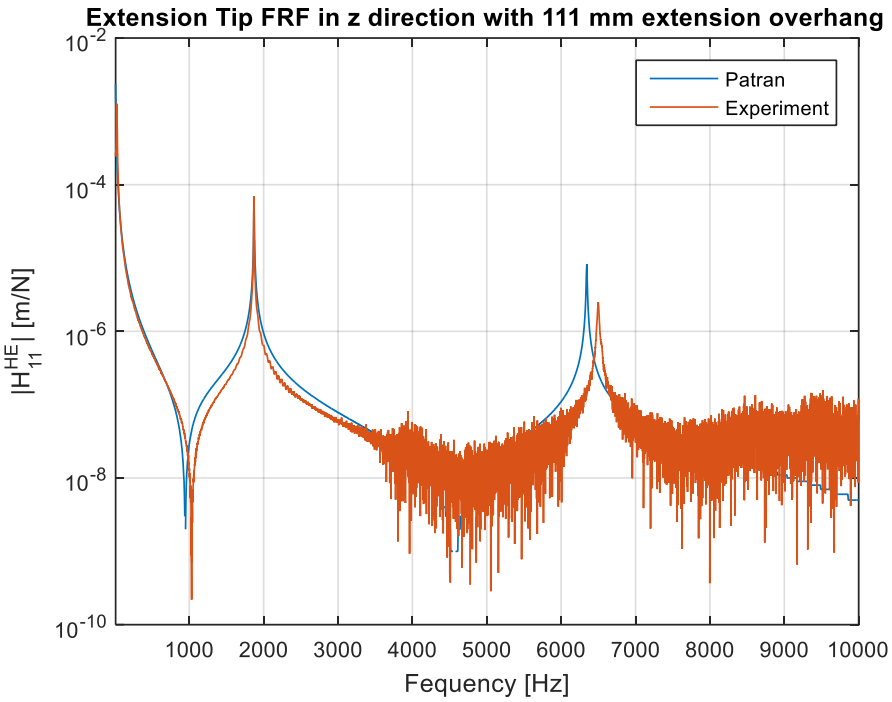

Figure 4-17 Extension Tip FRF in z direction with 111 mm extension overhang

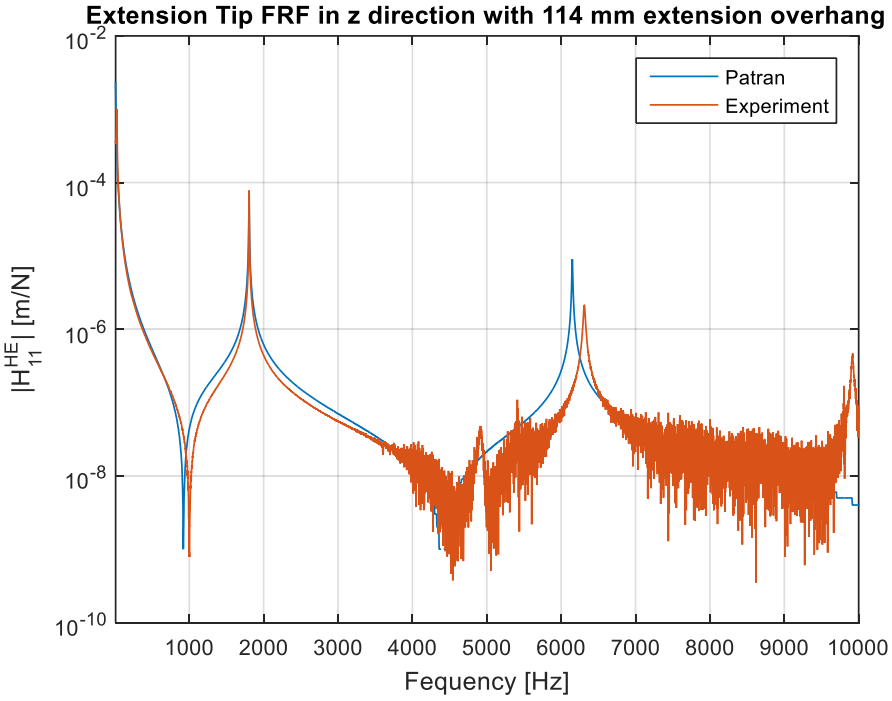

Figure 4-18 Extension Tip FRF in z direction with 114 mm extension overhang

The FRFs obtained from the experiment and PATRAN match at the first mode of the assembly, but for the other modes FRFs obtained from PATRAN has lower natural frequency. The main reason for that natural frequency of the holder. As seen in Figure 4-19 the natural frequency of the holder obtained from PATRAN is 9530 Hz and the natural frequency of the holder obtained from the experiment is 9890 Hz. This is because, when modeling the holder in PATRAN, not all the details can be meshable, so the model is simplified. This causes a difference in the FRFs for the modes except for the first one. For example, for holder-extension assembly, as seen in Figure 4-20, for the first natural frequency the effect of the extension is dominant, the holder is only rotating. However, for the second mode, the holder is also deforming and its contribution on the natural frequency of the assembly becomes significant.

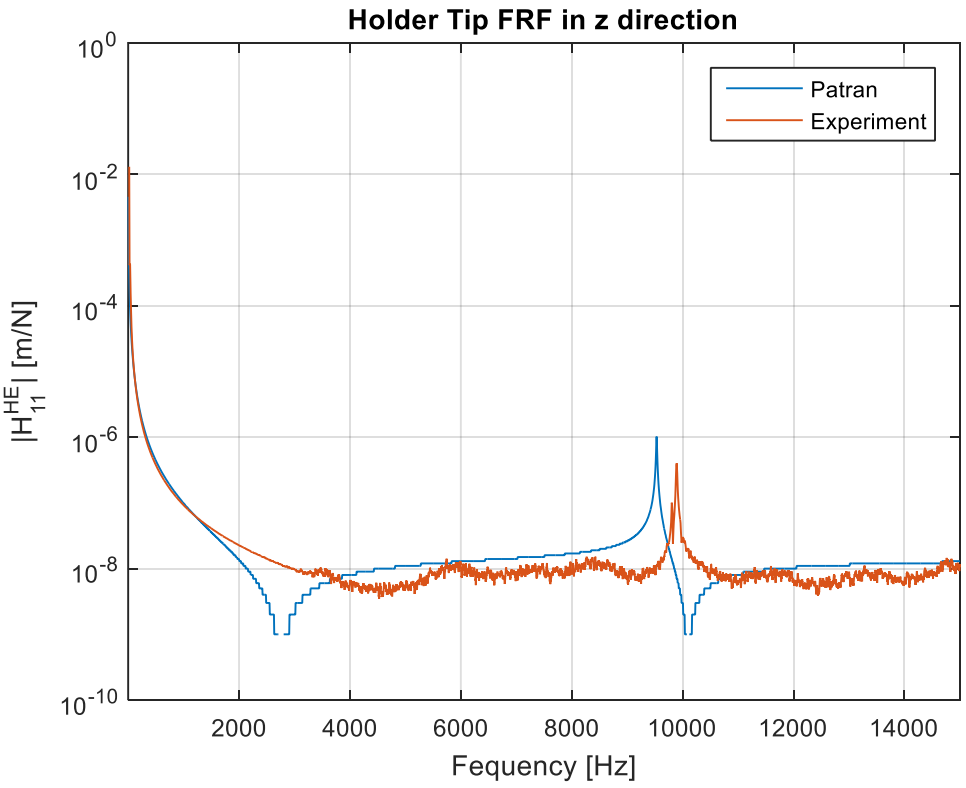

Figure 4-19 Holder tip point FRF (the experiment results are filtered)

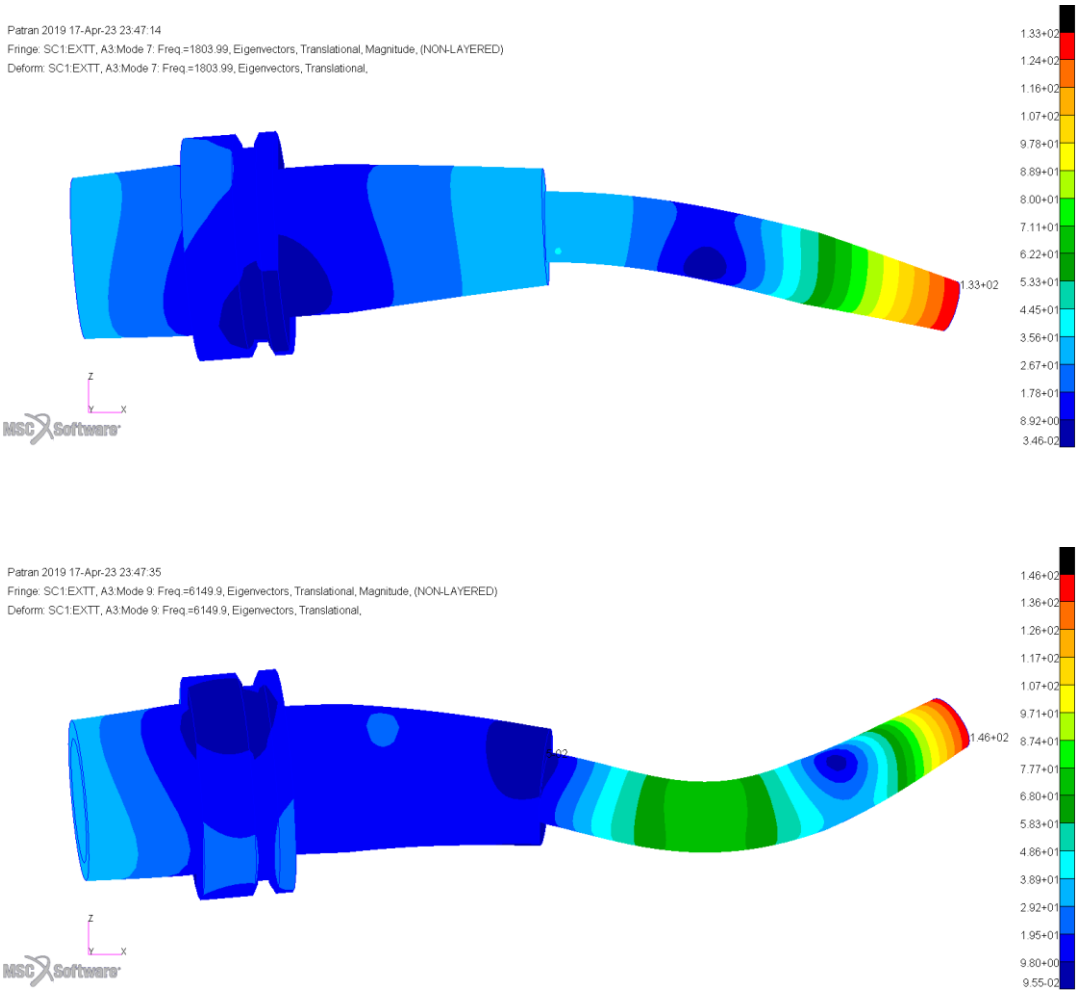

Figure 4-20 First and second mode of the holder-extension assembly

For chatter, effect of the mode with highest amplitude is dominant. For all experiments the first mode has the highest amplitude. Therefore, the first mode in the FRFs are focused. The maximum error for the first mode in every experiment is less than 2%. Schmitz et al. [1] also performed experiments with different overhang lengths. They also found that the error between the natural frequencies between experiment and simulation is around 2%. Therefore, it can be concluded that the proposed method in this thesis is accurate.

4.4 Identifying the Contact Parameters Using Experimental Results

To use the IRCSA method with the results obtained from the experiment, rotational receptances should be calculated. Three measurement points are defined for the extension with constant spacing 10 mm from each other and Equation 3.41 is used. The calculated receptances for the holder-extension assembly is given in Figures 4-21 to 4-24. Because the hammer test gives poor results for higher frequencies, the result are filtered and results up to 10 KHz are given.

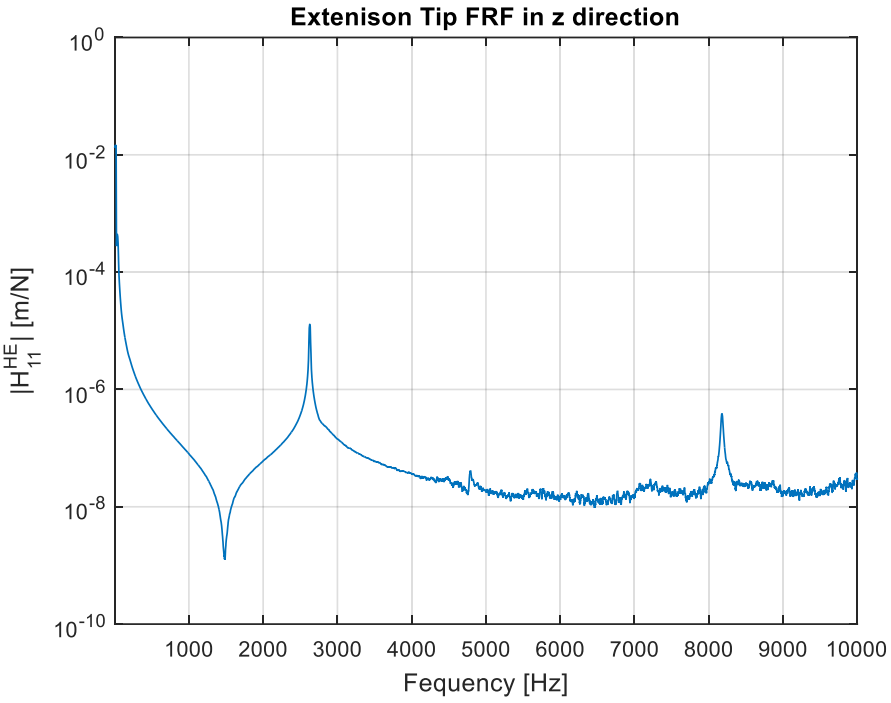

Figure 4-21 Approximately obtained extension force-to-displacement tip point FRF of the holder-extension assembly

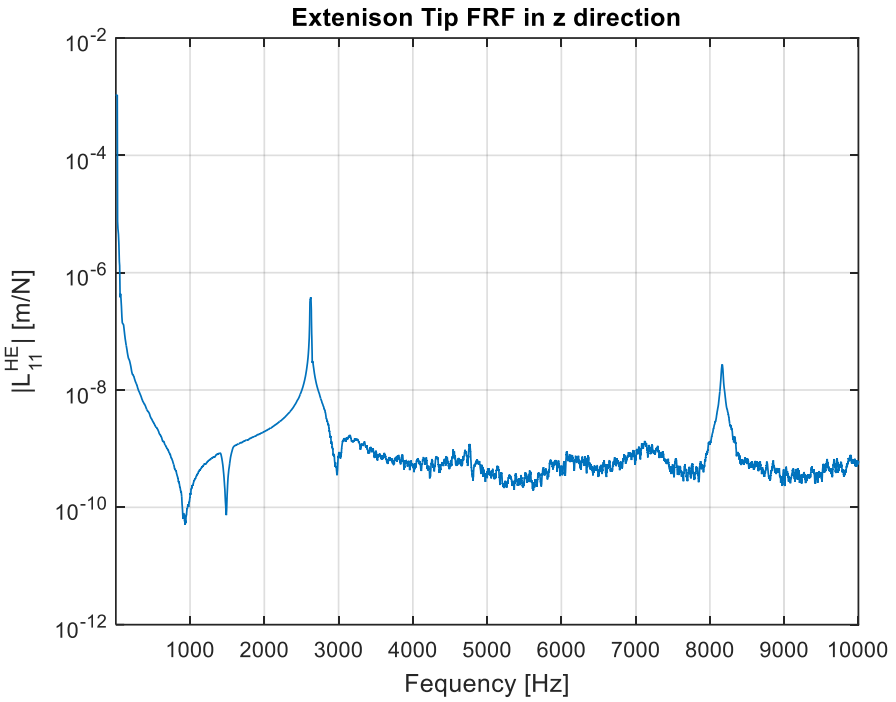

Figure 4-22 Approximately obtained extension moment-to-displacement tip point FRF of the holder-extension assembly

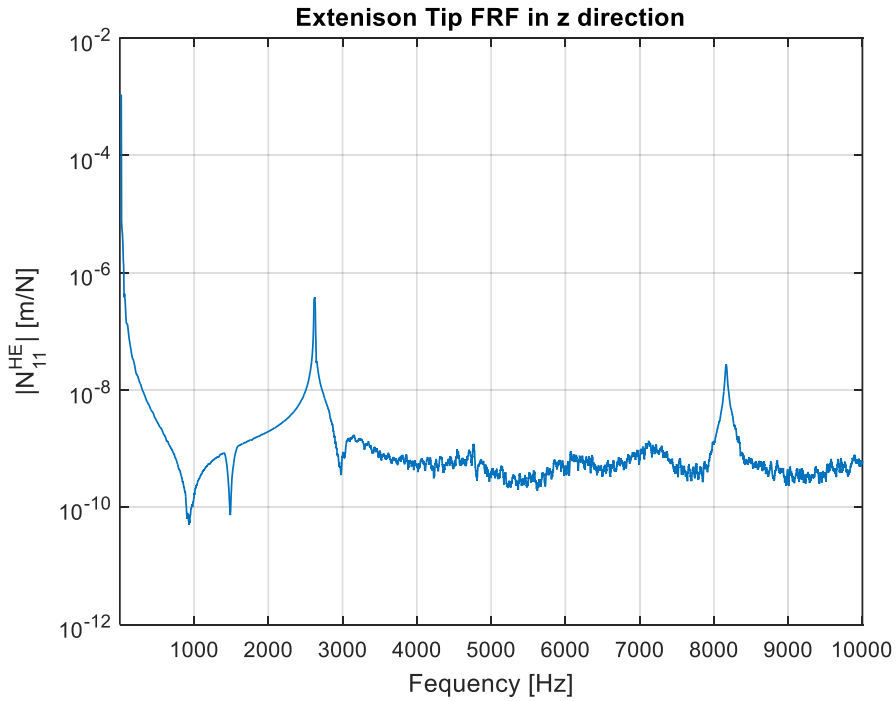

Figure 4-23 Approximately obtained extension force-to-rotation tip point FRF of the holder-extension assembly

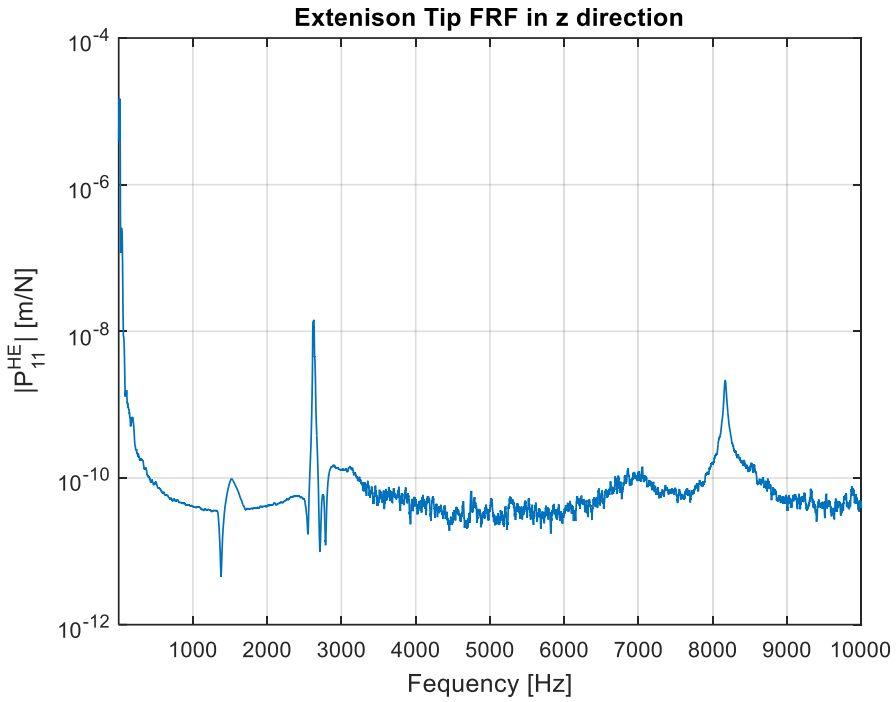

Figure 4-24 Approximately obtained extension moment-to-rotation tip point FRF of the holder-extension assembly

Using the receptance matrices above, the translational stiffness and damping values are recalculated using IRCSA method. The receptance matrices for the extension and the holder is still used the ones obtained analytically. The calculated contact parameters are given in Figures 4-25 and 4-26. As stated in Chapter 2, the contact interface is considered as two springs with series connection. Therefore, the dynamic properties of the contact region are calculated as adding up the stiffness values at the tip and end of the contact region. For the damping properties the average value for the whole contact region is calculated. The translational stiffness and translational damping values obtained from PATRAN is $1.07*10^8$ N/m and $3.8*10^4$ Ns/m respectively as given in Table 2-5. For the case with experimental results, the average values between 2600 Hz and 2650 Hz are used because the first natural frequency is 2620 Hz. The translational stiffness value is obtained as $3.41*10^7$ N/m and translational damping value is obtained as $1.08*10^6$ Ns/m. For matrix inversion to use IRCSA method, built in inverse function in MATLAB is used, because as

examined in Chapter 3, directly inversing of the matrices gives better results from the alternative inversion methods. There is a dramatic difference between the values obtained from the PATRAN and the experiment. The main reason of this is that the rotational FRFs of the experiment is calculated using an approximate method. The accuracy of this method is highly dependent on the spacing between the excitation points. Because experiments are performed by a human, the hammer cannot always be hit the same point as the accelerometer. And the formulation gives an approximate value for the rotational FRFs. Therefore, the difference between these values are expected.

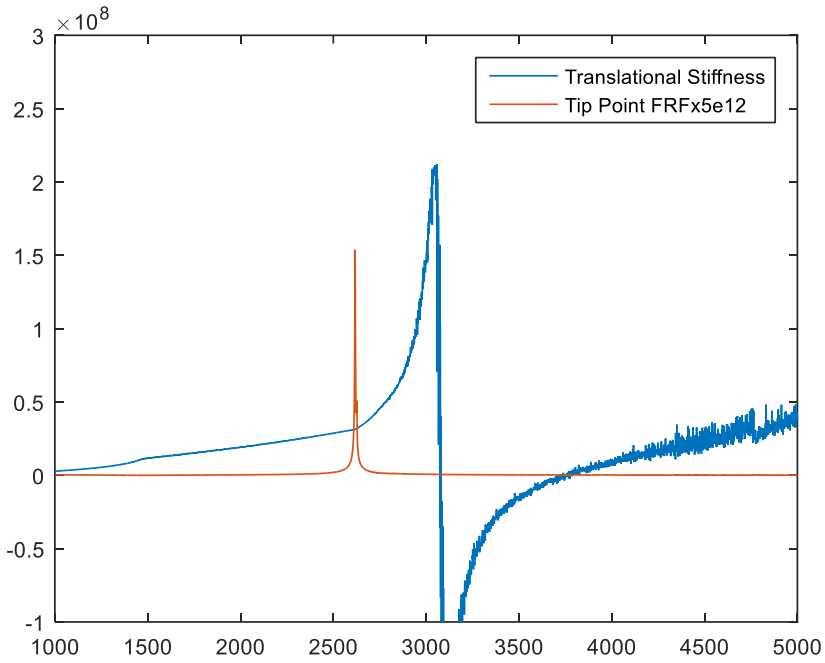

Figure 4-25 Calculated translational stiffness values for the holder-extension interface using experimental results

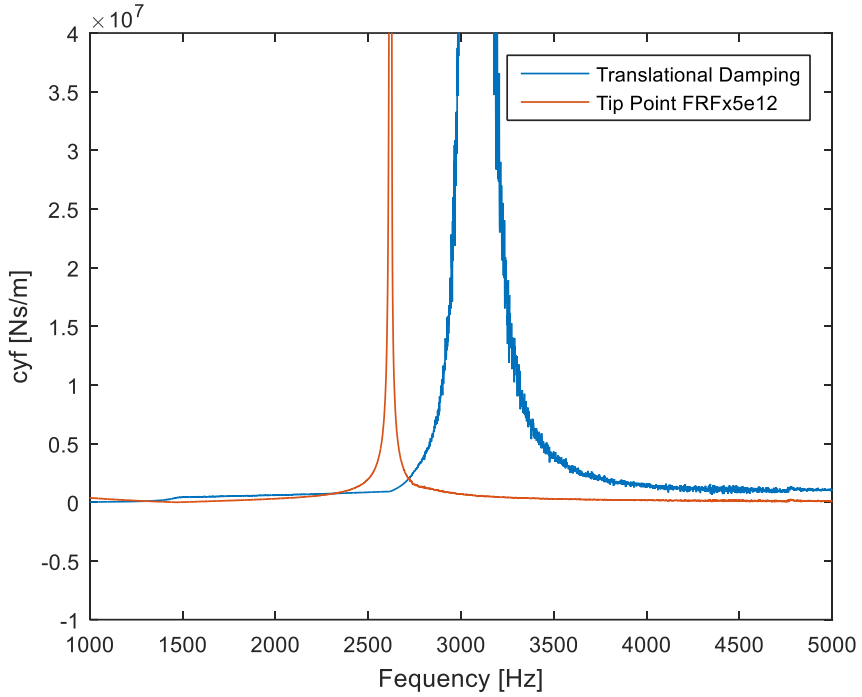

Figure 4-26 Calculated translational damping values for the holder-extension interface using experimental results

To apply IRCSA method to the extension-tool interface, three measurement points are defined for the extension with constant spacing 8.5 mm from each other and Equation 3.41 is used. The calculated receptances for the holder-extension assembly is given in Figures 4-27 to 4-30. Because the hammer test gives poor results for higher frequencies, the result are filtered and results up to 10 KHz are given.

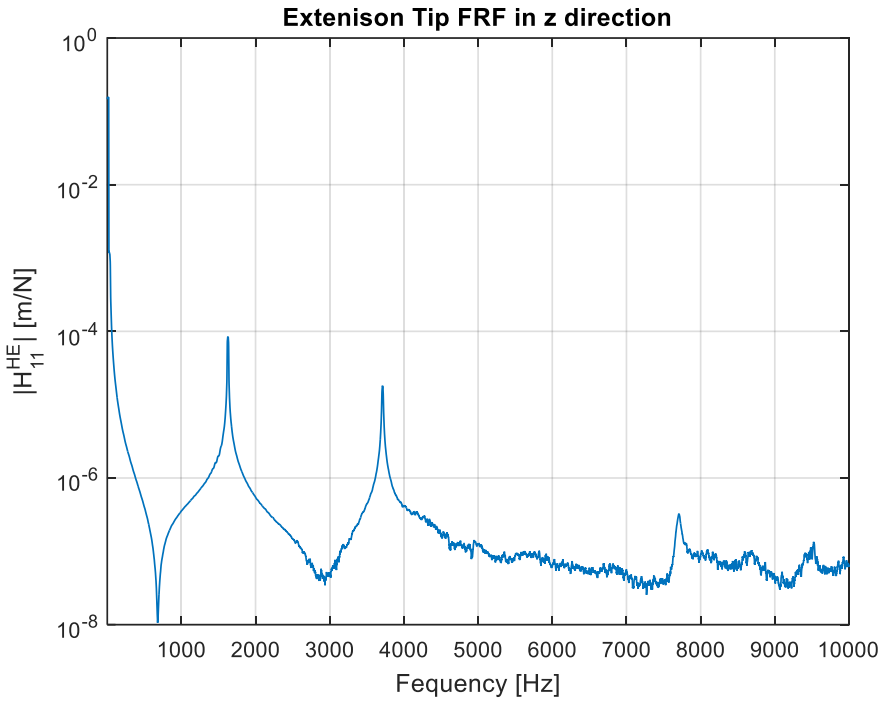

Figure 4-27 Approximately obtained tool force-to-displacement tip point FRF of the holder-extension-tool assembly

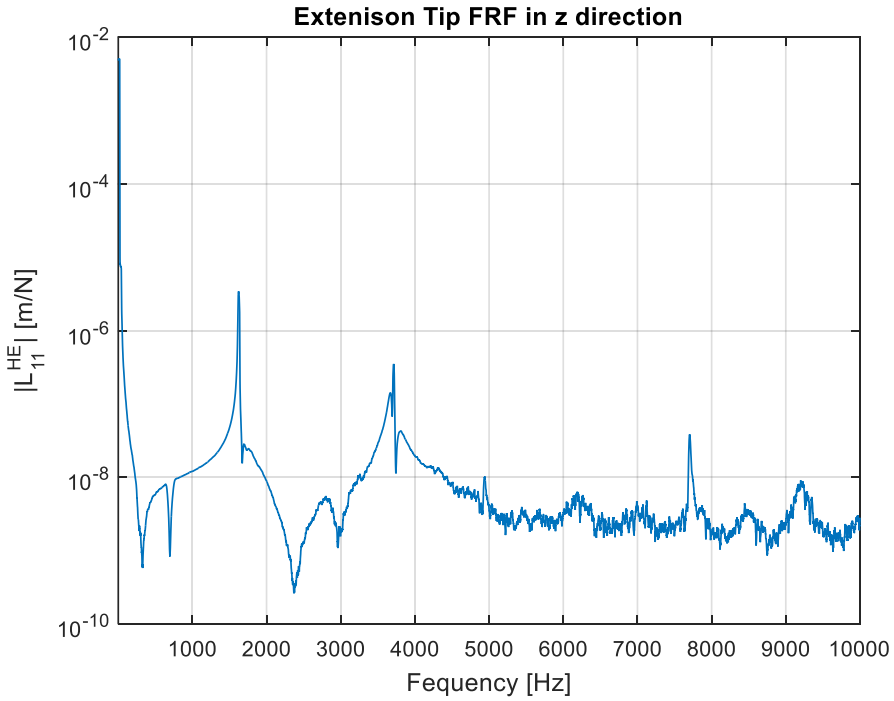

Figure 4-28 Approximately obtained tool moment-to-displacement tip point FRF of the holder-extension-tool assembly

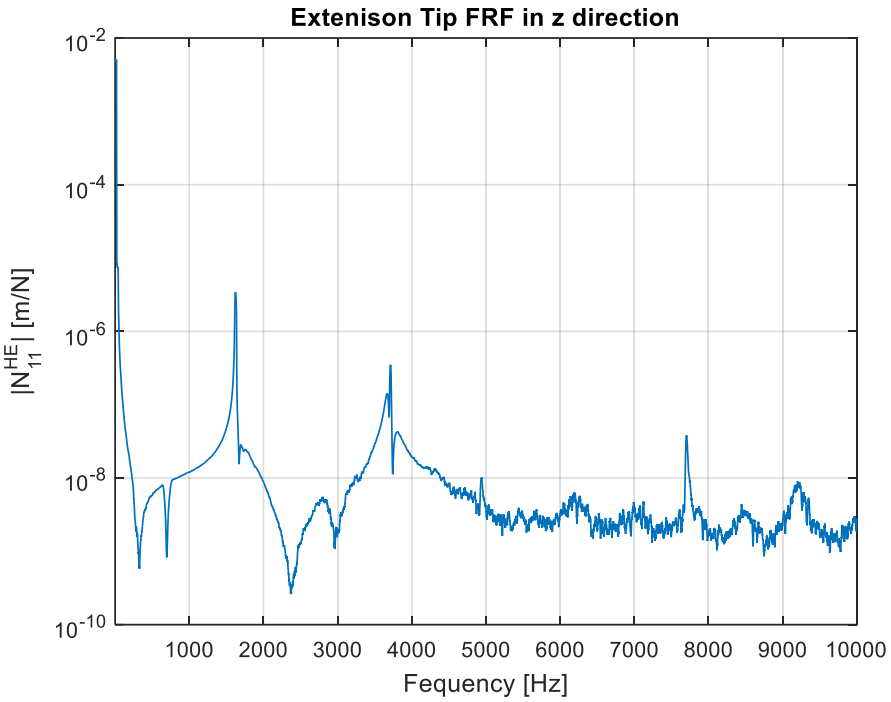

Figure 4-29 Approximately obtained tool force-to-rotation tip point FRF of the holder-extension-tool assembly

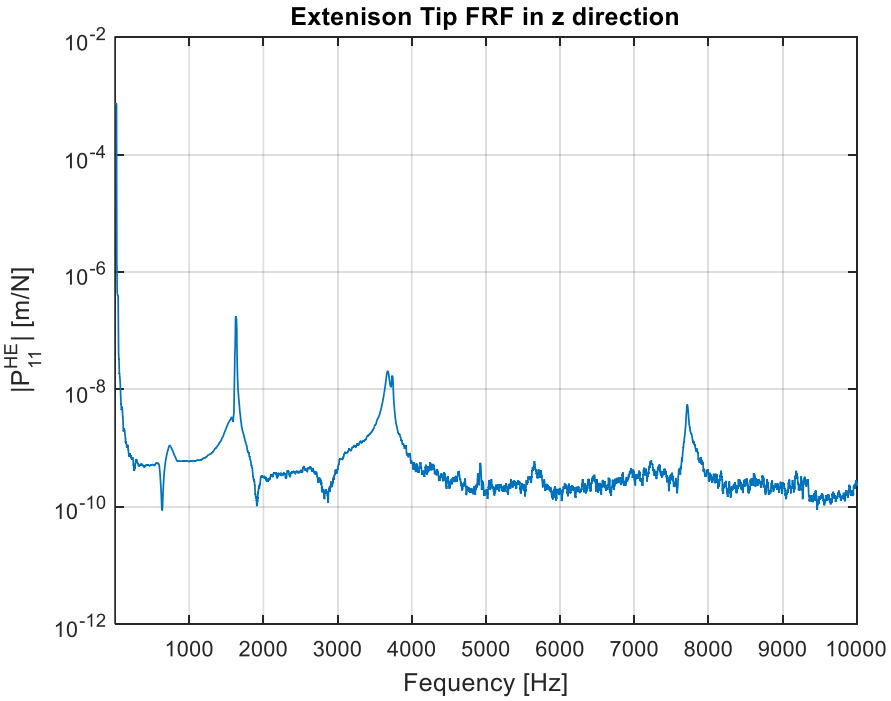

Figure 4-30 Approximately obtained tool moment-to-rotation tip point FRF of the holder-extension-tool assembly

Using the receptance matrices above, the translational stiffness and damping values are identified using IRCSA method. The receptance matrices for the tool is still used by the ones obtained analytically. The identified contact parameters are given in Figures 4-31 and 4-32. As explained for the holder-extension assembly, the translational stiffness and translational damping values obtained from PATRAN was $2.86*10^6$ N/m and $8*10^3$ Ns/m respectively. The translational stiffness value is obtained as $8.2*10^5$ N/m and translational damping value is obtained as $5.5*10^2$ Ns/m. For the case with experimental results, the average values between 1600 Hz and 1650 Hz are used because the first natural frequency is 1620 Hz. For matrix inversion to use IRCSA method, built in inverse function in MATLAB is used, because as explained for the holder-extension assembly, it gives the best results. The main reason for this dramatic difference is the same as the holder-extension assembly. It is caused by the human factor and approximately calculated rotational FRFs. Therefore, the difference between these values are expected.

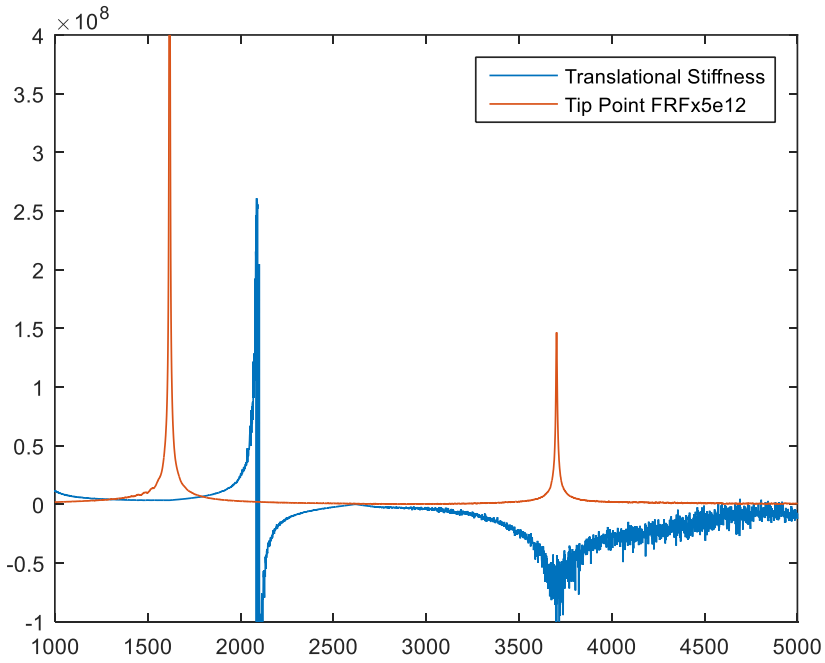

Figure 4-31 Calculated translational stiffness values for the extension-tool interface using experimental results

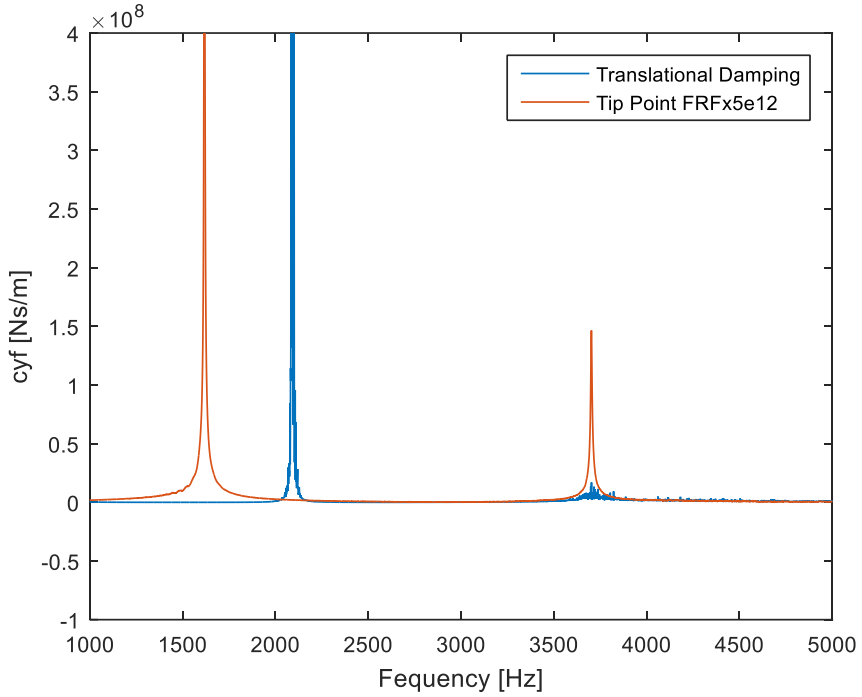

Figure 4-32 Calculated translational damping values for the extension-tool interface using experimental results

In this chapter, results obtained from the experiment using holder-extension and holder-extension-tool assembly is given. Tip point FRFs obtained from PATRAN, RCSA method and experiment are compared. The FRFs obtained from PATRAN are remarkably close to experimental FRFs. Therefore, validity of the Finite element modeling is proved. However, the RCSA method gives poor result, because of the errors in calculating receptances and assumption made to apply dynamic properties to the method. In addition, dynamic properties are recalculated using experimental values and compared with the ones obtained from PATRAN.

CHAPTER 5

CONCLUSION AND FUTURE WORK

5.1 Conclusion

In this study, using Finite element modeling with MSC PATRAN, distributed dynamic properties of the contact region of holder-extension interface and extension-tool interface is calculated. To find the translational stiffness values, the displacements for each force increment is enlisted and slopes of the force-displacement and moment-displacement curves are used. For the rotational stiffness values, rotation is calculated using displacement values via central finite difference method and slopes of the force-rotation and moment-rotation curves are used. For damping values, damping forces and the displacements along the tool axis is enlisted and calculated damping values for the nodes along the tool circumference is summed up. However, distributed dynamic properties are not practical to use in RCSA method. Therefore, the contact between the parts are modeled as two spring-damper elements connected as series at two ends of the contact region. The two stiffness values are summed up, because they are connected in series and for the damping, the average of the damping values along the contact region is used. In addition, using PATRAN, tip point FRFs are obtained.

Using RCSA method the tip point FRFs of the holder-extension and holder-extension-tool assembly is calculated. To find the receptances of the parts individually the Timoshenko Beam Theory is used. And for the dynamic properties, the results obtained in PATRAN is used. The calculated FRFs are close the ones obtained with PATRAN and the experiment in the first mode, but for the other modes there is a significant error. The formulation used to calculate receptances and the approximation used to determine contact properties might result in this difference. Using the IRCSA method with fully analytical results, gives exactly same values for

the dynamic properties found with PATRAN. However, when the noise is added to tip point FRFs, the dynamic properties calculated with IRCSA method has huge distortion. To eliminate this problem, alternative inverse methods are used, such as Moore-Penrose Pseudoinverse, Wu's Method and filtering data before the inversion. Although, the result are more stable with the alternative inversion methods, the most accurate result are obtained with direct inverse using MATLAB.

Lastly, a series of experiments are performed to validate the methods. Three different tool overhang and ten different extension overhangs are examined. Because the hammer test is performed the accuracy of the experimental result at the higher frequencies are poor, but this method gives a rough information about the natural frequencies of the assemblies. Therefore, the result at the lower frequencies are focused on. Tip point FRFs using PATRAN, RCSA method and experiments are compared. The FRFs obtained from PATRAN are remarkably close to experimental FRFs at the first mode of assembly. For the other modes dynamic behavior of the holder caused some error because the natural frequency of the holder is different from the experimental result due to simplification at the finite element modeling. Therefore, validity of the Finite element modeling is proved. However, the RCSA method gives poor result, because of the errors in calculating receptances and assumption made to apply dynamic properties to the method. Lastly, the dynamic properties are recalculated with IRCSA method using experimental results and averaging the values close to the first natural frequency of the assembly, the approximate single value is obtained. However, there is a dramatic difference between the calculated dynamic properties and the ones obtained from the PATRAN. Because a human performs experiments, it is not possible to hit with the hammer and measure acceleration at the same point. In addition, the rotational receptances are calculated by approximate methods. Therefore, the error is expected.

5.2 Future Work

As a further work, a better application of the contact properties obtained from PATRAN to the RCSA method can be developed. Making assumptions to use as single complex stiffness matrix does not give an accurate result. Distributed contact properties can be applied to the RCSA method with an efficient way.

In addition, the calculated dynamic properties from IRCSA method is extremely sensitive to the noise in the receptances. An alternative matrix inversion method that reduces the distortions can be found.

It can also be recommended to use finite element modeling to identify contact properties of different contact regions such as bolted and riveted connections. Because the FEM is efficient and time saving to calculate tip point FRFs, the experimental dependency of these contact types can be reduced.

REFERENCES

[1] Schmitz, T. L., Powell, K., Won, D., Scott Duncan, G., Gregory Sawyer, W., & Ziegert, J. C. (2007). Shrink fit tool holder connection stiffness/damping modeling for frequency response prediction in milling. *International Journal of Machine Tools and Manufacture*, *47*(9), 1368–1380. https://doi.org/10.1016/j.ijmachtools.2006.08.009

[2] Xiao, W., Mao, K., Zhu, M., Li, B., Lei, S., & Pan, X. (2014). Modelling the spindle–holder taper joint in machine tools: A tapered zero-thickness finite element method. *Journal of Sound and Vibration*, *333*(22), 5836–5850. https://doi.org/10.1016/j.jsv.2014.06.023

[3] Liao, J., Zhang, J., Feng, P., Yu, D., & Wu, Z. (2016). Identification of contact stiffness of shrink-fit tool-holder joint based on fractal theory. *The International Journal of Advanced Manufacturing Technology*, *90*(5-8), 2173–2184. https://doi.org/10.1007/s00170-016-9506-3

[4] Gao, X., Wang, M., Zhang, Y., & Zan, T. (2016). A modeling approach for contact stiffness of spindle–tool holder based on fractal theory. *Proceedings of the Institution of Mechanical Engineers, Part B: Journal of Engineering Manufacture*, *230*(10), 1942–1951. https://doi.org/10.1177/0954405415579009

[5] Xu, C., Zhang, J., Wu, Z., Yu, D., & Feng, P. (2012). Dynamic modeling and parameters identification of a spindle–holder taper joint. *The International Journal of Advanced Manufacturing Technology*, *67*(5-8), 1517–1525. https://doi.org/10.1007/s00170-012-4586-1

[6] Xu, C., Zhang, J., Feng, P., Yu, D., & Wu, Z. (2014). Characteristics of stiffness and contact stress distribution of a spindle–holder taper joint under clamping and centrifugal forces. *International Journal of Machine Tools and Manufacture*, *82-83*, 21–28. https://doi.org/10.1016/j.ijmachtools.2014.03.006

[7] Houming, Z., Chengyong, W., & Zhenyu, Z. (2008). Dynamic characteristics of conjunction of lengthened shrink-fit holder and cutting tool in high-speed milling. *Journal of Materials Processing Technology*, *207*(1-3), 154–162. https://doi.org/10.1016/j.jmatprotec.2007.12.083

[8] Brecher, C., Chavan, P., & Fey, M. (2020). Efficient Joint Identification and fluted segment modelling of shrink-fit tool assemblies by updating extended tool models. *Production Engineering*, *15*(1), 21–33. https://doi.org/10.1007/s11740-020-00999-0

[9] Kumar, U. V., & Schmitz, T. L. (2012). Spindle Dynamics identification for receptance coupling substructure analysis. *Precision Engineering*, *36*(3), 435–443. https://doi.org/10.1016/j.precisioneng.2012.01.007

[10] Mancisidor, I., Urkiola, A., Barcena, R., Munoa, J., Dombovari, Z., & Zatarain, M. (2014). Receptance coupling for tool point dynamic prediction by fixed boundaries approach. *International Journal of Machine Tools and Manufacture*, *78*, 18–29. https://doi.org/10.1016/j.ijmachtools.2013.12.002

[11] Movahhedy, M. R., & Gerami, J. M. (2006). Prediction of spindle dynamics in milling by sub-structure coupling. *International Journal of Machine Tools and Manufacture*, *46*(3-4), 243–251. https://doi.org/10.1016/j.ijmachtools.2005.05.026

[12] Park, S. S., Altintas, Y., & Movahhedy, M. (2003). Receptance coupling for end mills. *International Journal of Machine Tools and Manufacture*, *43*(9), 889–896. https://doi.org/10.1016/s0890-6955(03)00088-9

[13] Park, S. S., & Chae, J. (2007). Joint identification of modular tools using a novel receptance coupling method. *The International Journal of Advanced Manufacturing Technology*, *35*(11-12), 1251–1262. https://doi.org/10.1007/s00170-006-0826-6

[14] Xuan, X. J., Haung, Z. H., Wu, K. D., & Hung, J. P. (2018). Prediction of the frequency response function of a tool holder-tool assembly based on receptance coupling method. *Engineering, Technology & Applied Science Research*, *8*(6), 3556–3560. https://doi.org/10.48084/etasr.2372

[15] ZHANG, J. (2011). Receptance coupling for Tool Point Dynamics Prediction on Machine Tools. *Chinese Journal of Mechanical Engineering*, *24*(03), 340. https://doi.org/10.3901/cjme.2011.03.340

[16] Agapiou, J. S. (2008). Estimating the static stiffness for a spindle-toolholder-tooling system. *Machining Science and Technology*, *12*(1), 77–99. https://doi.org/10.1080/10910340801890938

[17] Brecher, C., Chavan, P., Fey, M., & Daniels, M. (2016). A modal parameter approach for receptance coupling of Tools. *MM Science Journal*, *2016*(04), 1032–1034. https://doi.org/10.17973/mmsj.2016_10_201616

[18] Kiran, K., Satyanarayana, H., & Schmitz, T. (2017). Compensation of frequency response function measurements by inverse RCSA. *International Journal of Machine Tools and Manufacture*, *121*, 96–100. https://doi.org/10.1016/j.ijmachtools.2017.04.004

[19] Namazi, M., Altintas, Y., Abe, T., & Rajapakse, N. (2007). Modeling and identification of Tool Holder–Spindle Interface Dynamics. *International Journal of Machine Tools and Manufacture*, *47*(9), 1333–1341. https://doi.org/10.1016/j.ijmachtools.2006.08.003

[20] Özşahin, O., Ertürk, A., Özgüven, H. N., & Budak, E. (2009). A closed-form approach for identification of dynamical contact parameters in spindle–holder–tool assemblies. *International Journal of Machine Tools and Manufacture*, *49*(1), 25–35. https://doi.org/10.1016/j.ijmachtools.2008.08.007

[21] Ertürk, A., Özgüven, H. N., & Budak, E. (2006). Analytical modeling of Spindle–tool dynamics on machine tools using Timoshenko Beam model and receptance coupling for the prediction of Tool Point FRF. *International Journal of Machine Tools and Manufacture*, *46*(15), 1901–1912. https://doi.org/10.1016/j.ijmachtools.2006.01.032

[22] Matthias, W., Özşahin, O., Altintas, Y., & Denkena, B. (2016). Receptance coupling based algorithm for the identification of contact parameters at holder–tool interface. *CIRP Journal of Manufacturing Science and Technology*, *13*, 37–45. https://doi.org/10.1016/j.cirpj.2016.02.005

[23] Özşahin, O., & Altintas, Y. (2015). Prediction of frequency response function (FRF) of asymmetric tools from the analytical coupling of spindle and beam models of holder and tool. *International Journal of Machine Tools and Manufacture*, *92*, 31–40. https://doi.org/10.1016/j.ijmachtools.2015.03.001

[24] Kiran, K. (2022). A receptance coupling procedure considering frequency-dependent behavior of holder-tool contact dynamics. *Journal of Manufacturing Processes*, *80*, 624–641. https://doi.org/10.1016/j.jmapro.2022.06.007

[25] Albertelli, P., Goletti, M., & Monno, M. (2013). A new receptance coupling substructure analysis methodology to improve chatter free cutting conditions prediction. *International Journal of Machine Tools and Manufacture*, *72*, 16–24. https://doi.org/10.1016/j.ijmachtools.2013.05.003

[26] Ealo, J. A., Garitaonandia, I., Fernandes, M. H., Hernandez-Vazquez, J. M., & Muñoa, J. (2018). A practical study of joints in three-dimensional inverse receptance coupling substructure analysis method in a horizontal milling machine. *International Journal of Machine Tools and Manufacture*, *128*, 41–51. https://doi.org/10.1016/j.ijmachtools.2018.02.002

[27] Ahmadi, K., & Ahmadian, H. (2007). Modelling Machine Tool Dynamics using a distributed parameter tool–holder joint interface. *International Journal of Machine Tools and Manufacture*, *47*(12-13), 1916–1928. https://doi.org/10.1016/j.ijmachtools.2007.03.004

[28] Yigit, A. S., & Ulsoy, A. G. (2002). Dynamic stiffness evaluation for reconfigurable machine tools including weakly non-linear joint characteristics. *Proceedings of the Institution of Mechanical Engineers, Part B: Journal of Engineering Manufacture*, *216*(1), 87–101. https://doi.org/10.1243/0954405021519726

[29] Yang, Y., Wan, M., Ma, Y.-C., & Zhang, W.-H. (2016). An improved method for Tool Point Dynamics Analysis using a bi-distributed joint interface model. *International Journal of Mechanical Sciences*, *105*, 239–252. https://doi.org/10.1016/j.ijmecsci.2015.11.014

[30] Liao, J., Yu, D., Zhang, J., Feng, P., & Wu, Z. (2017). An efficient experimental approach to identify tool point FRF by improved receptance coupling technique. *The International Journal of Advanced Manufacturing Technology*, *94*(1-4), 1451–1460. https://doi.org/10.1007/s00170-017-0957-y

[31] Schmitz, T.L., & Burns, T.J. (2003). Receptance Coupling for High-Speed Machining Dynamics Prediction. *Conference & Exposition on Structural Dynamics.*

[32] Burns, T. J., & Schmitz, T. L. (2005). A study of linear joint and tool models in spindle-holder-tool receptance coupling. *Volume 6: 5th International Conference on Multibody Systems, Nonlinear Dynamics, and Control, Parts A, B, and C*. https://doi.org/10.1115/detc2005-85275

[33] Cheng, C.-H., Schmitz, T. L., Arakere, N., & Duncan, G. S. (2005). An Approach for Micro End Mill Frequency Response Predictions. *Manufacturing Engineering and Materials Handling, Parts A and B*. https://doi.org/10.1115/imece2005-81215

[34] Schmitz, T. L., Davies, M. A., & Kennedy, M. D. (2001). Tool point frequency response prediction for high-speed machining by RCSA. *Journal of Manufacturing Science and Engineering*, *123*(4), 700–707. https://doi.org/10.1115/1.1392994

[35] Schmitz, T., Betters, E., Budak, E., Yüksel, E., Park, S., & Altintas, Y. (2023). Review and status of tool tip frequency response function prediction using receptance coupling. *Precision Engineering*, *79*, 60–77. https://doi.org/10.1016/j.precisioneng.2022.09.008

[36] Schmitz, T. L., & Duncan, G. S. (2005). Three-component receptance coupling substructure analysis for Tool Point Dynamics Prediction. *Journal of Manufacturing Science and Engineering*, *127*(4), 781–790. https://doi.org/10.1115/1.2039102

[37] Tunc, L. T. (2017). Prediction of tool tip dynamics for generalized milling cutters using the 3D model of the Tool Body. *The International Journal of Advanced Manufacturing Technology*, *95*(5-8), 1891–1909. https://doi.org/10.1007/s00170-017-1286-x

[38] Chen, S.-Y. (2012). An equivalent direct modeling of a rotary shaft with hot-fit components using contact element modal analysis results. *Computers & Mathematics with Applications*, *64*(5), 1093–1099. https://doi.org/10.1016/j.camwa.2012.03.027

[39] Tol, S.; Özgüven, N.: Dynamic characterization of bolted joints using FRF decoupling and optimization, Mechanical Systems and Signal Processing 54-55, (2015), pp.124-138

[40] Wu, Y. (2012). Parametric inverse of severely ill-conditioned Hermitian matrices in signal processing. *Journal of the Franklin Institute*, *349*(3), 1048–1060. https://doi.org/10.1016/j.jfranklin.2011.12.006

[41] *Standard shrink fit Chuck HSK-A63 - Haimer UK*. Haimer GmbH. (2020, December 14). Retrieved April 5, 2023, from https://www.haimer.biz/products/tool-holders/din-69893-hsk-a-hsk-e-hsk-f/hsk-a63/shrink-fit-chuck/standard.html

[42] *Mini shrink shrink fit extension- Haimer*. Haimer GmbH. (2018, May 18). Retrieved April 5, 2023, from https://www.haimer.biz/products/tool-holders/accessories/shrinking-extensions/mini-shrink-shrink-fit-extensions/standard.html

[43] *Solid carbide end Mill Haimer Mill - F2004NN chamfer*. Haimer GmbH. (2020, December 21). Retrieved April 5, 2023, from https://www.haimer.biz/products/tools/solid-carbide-end-mills/haimer-mill/haimer-mill-f2004nn-chamfer.html

[44] Shanshin, I. K., Shagniev, O. B., & Burdakov, S. F. (2019). Adaptive self-excited vibrations suppression during milling. *Journal of Physics: Conference Series*, *1236*(1), 012051. https://doi.org/10.1088/1742-6596/1236/1/012051

[45] Duarte, M. L., & Ewins, D. J. (2000). Rotational degrees of freedom for structural coupling analysis via finite-difference technique with residual compensation. *Mechanical Systems and Signal Processing*, *14*(2), 205–227. https://doi.org/10.1006/mssp.1999.1241